Studies on defect and contact properties of $ZnSnP_2$ for application to thin film photovoltaics

2022

Taro Kuwano

Contents

1. General introduction

1.1. Solar cell —an essential power generation for sustainable society—

After the innovation of steam engines through the Industrial Revolution in the 18th century, human beings have consumed a tremendous amount of coal, petroleum, and natural gas for power generation and emitted a corresponding amount of carbon dioxides (CO_2). Although it has been a long time since it was pointed out that the content of CO_2 in the atmosphere is one of the main factors on global warming, many countries still rely on thermal power generation, as shown in Figure 1-1, because of lower cost than other techniques [1–3]. As declared in the 17 Sustainable Development Goals (SDGs) of the United Nations [4], it is urgent to develop and spread cheaper and cleaner power generation techniques.

Alternative sources to fossil fuels are nuclear power, wasted energy like biomass and heat, and renewable energy like wind, tidal, hydro, geothermal, and solar powers [5]. Considering the total energy of solar irradiation on the earth is 7000–8000 times larger than the world energy consumption [5,6], solar power can be the stem of sustainable society. In addition, solar cells can be

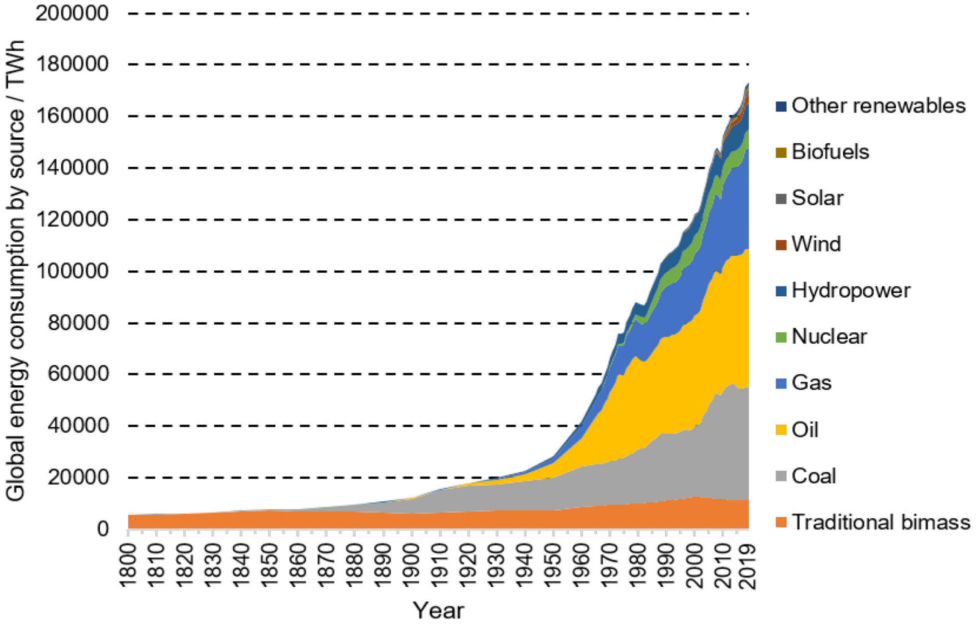

Figure 1-1. Global primary energy consumption by source [3].

used for various purposes and situations; for portable devices and vehicles such as cars, aircrafts, and satellites; at remote places such as islands, highlands, deserts, and space; and in emergencies where electrical supply shuts down. Such substantial usefulness of solar cells is indispensable to follow the increasing demands for electricity in the movement toward the IoT society and to struggle with the increase in natural disasters resulting from climate changes.

1.2. Principles of photovoltaic conversion in solar cells

Solar cells are devices that directly convert optical energy to electricity. As schematically shown in Figure 1-2, compound-based solar cells typically consist of multi-layers with various properties, indicating the importance of combinations of materials. It is necessary to understand photovoltaic (PV) conversion principles in solar cells and the properties expected for each layer.

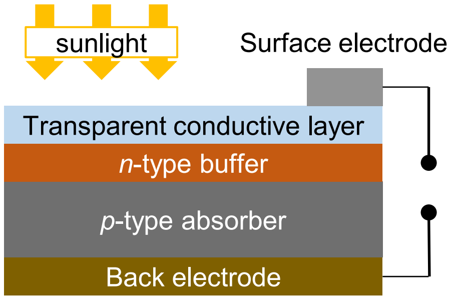

Figure 1-2. Schematic illustration of typical solar cells based on compounds.

1.2.1. Light absorption and carrier generation

The PV conversion process in solar cells can be divided roughly into two steps; carrier generation and transport. At first, incident light absorbed by solar cells generates free carriers with a specific rate determined mainly by the relationship of the flux and wavelength of the incident light and the absorption coefficient and the bandgap of the absorption layer. A high absorption coefficient leads to a high carrier generation and high PV conversion efficiency for the same absorber thickness.

On the other hand, the maximum current and voltage are trade-offs at a specific bandgap: a small bandgap leads to a large current but small voltage, while a large bandgap leads to a large voltage but small current. It leads to the well-known Shockley-Qeuisser theory, which quantitatively describes the relationship between bandgap of absorption layers and PV conversion efficiencies of solar cells [7]. For example, theoretical efficiencies are over 30% in the range of the bandgap between 1.0 –1.6 eV as shown in Figure 1-3 under the sunlight of air-mass 1.5 global tilt (AM 1.5G) [7,8]. Choosing an absorber material with a high absorption coefficient and suitable bandgap to the subjected incident light spectrum is crucial.

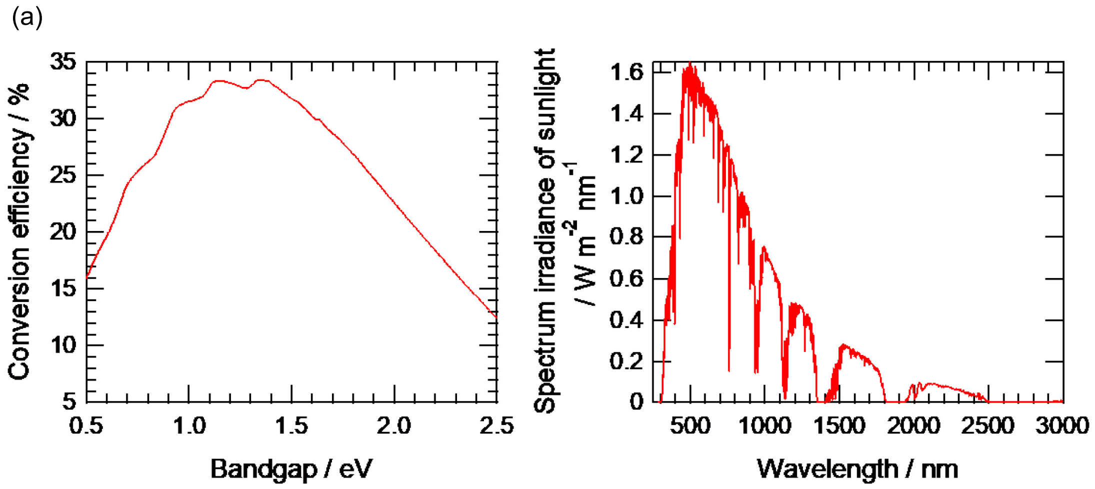

Figure 1-3. (a) Relationship between conversion efficiency of solar cells and bandgap of absorber layers calculated based on Shockley-Queisser theory and (b) spectrum irradiation of sunlight under AM 1.5G.

1.2.2. Carrier transport

Photo-generated carriers need to be transported to external circuits without any loss as possible. Usually, one incident photon generates one pair of negative and positive carriers, called an electron-hole pair. The photo-generated carriers with high kinetic and potential energy enough to overcome Coulomb attraction can diffuse in certain distances. The distance and period until recombination, called carrier diffusion length and lifetime, respectively, are favorable to be long for carrier transport.

It is vital to reduce defects that may scatter or trap carriers, hinder carrier diffusion, and decrease the extraction of electricity. Such defects may exist not only in intra-layers but also at interfaces.

1.2.3. Equivalent circuit and diode equation of solar cells

If there is only an isotropic electric field around an absorption media, photo-generated carriers diffuse in random directions, and the net electrical current becomes zero. Generally, *pn* diodes are used to generate a unidirectional electric field and assist the separationof carriers with negative and positive charge diffusing in opposite directions. An equivalent circuit of solar cells are described as shown in Figure 1-4 (a). The relationship between current density and voltage in solar cells are usually expressed by a modified diode equation [9];

$$J = -J_0\left[\exp\left(\frac{q(V-R_sJ)}{nkT}\right)-1\right]+\frac{V-R_sJ}{R_{sh}}+J_{ph}\,, \tag{1-1}$$

where J_0, J_{ph}, n, R_s, R_{sh} are reverse saturation current density, photo-generated current density, ideality factor, series resistance, and shunt resistance, respectively. k, q, T are the Boltzmann constant, elementary charge, and absolute temperature, respectively. Figure 1-4 (b) shows typical current density-voltage (*J*-*V*) characteristics under dark and illuminated conditions. The following equation

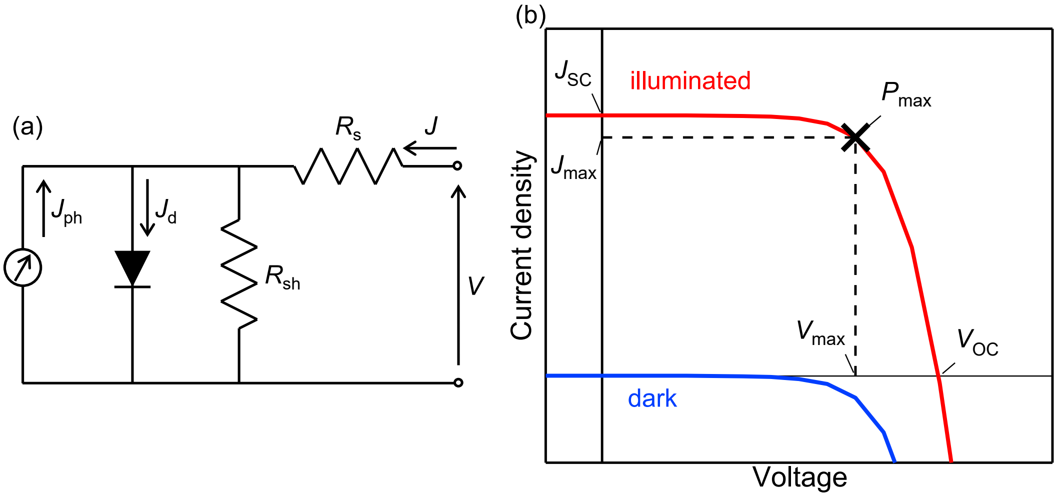

Figure 1-4. (a) Equivalent circuit of solar cells with diode parameters described and (b) *J-V* characteristics under dark and illuminated conditions and device parameters of solar cells.

determines PV conversion efficiency (PCE);

$$\mathrm{PCE} = \frac{J_{\max} \cdot V_{\max}}{W_{\mathrm{photo}}} = \frac{J_{\mathrm{SC}} \cdot V_{\mathrm{OC}} \cdot FF}{W_{\mathrm{photo}}}, \tag{1-2}$$

where the product of $J_{\max}$ and $V_{\max}$ is the maximum operating point, $P_{\max}$ in Figure 1-4 (b). $P_{\max}$ is also expressed by another product of J_{SC}, V_{OC}, and FF: the short-circuit current density, open-circuit voltage, and fill factor. W_{photo} is the power of incident light per unit area. J_{sc}, V_{oc}, and FF are the most frequently used parameters to evaluate the performance of solar cells.

1.3. Solar cells based on inorganic absorber materials

Figure 1-5 shows a classification tree of the adamantine family of compound semiconductors [10], where Roman numerals represent the number of valence electrons. Various adamantine compounds are derived from group IV elements by replacing one with two elements with

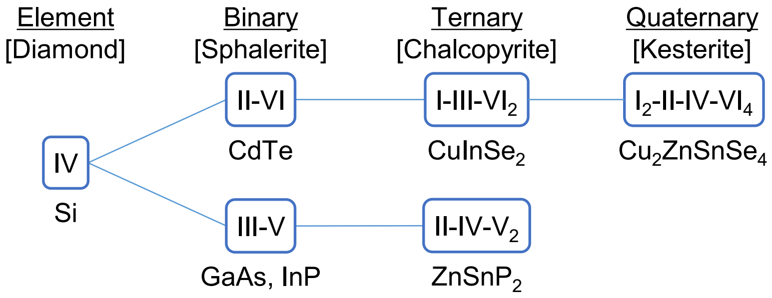

Figure 1-5. Classification tree of adamantine family of compounds [10].

Table 1-1. PCE and areas of various solar cells and modules [11].

	Cell		Module	
	PCE / %	Area / cm^2	PCE / %	Area / cm^2
Si mono-crystalline	26.7	79	24.4	13177
Si multi-crystalline	24.4	268	20.4	14818
GaAs	29.1	0.998	-	-
CIGS	23.4	1	19.2	841
CdTe	21	1	19	23573
Perovskite	22.6	1	17.9	804

keeping the number of nominal valence electrons per atom at four. As named adamantine, many compounds have diamond-like crystal structures such as sphalerite-, chalcopyrite-, and kesterite-types. Absorber materials used in the PV industry like Si, GaAs, InP, $CuInSe_2$, and CdTe are all included in this family.

1.3.1. Commercial materials

Table 1-1 shows PCE of several types of solar cells and modules [11]. Since the first PV conversion with *pn*-junction was reported on Si-based solar cells by Chapin, Fuller, and Pearson in the 1950s [12], various types of solar cells using monocrystalline, polycrystalline, and amorphous Si have been developed. Continuous researches over 60 years push up the PCE of Si solar cells more than 26% [13,14]. Accordingly, the PCE of modules sold by the ten biggest PV companies worldwide is higher than 20%, and Si-based solar cells occupy 95% of the world PV production [15].

III-V compounds like GaAs, InP, and their alloys have been studied for several decades. The efficiencies of III-V based single-junction solar cells are higher than 29% [16]. Although the high process cost limits their use in high-efficiency tandem or concentrated solar cells for the space industry [17], the highest efficiency of 47.1% was reported for 6-junction tandem solar cells under the direct spectrum at 143 Suns concentration [18].

Solar cells based on thin-film $CuInSe_2$ (CIS) and CdTe have been intensively researched because their high absorption coefficients and lightweights make it possible to cover the installation limit of Si-based solar cells, as the highest PCE of CIS- and CdTe-based solar cells are 23.35% [19] and 22.1% [20], respectively. Recently, the share of CdTe solar cells in the annual world products of thin-film solar cells has been growing and has become 78% until 2020 [15]. Further demands for thin-film PVs can be expected in the near future because vast lands for mega-solar systems are limited, and solar cells will need to be installed on other places such as roofs, walls, vehicles, etc.

Table 1-2. Device parameters of emergent inorganic solar cells with PCE > 10%.

Material	PCE / %	V_{OC} / V	J_{SC} / mA cm^{-2}	FF / %	Device structure
Cu_2ZnSnS_4 (CZTS)	11	0.731	21.74	69.3	Glass/Mo/CZTS/CdS/i-ZnO/ITO/Al/MgF_2
$Cu_2ZnSn(S_{0.25}Se_{0.75})_4$ (CZTSSe)	12.6	0.513	35.2	69.8	Glass/Mo/CZTSSe/CdS/ZnO/ITO/Ni/Al/MgF_2
$Cu_2ZnSn(S_ySe_{1-y})_4$ (CZTSSe)	12.62	0.541	35.35	65.9	Glass/Mo/CZTSSe/CdS/ZnO/ITO/Ni/Al/MgF_2
$Cu_2ZnSnSe_4$ (CZTSe)	12.5	0.491	37.37	68.2	Glass/Mo/CZTSe/CdS/ZnO/AZO/Ni/Al/MgF_2
Q-1D $Sb_2(S,Se)_3$	10	65.5	24.07	63.5	Glass/FTO/CdS/Sb_2Se_3/Spiro-OMeTAD/Au
$Cu_2ZnCdSnS_4$	12.6	0.64	27.8	71	Glass/Mo/CZCTS/CdS/ITO/Ag
$(Ag_{0.05-0.3}Cu_{0.95-0.7})_2ZnSn(S,Se)_4$	11.2	0.464	36.2	66.5	Glass/Mo/ACZTSSe/CdS/ZnO/ITO/Ag
$(Ag_{0.05}Cu_{0.95})_2(Zn_{0.75}Cd_{0.25})S_4$	10.1	0.65	23.4	66.2	Glass/Mo/ACCdZTS/CdS/ITO/Ag
$Cu_2Zn(Sn_{0.78}Ge_{0.22})Se_4$	12.3	0.527	32.2	72.7	Glass/Mo/CZTGTSe/CdS/ZnO/AZO/Ag/ARC
$(Li_{0.06}Cu_{0.94})_2ZnSn(S,Se)_4$	11.6	0.531	33.7	64.8	Glass/SiOx/Mo/LiCZTSSe/CdS/ZnO/AZO/Ni/Al/MgF_2
$Cu_2ZnSn_xGa_{1-x}(S,Se)_4$	10.8	0.455	36.48	65.05	Glass/Mo/CZTGSSe/CdS/iZnO/ITO/Ag/MgF_2
Q-1D $Sb_2(S_xSe_{1-x})_3$	10.5	0.664	23.8	66.3	Glass/FTO/$Sb_2(S_xSe_{1-x})_3$/Au

1.3.2. Emerging inorganic absorbers

Scientists are now eagerly exploring emerging absorber materials without expensive and toxic elements like Ga, In, Se, Cd, and Te in $Cu(In,Ga)Se_2$ and CdTe for further spreading of solar cells. This section briefly introduces studies on emerging inorganic absorbers of chalcogenides and pnictides. Table 1-2 summarized emergent inorganic solar cells with PCE > 10% referred to [21]. Analog materials to lead-halide perovskites are mentioned elsewhere [22].

Chalcogenides

In ref [21], half of the listed emerging materials are chalcogenides. Especially, I_2-II-IV-VI_4 group materials, which are close to well-established I-III-VI_2 materials like $CuInSe_2$, have been intensively studied by substituting or alloying. Solar cells based on $Cu_2ZnSn(S,Se)_4$ (CZTSSe), a solid solution of Cu_2ZnSnS_4 and $Cu_2ZnSnSe_4$, showed the highest efficiency of 12.6% in chalcogenides [23,24]. Quasi one-dimensional (Q-1D) antimony-based chalcogenides like Sb_2S_3, Sb_2Se_3, and $Sb_2(S,Se)_3$ alloy have recently attracted much attention as one of low-dimensional absorbers and the PCE is of 7–10% [25–29].

Pnictides

In contrast to chalcogenides, applications of novel pnictides to solar cells are very few. Even for Zn_3P_2, a relatively famous pnictide in the above review, there are only 12 reports on solar cell applications [30]. In other words, pnictides are frontier worth exploration to expand materials diversity. Similar to the relation between II-VI and I-III-VI_2 groups, there are II-IV-V_2 group materials that are derivatives from III-V compounds by replacing III to II and IV elements. II-IV-V_2 group materials were reviewed at first by Shay and Wernick about 60 years ago [31]. Recently, the research group of Tamboli pointed out their tunability of lattice constants and bandgaps alloying and utility for photovoltaic devices [32,33].

1.4. Overview of the previous studies on $ZnSnP_2$

$ZnSnP_2$, the subject material of this study, is one of the II-IV-V_2 materials without toxic and expensive elements. Since Goodman reported the synthesis of $ZnSnP_2$ in 1957 [34], $ZnSnP_2$ has been studied mainly by the groups in Ioffe Institute, Texas University, and Kyoto University. In this chapter, the previous studies on $ZnSnP_2$ are overviewed with focusing on physical properties, structural analysis, growth methods, and applications.

1.4.1. Physical properties

In 1968, Vaipolin et al. reported that $ZnSnP_2$ has two modifications, chalcopyrite ($I\bar{4}2d$

5.651 Å, $c/a = 2$) and sphalerite ($F\bar{4}3m$, $a = 5.651$ Å, $c/a = 1$) types as shown in Figure 1-6 (a) and (b) [35]. The Wyckoff positions of Zn, Sn, and P atoms are 4a, 4b, and 8d, respectively. A parameter X, which is used for the description of the position of P atoms, equals 0.238 for chalcopyrite and 0.25 for sphalerite.

It is commonly reported that $ZnSnP_2$ is an intrinsically p-type semiconductor. For small crystals grown by simply cooling the solution in Sn flux, carrier density and mobility are usually about 10^{16}–10^{18} cm^{-3} and 5–50 $cm^2\ V^{-1}\ s^{-1}$, respectively [35–39]. According to Nakatsuka et al., those s of large bulk crystals of nearly 10×10×1 mm^3 in dimensions are 6×10^{16}–2×10^{17} cm^{-3} and 1–3 $cm^2\ V^{-1}\ s^{-1}$ [40], which is suitable values for the absorber of solar cells.

Goryunova et al. reported, based on the analysis of band-structure, that the fundamental absorption is associated with the direct transition between the valence band (VB) and the conduction band (CB) at the Γ point in the **k**-space [37]. According to the first principles calculation by Yokoyama et al., the absorption coefficient of $ZnSnP_2$ is more than 10^4 cm^{-1} in the range of photon energy above 1.8 eV, which is comparable to other compound absorber materials like GaAs, CdTe, and $Cu(In,Ga)Se_2$ [41].

Berkovskii et al. measured cathode-luminescence (CL) spectra for $ZnSnP_2$ grown with a low cooling rate and observed the radiative recombination (RR) with the energy of 1.46 eV [42]. They attributed this CL to the band-to-band (BB) transition. Kradinova et al. observed the RR from donor-

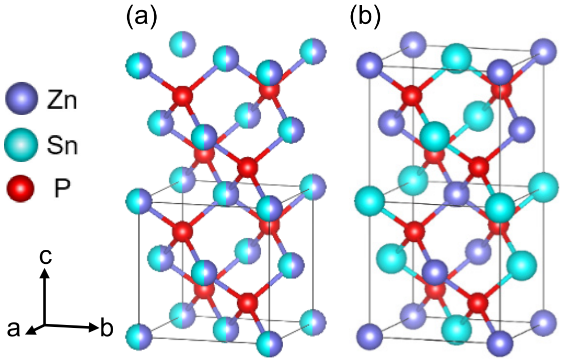

Figure 1-6. (a) Sphalerite- and (b) chalcopyrite-type $ZnSnP_2$.

to-acceptor (DAP) transition only for $ZnSnP_2$ grown with a high cooling rate during crystallization from Sn -solution [43]. They also confirmed the decrease of the RR from DAP transition and the blue-shift of the RR from BB transition by heat treatment at 870−1050 K. They concluded the heat treatment led to the decrease of the donor and acceptor densities, supposing the DAP come from cation antisites. Nakatsuka et al. observed photoluminescence (PL) at 1.69 eV for $ZnSnP_2$ grown by unidirectionally cooling Sn-solution with a cooling rate of 0.7 ºC h^{-1} [44], which is much slower than that employed by Berkovskii et al. [42].

Nakatsuka et al. also reported a fast decay of time-resolved PL (TRPL) spectra, indicating more than 99% of photo-generated minority carriers drop from the CB to other energy levels in sub-nano seconds [44]. Short carrier lifetime was confirmed by Berkovskii et al., too, by CL measurement at 80 K [42]. They took the Burstein effect into account and estimated the carrier lifetime as $(4–6)\times10^{-10}$ sec from the photo-generated electron density of $\sim1.5\times10^{18}$ cm^{-3} and the injected current density of $(1–3)\times10^{27}$ cm^{-3} sec^{-1}. Such a fast decay is not favorable to solar cells, while it becomes an advantage for the application to photodetectors, which require rapid response to the on/off of light.

1.4.2. Native defects

Kumagai et al. studied in detail the point defects in $ZnSnP_2$ by ab-initio calculation [45]. They considered 11 types of native point defects; Zn, Sn, and P vacancies (V_X, X = Zn, Sn, and P), Zn, Sn, and P interstitials at the ic and ia sites (X_{ia} and X_{ic}, X = Zn, Sn, and P) and Zn-on-Sn and Sn-on-Zn cation antisites (Zn_{Sn} and Sn_{Zn}) with different charge states; and calculated their formation energies and thermodynamical transition levels (TTLs) which corresponds to defect levels detected by transient capacitance measurements. Figure 1-7 shows the TTLs of the 11 defects. TTLs of V_{Sn}, V_P, Zn_{ic}, Zn_{ia}, P_{ic}, P_{ia}, and Sn_{Zn} are located between the valence band maximum (VBM) and the conduction band minimum (CBM), indicating these defects can work as traps or recombination centers. It was also

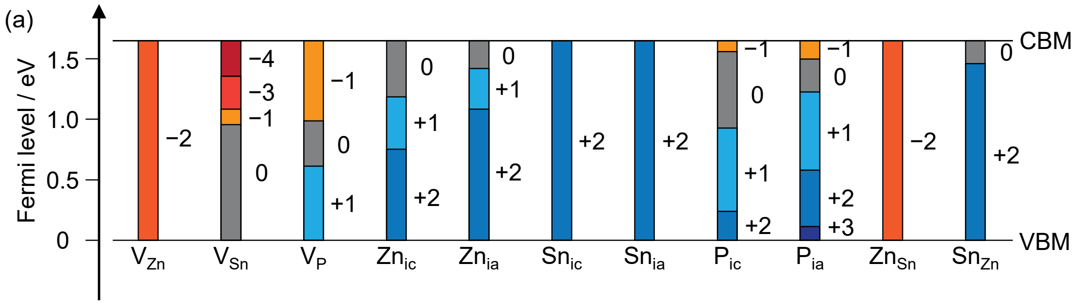

Figure 1-7. (a) Thermodynamical transition levels (TTLs) and formation energies of native point defects in $ZnSnP_2$ under (b) Zn-rich and (c) Zn-poor conditions calculated by Kumagai et al. [59]

reported that antisites Zn_{Sn} and Sn_{Zn} have especially low formation energies. This associates with the fact that $ZnSnP_2$ exhibits order-disorder transition. Note that Kumagai mentioned the TTL of Zn_{Sn} is just above the VBM, and Zn_{Sn} works as an acceptor. This indicates these cation antisites would influence electrical properties. On the other hand, V_P, Zn_{ic}, and Zn_{ia} have low formation energies and in-gap TTLs, which can cause degradation of carrier transport properties of $ZnSnP_2$.

On the other hand, Nakatani et al. considered antisites of Sn on Zn sites (Sn_{Zn}) and the vacancy of Zn (V_{Zn}) as candidates of donor and acceptor for the DAP transition, respectively, supposing that the formation energy of V_{Zn} is low as for $ZnGeP_2$ [46]. Miyauchi et al. found that annealing $ZnSnP_2$ in Zn atmosphere resulted in the decrease in the PL intensity associated with the DAP. They concluded from this finding that the decrease of V_{Zn} led to the decrease of RR from DAP transition. However, the formation energy of V_{Zn} is not low, according to the ab-initio study by Kumagai et al. [45]. As mentioned above, Kumagai et al. suggested that antisites of Zn on Sn sites (Zn_{Sn}) have low formation energy and rather contribute to the shallow acceptor level. Nakatsuka and Nose reported annealing $ZnSnP_2$ above 500 °C in evacuated ampule resulted in the increase of the degree of order and the bandgap of $ZnSnP_2$ [47]. The decrease of RR from DAP transition confirmed by Miyauchi may be due to the decrease of Zn_{Sn} just by annealing, and V_{Zn} and Zn atmosphere were rather irrelevant.

1.4.3. Crystal growth

Crystals of $ZnSnP_2$ are usually obtained by cooling a solution of Zn and P in Sn flux. Figure 1-8 and Figure 1-9 show the ternary phase diagram of the Zn-Sn-P system at 600 ºC and the pseudo-binary phase diagram of Sn-ZnP_2 reported by Nose and Uda [48]. We can see the two-phase region of $ZnSnP_2$ and liquid, which is one of the reasons why we can obtain $ZnSnP_2$ from a liquid solution. However, due to the presence of a two-phase region of liquid and ZnP_2, the initial concentration of Sn in the solution must exceed 90 mol% in order to obtain pure $ZnSnP_2$ directly from the solution. This leads to an inevitably small volume fraction of obtained $ZnSnP_2$. In addition, in such a dilute solution, crystal growth is strongly limited by the diffusion velocity of solute species. These restrictions, for example, resulted in the small dimensions of $3 \times 4 \times 0.4$ mm^3 for platelet $ZnSnP_2$ prepared by simply cooling the solution with a rate of 5 ºC h^{-1} or more [49]. Therefore, the growth of bulk crystals of pure $ZnSnP_2$ requires unidirectionally cooling the solution of 90mol%-Sn at a much slow cooling rate. In this point of view, Nakatsuka et al. used a so-called Bridgman method. They fabricated a moving furnace having a steep temperature gradient and made it possible to obtain centimeter-scale bulk crystals of pure $ZnSnP_2$ by unidirectionally cooling from the bottom of the solution of 92 mol%-Sn in ampule with a diameter of 11 mm at a rate of 0.7 ºC h^{-1} from 700 ºC in nearly 30days [40]. Such a centimeter-scale crystal is useful for various characterizations and applications, for example, absorber in solar cells. Another merit of this method is the disuse of acid, which is needed to remove the matrix of Sn when the pieces of small platelet $ZnSnP_2$ disperse throughout the matrix. Nakatsuka et al. sequentially studied the influence of cooling rate on the crystal structure and physical properties of $ZnSnP_2$ by using the same method as mentioned in the following sub-section.

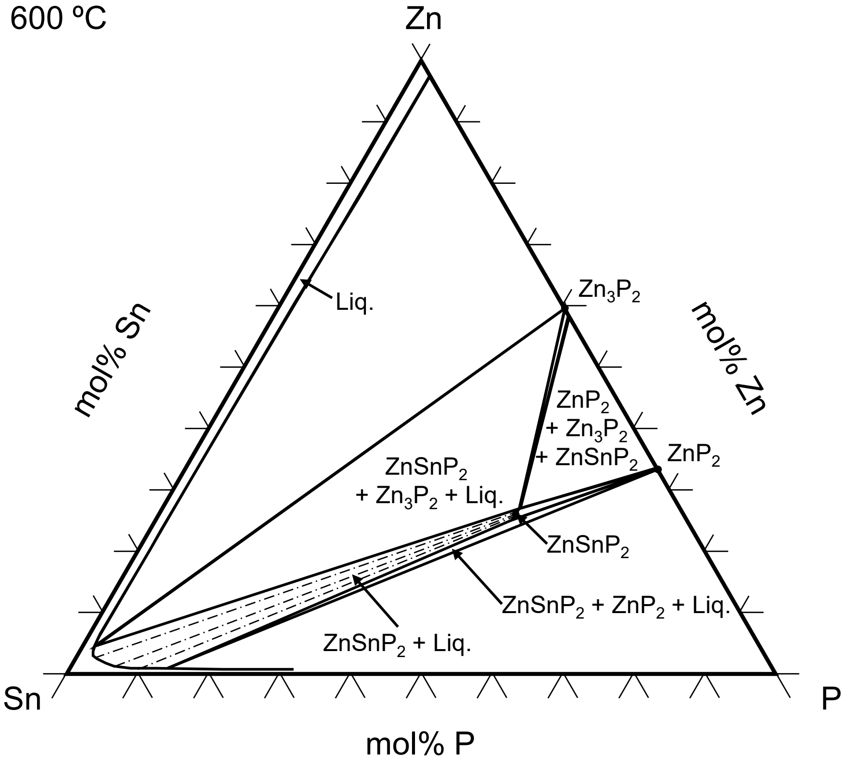

Figure 1-8. Ternary phase diagram of Zn-Sn-P system at 600 °C [48].

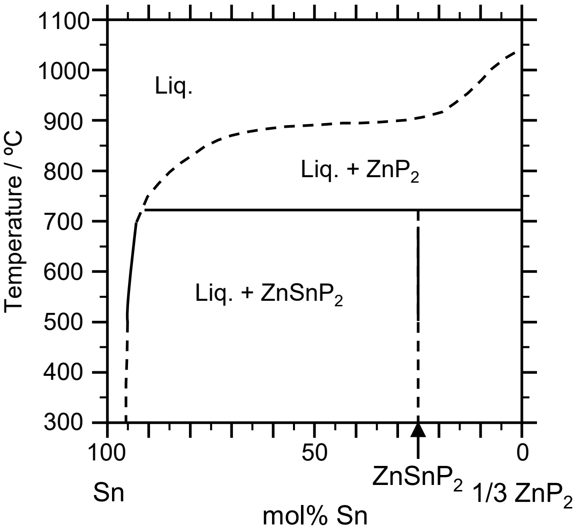

Figure 1-9. Pseudo-binary phase diagram of Sn-ZnP₂ [48].

1.4.4. Order-disorder phenomena

The phase transition between sphalerite and chalcopyrite $ZnSnP_2$ corresponds to the change in the randomness of atomic arrangement on the cation sublattice, as is the case for other II-IV-V_2 compounds [31,32]. For the chalcopyrite phase of $ZnSnP_2$, a degree of order can be defined for the randomness. As mentioned above, the degree of order affects the physical properties of $ZnSnP_2$. Vaipolin et al. pointed out that the change of the cooling rate during crystallization makes it possible to obtain $ZnSnP_2$ with various degrees of order and to change its physical properties [35]. Scanlon and Walsh calculated the electronic structure of $ZnSnP_2$ and predicted that the bandgap of $ZnSnP_2$ changes from 0.75 to 1.70 eV between the perfectly disordered to perfectly ordered states [50]. Nakatsuka an Nose reported a comprehensive study on the bandgap change in $ZnSnP_2$ by experimentally evaluating the degree of order [47]. They evaluated the abdgap and the long-range order (LRO) parameter η for $ZnSnP_2$ grown with different cooling rates using the Warren's method. According to Warren, LRO parameter η is expressed by the following equation:

$$\eta = r_{\alpha}^{Zn} + r_{\beta}^{Sn} - 1 \tag{1-5}$$

where r_{α}^{Zn} and r_{β}^{Sn} are ratios of α and β sites occupied by Zn and Sn atoms, respectively. α and β

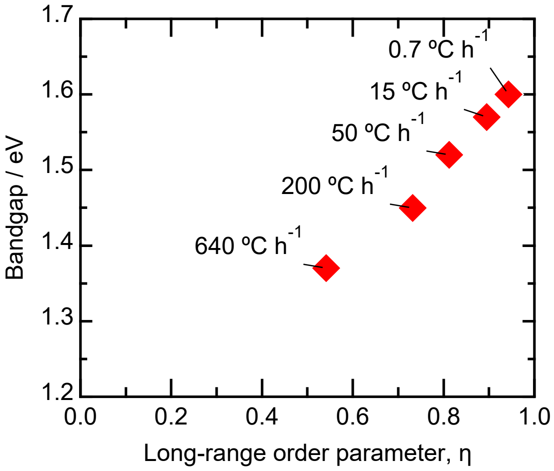

Figure 1-10. The relationship between the bandgap and the LRO parameter of $ZnSnP_2$ grown with different cooling rates [47].

sites are respectively occupied by only Zn and Sn atoms in the perfectly-ordered state. $\eta = 1$ corresponds to the perfectly ordered state and $\eta = 0$ to the perfectly disordered one. The LRO is directly related to the structure factor of the superlattice reflection in x-ray diffraction (XRD) experiments. The intensity of superlattice reflection is smaller for the lower LRO parameter. Nakatsuka and Nose evaluated the LRO parameter by two methods: one is calculating the occupancy from the Rietveld refinement, and the other is comparing the measured and calculated peak area ratio of superlattice to fundamental reflections. In their report, both methods gave almost the same LRO parameters. Figure 1-10 shows the reported relationship between the LRO parameter and the bandgap for the $ZnSnP_2$ grown from the Sn solution with different cooling rates. It is obvious that the bandgap is changed from 1.35 to 1.6 eV as the increase of the degree of order.

The coordination environment around P atoms is also changed with the degree of order. In the perfectly ordered stoichiometric $ZnSnP_2$, phosphorus atoms are surrounded by two Zn and two Sn atoms as shown in Figure 1-11 because this coordination is the electrically most stable. Following the cation-disordering, however, the number of the first nearest neighbor (1st NN) cations around P atoms can be changed partially from the most stable combination. For example, as shown in Figure 1-11, some P atoms are surrounded by 1 Zn and 3 Sn atoms under low LRO. According to Ryan et al. [36], this change of the number of 1st NN cations around P atoms resulted in small satellite peaks of ^{31}P NMR. In contrast, the coordination around Zn and Sn is rarely changed: each cation is always surrounded by 4 P atoms.

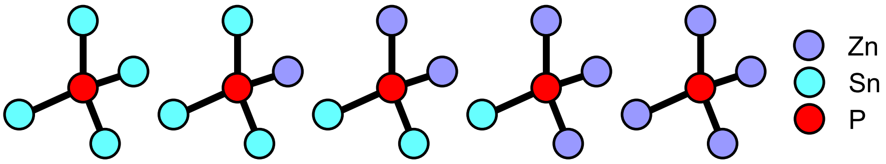

Figure 1-11. The schematic illustrations five types of the coordination around P atoms. The center one is the electrically most stable coordination: 2 Zn and 2 Sn surround each P atom.

Raman spectroscopy was also used for the evaluation of the degree of order in thin-film $ZnSnP_2$. According to Kaminow et al. [51], the representation of the zone-center optical phonons is given by

$$\Gamma_{\mathrm{optic}} = 1\Gamma_1 + 2\Gamma_2 + 3\Gamma_3 + 3\Gamma_4 + 6\Gamma_5 \quad (1\text{-}1)$$

and that of the acoustic modes by

$$\Gamma_{\mathrm{acoustic}} = 1\Gamma_4 + 1\Gamma_5. \quad (1\text{-}2)$$

The five vibration modes from Γ_1 to Γ_5 of II-IV-V_2 materials with chalcopyrite structure have 17 normal-mode displacement coordinates, denoted ν_i. Each ν_i is associated with the atomic displacements of Zn, Sn, and P in the directions along the crystal axes, x, y, and z. Among the five modes, Γ_1, Γ_3, Γ_4, and Γ_5 are Raman-active while Γ_2 is Raman-inactive. Γ_2 is also a disorder-activated mode. Optical modes having Γ_1 and Γ_2 symmetry involve only the displacements of P atoms while those with Γ_3, Γ_4, and Γ_5 symmetry include the displacements of Zn and Sn as well. Because Γ_1 is associated only with the displacements of P atoms, of which coordination is more easily changed than those of cations, Actually, Mintairov et al. observed that the peak intensity of the Γ_1 mode is decreased with the decrease of the degree of order in thin-film $ZnSnP_2$ epitaxially grown on GaAs substrates by molecular beam epitaxy (MBE) [52]. Table 1-3 summarizes the vibration frequencies measured by infra-red (IR) absorption and Raman spectroscopy and calculated in the previous studies [52–58].

Table 1-3. Vibration frequencies measured by IR absorption and Raman spectroscopy and calculated in the previous studies. *Mulliken's irreducible representation; **representation used by Kaminow et al [39].

*	**	IR [42]	IR [38]	Raman [38]	Cal. [38]	Cal. [41]	Cal. [54]	Cal. [55]	Cal. [56]	Cal. [51]
E	$\Gamma_{5L/T}$	—	—	—	115/115	125/125	85	77/77	77	81
B_1	Γ_3	—	—	—	124	138	106	106	—	96
B_2	$\Gamma_{4L/T}$	—	—	—	140/139	149/148	98	105/101	—	92
E	$\Gamma_{5L/T}$	—	—	—	154/153	165/164	108	119/116	—	109
E	$\Gamma_{5L/T}$	—	—	—	190/189	188/187	157	115/179	—	160
B_1	Γ_3	—	—	—	208	214	191	205	—	187
A_2	Γ_2	—	—	295	292	—	—	308	—	271
A_1	Γ_1	—	—	309	307	304	309	298	297	286
E	$\Gamma_{5L/T}$	—	318/313	—/317	317/315	312/311	318	325/321	232	272
A_2	Γ_2	—	—	333	331	—	—	332	—	323
E	$\Gamma_{5L/T}$	—/330	339/328	—/328	334/333	239/328	321	331/327	298	301
B_2	$\Gamma_{4L/T}$	—	—	347/—	329/324	345/335	331	353/323	316	305
B_1	Γ_3	—	—	353	352	346	333	358	297	326
E	$\Gamma_{5L/T}$	—	360/342	—/342	378/350	374/345	337	354/331	—	324
B_2	$\Gamma_{4L/T}$	368/—	—	365/—	372/348	375/354	350	360/359	353	347

Table 1-4. Growth methods of thin-film $ZnSnP_2$ and evaluation methods of its bandgap and crystal structure.

Growth method (Abbreviation; P-source)	Bandgap / eV (Evaluation method)	Crystal structure (Evaluation method)	Ref.
Chemical vapor deposition (CVD; Ca_3P_2)	1.5 eV (absorption)	Chalcopyrite? (XRD)	[47]
Liquid phase epitaxy (LPE; SnP_3)	-	Chalcopyrite (Laue back scattering)	[46]
Co-evaporation (MBE; red phosphorus)	1.62 eV (transmittance)	Chalcopyrite (θ-2θ XRD)	[48, 50, 51]
Molecular beam epitaxy (MBE; PH_3)	1.381 and 1.683 eV (electroreflectance)	Chalcopyrite (4-axes XRD)	[38, 49, 52–54]
Phosphidation (-; Sn_4P_3/Sn)	1.3 eV (room-temperature photoluminescence)	Sphalerite (θ-2θ XRD)	[58]
e-beam evaporation (-; $ZnSnP_2$)	1.5–1.6 eV (low-temperature photoluminescence)	Sphalerite (ω-2θ XRD)	[55–57]

1.4.5. Growth and physical properties of thin-film $ZnSnP_2$

Table 1-4 summarizes growth methods and optical properties of thin-film $ZnSnP_2$. Davis and Wolfe fabricated $ZnSnP_2$ thin films by liquid phase epitaxy (LPE), where $ZnSnP_2$ is precipitated on GaAs substrate from Sn flux by compositional supercooling as is the case of bulk crystal growth [59]. They evaluated the crystal structure of thin films grown by LPE by back-reflection Laue patterns and reported both chalcopyrite and sphalerite types could be obtained with different cooling rates, yet neither optical nor electrical properties were reported. Chemical vapor deposition (CVD) was employed by Sansregret, where $ZnSnP_2$ thin films were grown by annealing SnO_2 thin films in an ambient containing PH_3, H_2, and Zn-metal vapor [60]. The optical absorption data of the CVD film indicated the absorption edge of ~1.5 eV, while the presence of superlattice reflection was not clearly mentioned [60]. Ajmera, Shin, and Zamanian reported that the $ZnSnP_2$ films were obtained by co-evaporation of metal Zn, metal Sn, and red phosphorus. For the films obtained, the optical absorption edge of ~1.5 eV and *p*-type conductivity with resistivity, carrier concentration, and mobility are ~5 Ω cm, 3.37×10^{16} cm^{-3}, ~40 $cm^2V^{-1}s^{-1}$, respectively [61–63]. Studies on the crystal structure of thin-film $ZnSnP_2$ were sequentially reported by research groups at A.F. Ioffe institute and Texas University in 1999 and 2000. They used 4-axes XRD and Raman spectroscopy for $ZnSnP_2$ thin-film grown on GaAs substrate by MBE using PH_3 gas source [52,64–66]. They also controlled the degree of order of $ZnSnP_2$ films by changing Sn/Zn flux ratio. One of those groups later reported that the bandgap was also changed from about 1.3–1.7 eV by the flux ratio [67]. Mukherjee et al. reported thin-film growth by e-beam evaporation and fabrication of photo-detectors [68–70]. They pointed out the incredibly fast rise and decay time of response in $ZnSnP_2$ photo-detector were correlated with defect levels within energy gaps. Nakatsuka et al. fabricated thin-film $ZnSnP_2$ by phosphidation of Zn-Sn metal precursors using Sn_4P_3/Sn composites as a source of P_4 gas [71]. The phosphidation resulted in the formation of numerous protrusions that causes short-circuit in solar cells, leading to low efficiency of less than

0.1% as shown in Table 1- [44]. Based on a chemical potential diagram of the Zn-Sn-P ternary system, Nakatsuka et al. pointed out that the formation of Zn_3P_2 at first should be suppressed to avoid protrusions. To the best of our knowledge, there are no other reports on thin-film solar cells of $ZnSnP_2$.

1.4.6. Application to solar cells and related issues

In 2017, Nakatsuka et al. utilized $ZnSnP_2$ bulk crystals and reported the application of $ZnSnP_2$ to solar cells for the first time, although PCE was less than 1% [44]. Nakatsuka and his group have continuously improved the PCE of $ZnSnP_2$ solar cells up to 3.44% by modifying the fabrication procedure and device structure from the prototype, which was simply analogous to CIS-based solar cells. Table 1-5 summarizes efficiencies and the stacking structures of $ZnSnP_2$ solar cells. As is the case for other compounds, $ZnSnP_2$ solar cells also consist of surface electrode, transparent conductive layer, *n*-type buffer, *p*-type absorber, and back contact in this manner. Figure 1-12 shows a schematic illustration and *J*-*V* characteristics of the newest solar cell with a structure of Al/Al:ZnO/(Cd,Zn)S/$ZnSnP_2$/Cu where Cu was used as back contact [72]. However, there is still much room for improvement compared with CIS- or CdTe-based solar cells.

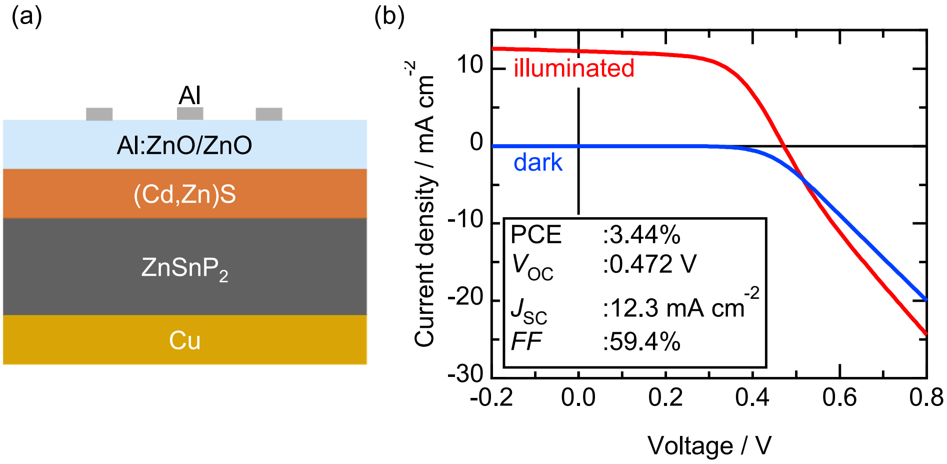

Figure 1-12. (a) Schematic illustration and (b) *J*-*V* characteristics under dark and illuminated conditions of the $ZnSnP_2$ solar cell with PCE of 3.44% [43].

Table 1-5. Device parameters of $ZnSnP_2$-based solar cells.

	Device structure	PCE / %	V_{OC} / V	J_{SC} / mA cm^{-2}	*FF* / %	Ref.
Bulk	Al/AZO/ZnO/CdS/ $ZnSnP_2$/Mo	0.087	0.172	1.99	25.5	[44]
	Al/AZO/ZnO/CdS/ $ZnSnP_2$/Cu	1.97	0.452	8.2	53.3	[73]
	Al/AZO/ZnO/(Cd,Zn)S/ $ZnSnP_2$/Cu	3.44	0.472	12.3	59.4	[72]
Thin film	Al/AZO/ZnO/CdS/ $ZnSnP_2$/Mo	0.0027	0.0037	2.63	27.2	[74]

As well as the physical properties of absorbers, the properties of interfaces are also important for the device performance solar cells. If there are band offsets and lattice mismatches at the interfaces between different functional layers in semiconductor devices, the carrier-recombination rate becomes high resulting in loss of current and voltage. A theoretical study by Minemoto et al. [46] pointed out that small offset at pn junctions leads to high PCE, V_{OC}, J_{SC}, and *FF*. From this point of view, the band-alignment between several sulfides and $ZnSnP_2$ was investigated. First-principles study by Hinuma et al. predicted that the valence band (VB) offset was ~1.0 eV for CdS/$ZnSnP_2$ and ~1.0 eV for ZnS/$ZnSnP_2$, which is not so different than those for CdS/ or ZnS/$CuInSe_2$ [75]. In contrast, x-ray photoelectron spectroscopy (XPS) study by Nakatsuka et al. revealed that the VB offset is nearly 2.0 eV for CdS/$ZnSnP_2$, which could result in a significant loss of voltage. By using (Cd,Zn)S, a solid solution of CdS and ZnS, Akari et al. improve the conversion efficiency up to 3.44% [72]. However, there should still be much loss in the open-circuit voltage. $CdSnP_2$ is one of the most promising n-type buffer materials for $ZnSnP_2$ in respect to band alignment and lattice matching. Nakatsuka demonstrated $CdSnP_2$/$ZnSnP_2$ junction exhibited favorable diode characteristics, although the series resistance was relatively high [76].

On the other hand, back contacts are selected in the viewpoint of the offset between the VBM of absorbers and the work function of subjected metals. For $ZnSnP_2$ with the VBM of 5.2 eV, Al (4.28 eV), Ag (4.26 eV), Mo (4.6 eV), and Cu (4.65 eV) were examined by Nakatsuka et al. [73,77], where the VBM corresponds to the ionization potential. Although every metal exhibited high contact resistance and rectification behavior like Schottky diode as-deposited, only Cu showed a reduction of the resistance by annealing. Figure 1-13 and Figure 1-14 show cross-sectional images by scanning transmission electron microscopy (STEM) and resistance-current (*R*-*I*) characteristics of the junction of Cu/ and Mo/$ZnSnP_2$, respectively, before and after annealing. In contrast to Mo/$ZnSnP_2$, where any change could not be confirmed in the microstructure and *R*-*V* characteristics, some reaction and reduction of resistance are confirmed at Cu/$ZnSnP_2$ interfaces. This implies not only work functions but also reactivity can be criteria for building up the low resistive junction. However, details of the reduction mechanism are unrevealed and the series resistance of the device with PCE of 3.44% was 15 Ω cm^2 [72], which is almost ten times larger than that calculated from the thickness (~200 μm) and the resistivity (10–70 Ω cm) of $ZnSnP_2$ bulk crystals [40].

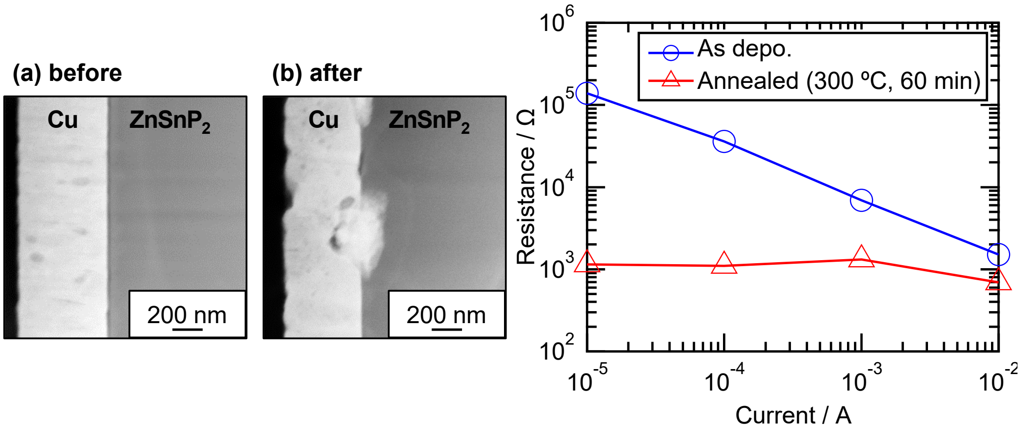

Figure 1-13. Cross-sectional STEM images of (a) before and (b) after annealing at 300 °C for 60 min and (c) R-I characteristics of Cu/ZnSnP$_2$ junction.

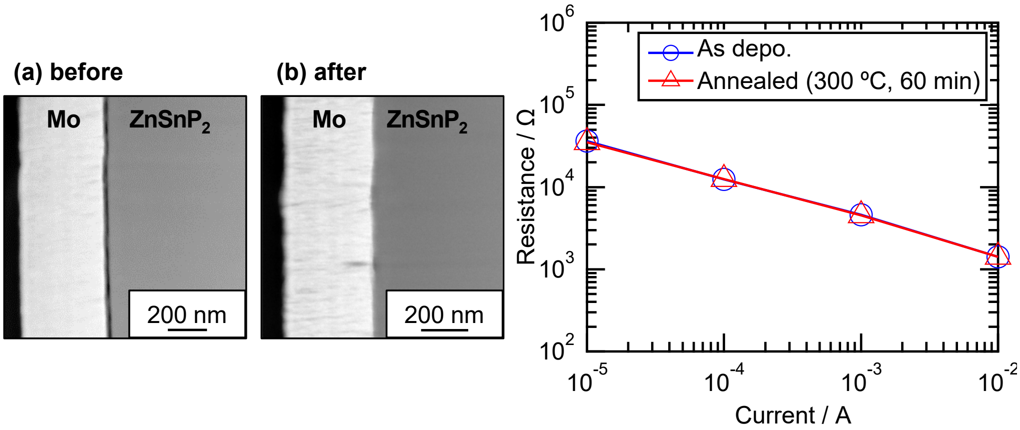

Figure 1-14. Cross-sectional STEM images of (a) before and (b) after annealing at 300 °C for 60 min and (c) R-I characteristics of Mo/ZnSnP$_2$ junction.

1.5. Objective and outline of this study

As described in the previous sections, high series-resistance in devices, small carrier lifetime, and establishment of thin-film preparation are challenging issues to overcome for further improving the performance of $ZnSnP_2$ solar cells. Thus, the objective of this study was set as follows.

1. Reduction of the series resistance: Upon to the report by Nakatsuka et al., the series resistance of the device with PCE of 3.44% is about 15 Ω cm^2, which is almost ten times larger than that calculated from the resistivity and thickness of $ZnSnP_2$ bulk crystals used as absorbers. In addition, the roll-over behavior of the *J-V* curve of the device indicates the existence of a potential barrier at the interface between $ZnSnP_2$ absorbers and Cu back contact. Considering the difference of resistance between the Cu/$ZnSnP_2$ and Mo/$ZnSnP_2$ interfaces after annealing, the reactive diffusion is a key for the reduction of resistance. In Chapter 2, the Cu/$ZnSnP_2$ interfaces are re-investigated in detail and discuss the mechanism of the reduction of resistance.
2. Identification of the origin of small carrier lifetime: Studies of recombination behavior using CL by Berkovskii et al. and PL by Nakatsuka et al. indicate a short minority carrier lifetime of about sub-nano seconds. It becomes a significant problem in device performance. In Chapter 3, the Recombination behavior of carriers is investigated through the characterization of bulk crystals by DLTS and PL. In addition, experimental results are discussed based on defect properties calculated by Kumagai et al. to present the *compass* for device design.
3. Raman spectroscopy on $ZnSnP_2$ with various degrees of order: As mentioned above, the degree of order has a significant influence on the physical properties of $ZnSnP_2$. The degree of order of powder $ZnSnP_2$ was evaluated by standard XRD measurement as Nakatsuka and Nose demonstrated. However, XRD is less effective for anisotropic specimens like thin films due to orientation problems. In Chapter 4, we discussed non-polarized Raman spectra of bulk $ZnSnP_2$ with various degrees of order and discussed its possibility for the use of evaluating the degree of order of thin films.

4. Thin-film growth by MBE: The formation of Zn_3P_2 and protrusions in the phosphidation process suppress the PCE less than 0.1% for the thin-film solar cells of $ZnSnP_2$. Co-evaporation processes like MBE can be a solution for directly obtaining thin-film $ZnSnP_2$ without protrusions. In Chapter 5, we discuss the influence of growth temperature on the physical properties of thin-film $ZnSnP_2$.

References to Chapter 1

[1] “Projected Costs of Generating Electricity,” International Energy Agency and Organisation for Economic Co-operation and Development/Nuclear Energy Agency (2020).

[2] “World Energy Outlook 2021,” International Energy Agency, (2021).

[3] “Global Primary Energy Consumption by Source,” Our World in Data. https://ourworldindata.org/grapher/global-energy-consumption-source?country=~OWID_WRL (access; 7 Jan. 2022).

[4] “Leveraging Energy Action for Advancing the Sustainable Development Goals,” United Nations (2021).

[5] P. Breeze, “Power Generation Technologies 3rd Edition.” (Elsevier Newnes, Amsterdam, Oxford, 2019).

[6] “World Energy Resources 2013 Survey,” World Energy Counsil, (2013).

[7] W. Shockley, H. J. Queisser, “Detailed Balance Limit of Efficiency of p-n Junction Solar Cells,” *J. Appl. Phys.* **32**, 510 (1961).

[8] “Reference Air Mass 1.5 Spectra,” National Renewable Energy Laboratory. https://www.nrel.gov/grid/solar-resource/spectra-am1.5.html (access: 7 January 2022)

[9] J.L. Gray, “The Physics of the Solar Cell, in Handbook of Photovoltaic Science and Engineering,” edited by A. Luque, S. Hegedus (John Wiley & Sons, Ltd, Chichester, UK, 2005), pp. 61–112.

[10] B. Pamplin, "The Adamantine Family of Compounds," *Progress in Crystal Growth and Characterization* **3**, 179 (1980).

[11] M.A. Green, E.D. Dunlop, J. Hohl-Ebinger, M. Yoshita, N. Kopidakis, X. Hao, “Solar Cell Efficiency Tables (Version 58),” *Prog. Photovolt. Res. Appl.* **29**, 657 (2021).

[12] D.M. Chapin, C.S. Fuller, G. L. Pearson, “A New Silicon P-n Junction Photocell for Converting Solar Radiation into Electrical Power,” *J. Appl. Phys.* **25**, 676 (1954).

[13] “New World Record Established for Conversion Efficiency in a Crystalline Silicon Solar Cell —Conversion Efficiency of 26.63% Achieved in a Practical Cell Size—,” KANEKA Corporation, (2017). https://www.kaneka.co.jp/en/topics/news/nr201708252/ (access; 7 January 2022)

[14] “26.1% Record Efficiency for p-Type Crystalline Si Solar Cells,” Institut für Solarenergieforschung GmbH (2018). https://isfh.de/26-1-record-efficiency-for-p-type-crystalline-si-solar-cells/ (access; 7 January 2022)

[15] “Photovoltaics Report,” Fraunhofer ISE (2021).

[16] “Best Research-Cell Efficiency Chart,” National Renewable Energy Laboratory (2021). https://www.nrel.gov/pv/cell-efficiency.html (access; 7 January 2022)

[17] “State-of-the-Art Small Spacecraft Technology,” National Aeronautics and Space Administration, (2021).

[18] J.F. Geisz, R.M. France, K.L. Schulte, M.A. Steiner, A.G. Norman, H.L. Guthrey, M.R. Young, T. Song, and T. Moriarty, “Six-Junction III–V Solar Cells with 47.1% Conversion Efficiency under 143 Suns Concentration,” *Nat. Energy* **5**, 326 (2020).

[19] “Solar Frontier Achieves World Record Thin-Film Solar Cell Efficiency of 23.35%,” Solar Frontier (2019). https://www.solar-frontier.com/eng/news/2019/0117_press.html (access; 7 January 2022)

[20] “First Solar Achieves Yet Another Cell Conversion Efficiency World Record,” First Solar (2016). https://investor.firstsolar.com/news/press-release-details/2016/First-Solar-Achieves-Yet-Another-Cell-Conversion-Efficiency-World-Record/default.aspx (access; 7 January 2022)

[21] A. Zakutayev, J.D. Major, X. Hao, A. Walsh, J. Tang, T.K. Todorov, L.H. Wong, E. Saucedo, “Emerging Inorganic Solar Cell Efficiency Tables (Version 2),” *J. Phys. Energy* **3**, 032003 (2021).

[22] O. Almora, D. Baran, G.C. Bazan, C. Berger, C.I. Cabrera, K.R. Catchpole, S. Erten-Ela, F. Guo, J. Hauch, A.W.Y. Ho-Baillie, T.J. Jacobsson, R.A.J. Janssen, T. Kirchartz, N. Kopidakis, Y. Li, M.A.

Loi, R.R. Lunt, X. Mathew, M.D. McGehee, J. Min, D.B. Mitzi, M.K. Nazeeruddin, J. Nelson, A.F. Nogueira, U.W. Paetzold, N.-G. Park, B.P. Rand, U. Rau, H.J. Snaith, E. Unger, L. Vaillant-Roca, H.-L. Yip, and C.J. Brabec, "Device Performance of Emerging Photovoltaic Materials (Version 1)," *Adv. Energy Mater.* **11**, 2002774 (2021).

[23] W. Wang, M.T. Winkler, O. Gunawan, T. Gokmen, T.K. Todorov, Y. Zhu, D.B. Mitzi, "Device Characteristics of CZTSSe Thin-Film Solar Cells with 12.6% Efficiency," *Adv. Energy Mater.* **4**, 1301465 (2014).

[24] D.-H. Son, S.-H. Kim, S.-Y. Kim, Y.-I. Kim, J.-H. Sim, S.-N. Park, D.-H. Jeon, D.-K. Hwang, S.-J. Sung, J.-K. Kang, K.-J. Yang, D.-H. Kim, "Effect of Solid-H_2S Gas Reactions on CZTSSe Thin Film Growth and Photovoltaic Properties of a 12.62% Efficiency Device," *J. Mater. Chem. A* **7**, 25279 (2019).

[25] X. Wen, C. Chen, S. Lu, K. Li, R. Kondrotas, Y. Zhao, W. Chen, L. Gao, C. Wang, J. Zhang, G. Niu, J. Tang, "Vapor Transport Deposition of Antimony Selenide Thin Film Solar Cells with 7.6% Efficiency," *Nat. Commun.* **9**, 2179 (2018).

[26] R. Tang, X. Wang, W. Lian, J. Huang, Q. Wei, M. Huang, Y. Yin, C. Jiang, S. Yang, G. Xing, S. Chen, C. Zhu, X. Hao, M.A. Green, T. Chen, "Hydrothermal Deposition of Antimony Selenosulfide Thin Films Enables Solar Cells with 10% Efficiency," *Nat. Energy* **5**, 587 (2020).

[27] Z. Li, X. Liang, G. Li, H. Liu, H. Zhang, J. Guo, J. Chen, K. Shen, X. San, W. Yu, R.E.I. Schropp, Y. Mai, "9.2%-Efficient Core-Shell Structured Antimony Selenide Nanorod Array Solar Cells," *Nat. Commun.* **10**, (2019).

[28] Y.C. Choi, D.U. Lee, J.H. Noh, E.K. Kim, S.I. Seok, "Highly Improved Sb_2S_3 Sensitized-Inorganic-Organic Heterojunction Solar Cells and Quantification of Traps by Deep-Level Transient Spectroscopy," *Adv. Funct. Mater.* **24**, 3587 (2014).

[29] X. Wang, R. Tang, C. Jiang, W. Lian, H. Ju, G. Jiang, Z. Li, C. Zhu, T. Chen, "Manipulating the

Electrical Properties of $Sb_2(S,Se)_3$ Film for High-Efficiency Solar Cell," *Adv. Energy Mater.* **10**, 2002341 (2020).

[30] R. Katsube, "Investigation on Properties of Zinc Phosphide Related Materials and Interfaces for Optoelectronic Devices," Ph. D thesis (Kyoto University, 2018).

[31] J.L. Shay, J.H. Wernick, "Ternary Chalcopyrite Semiconductors, Growth, Electronic Properties, and Applications" (Pergamon Press, Oxford, 1975).

[32] A.D. Martinez, A.N. Fioretti, E.S. Toberer, A.C. Tamboli, "Synthesis, Structure, and Optoelectronic Properties of II–IV–V_2 Materials," *J. Mater. Chem. A* **5**, 11418 (2017).

[33] R.R. Schnepf, J.J. Cordell, M.B. Tellekamp, C.L. Melamed, A.L. Greenaway, A. Mis, G.L. Brennecka, S. Christensen, G.J. Tucker, E.S. Toberer, S. Lany, A.C. Tamboli, "Utilizing Site Disorder in the Development of New Energy-Relevant Semiconductors," *ACS Energy Lett.* **5**, 2027 (2020).

[34] C.H.L. Goodman, "A New Group of Compounds with Diamond Type (Chalcopyrite) Structure," *Nature* **179**, 828 (1957).

[35] A.A. Vaipolin, N.A. Goryunova, L.I. Kleshchinskii, G.V. Loshakova, E.O. Osmanov, "The Structure and Properties of the Semiconducting Compound $ZnSnP_2$," *Phys. Status Solidi B* **29**, 435 (1968).

[36] M.A. Ryan, M.W. Peterson, D.L. Williamson, J.S. Frey, G.E. Maciel, B.A. Parkinson, "Metal Site Disorder in Zinc Tin Phosphide," *J. Mater. Res.* **2**, 528 (1987).

[37] N.A. Goryunova, M.L. Belle, L.B. Zlatkin, G.V. Lashakova, A.S. Poplavnoi, V.A. Chaldyshev, "Optical Properties and Band Structure of $ZnSnP_2$ (Chalcopyrite and Sphalerite Modifications)," *Sov. Phys. Semiconduct.* **2**, 1126 (1969).

[38] Yu.V. Rud, I.A. Mal'tseva, "Anisotropy If the Luminescence of $ZnSnP_2$," *Sov. Phys. Semiconduct.* **11**, 612 (1977).

[39] M. Rubenstein, R.W. Ure, "Preparation and Characteristics of $ZnSnP_2$," *J. Phys. Chem. Sol.* **29**,

551 (1968).

[40] S. Nakatsuka, H. Nakamoto, Y. Nose, T. Uda, Y. Shirai, “Bulk Crystal Growth and Characterization of $ZnSnP_2$ Compound Semiconductor by Flux Method,” *Phys. Status Solidi C* **12**, 520 (2015).

[41] T. Yokoyama, F. Oba, A. Seko, H. Hayashi, Y. Nose, I. Tanaka, “Theoretical Photovoltaic Conversion Efficiencies of $ZnSnP_2$, $CdSnP_2$, and $Zn_{1-x}Cd_x SnP_2$ Alloys,” *Appl. Phys. Express* **6**, 061201 (2013).

[42] F.M. Berkovskii, D.Z. Garbuzov, N.A. Goryunova, G.V. LOSHAKOV, S.M. Ryvkin, G.P. Shpen’kov, “Radiative Recombination in $ZnSnP_2$ Crystals,” *Sov. Phys. Semiconduct.* **2**, 618 (1968).

[43] L.V. Kradinova, Z.A. Parimbekov, Yu.V. Rud’, “Effect of the Ordering of Atoms on the Radiative Properties of $ZnSnP_2$,” *Izv. Akad. Nauk SSSR, Neorg. Mater.* **23**, 154 (1987).

[44] S. Nakatsuka, N. Yuzawa, J. Chantana, T. Minemoto, Y. Nose, “Solar Cells Using Bulk Crystals of Rare Metal-Free Compound Semiconductor $ZnSnP_2$,” *Phys. Status Solidi A* **214**, 1600650 (2017).

[45] Y. Kumagai, M. Choi, Y. Nose, F. Oba, “First-Principles Study of Point Defects in Chalcopyrite $ZnSnP_2$,” *Phys. Rev. B* **90**, 125202 (2014).

[46] K. Nakatani, T. Minemura, K. Miyauchi, K. Fukabori, H. Nakanishi, M. Sugiyama, S. Shirakata, “Photoluminescence Property of $ZnSnP_2$ by Solution Growth and Normal Freezing Methods,” *Jpn. J. Appl. Phys.* **47**, 5342 (2008).

[47] S. Nakatsuka, Y. Nose, “Order–Disorder Phenomena and Their Effects on Bandgap in $ZnSnP_2$,” *J. Phys. Chem. C* **121**, 1040 (2017).

[48] Y. Nose, T. Uda, “Bulk Crystal Growth and Characterization of Chalcopyrite-Type Semiconductor $ZnSnP_2$ for Solar Cells,” *in Technical Digest of 21st International Photovoltaic Science and Engineering Conference*, Fukuoka, Japan 28 November–2 December 2011. 2D-3P-35.

[49] N.A. Goryunov, F.P. Kesamanly, and G.V. Loshakov, “Electrical Properties of $ZnSnP_2$ Crystals,”

Sov. Phys. Semiconduct. **1**, 844 (1968).

[50] D.O. Scanlon, A. Walsh, "Bandgap Engineering of $ZnSnP_2$ for High-Efficiency Solar Cells," *Appl. Phys. Lett.* **100**, 251911 (2012).

[51] I.P. Kaminow, E. Buehler, J.H. Wernick, "Vibrational Modes in $ZnSiP_2$," *Phys. Rev. B* **2**, 960 (1970).

[52] A.M. Mintairov, N.A. Sadchikov, T. Sauncy, M. Holtz, G.A. Seryogin, S.A. Nikishin, H. Temkin, "Vibrational Raman and Infrared Studies of Ordering in Epitaxial $ZnSnP_2$," *Phys. Rev. B* **59**, 15197 (1999).

[53] H. Liu, B. Zhao, Y. Yu, Z. He, J. Xiao, W. Huang, S. Zhu, B. Chen, L. Xie, "Theoretical Investigations on Elastic, Thermal and Lattice Dynamic Properties of Chalcopyrite $ZnSnX_2$ (X = P, As, Sb) under Pressure and Temperature: The First-Principles Calculation," *Int. J. Mod. Phys. B* **32**, 1850329 (2018).

[54] M. Bettini, "Zone-Centered Phonons in Ternary Compounds of Chalcopyrite Structure," *Phys. Status Solidi B* **69**, 201 (1975).

[55] L.B. ZLATKIN, J.F. Markov, A.I. Stekhanov, M.S. Shur, "Lattice Reflection and Optical Constants of $ZnSnP_2$ Crystals with Chalcopyrite and Sphalerite Structure," *Phys. Status Solidi* **32**, 473 (1969).

[56] F.W. Ohrendorf, H. Haeuseler, "Lattice Dynamics of Chalcopyrite Type Compounds. Part I. Vibrational Frequencies," *Cryst. Res. Technol.* **34**, 339 (1999).

[57] J. Łażewski, K. Parlinski, "Dynamical Properties of Pnictide $ZnSnP_2$ from Ab Initio Calculations," *J. Alloys Compd.* **328**, 162 (2001).

[58] T. Basak, M.N. Rao, S.L. Chaplot, "Order-Disorder Transition in $ZnGeP_2$ and $ZnSnP_2$," *J. Phys.: Conf. Ser.* **377**, 012071 (2012).

[59] G.A. Davis, C.M. Wolfe, "Liquid Phase Epitaxial Growth of $ZnSnP_2$ on GaAs," *J. Electrochem.*

Soc. **130**, 6 (1983).

[60] J. Sansregret, "The Growth of Thin Films of Zinc Tin Phosphide," *Mater. Res. Bull.* **16**, 607 (1981).

[61] P.K. Ajmera, H.Y. Shin, B. Zamanian, "Vacuum Growth of Thin Films of $ZnSnP_2$," *Solar Cells* **21**, 291 (1987).

[62] H.Y. Shin. P.K. Ajmera, "Characterization of Vacuum Grown Thin Films of $ZnSnP_2$," *Mater. Lett.* **5**, 211 (1987).

[63] H.Y. Shin, P.K. Ajmera, "Thin Films of $ZnSnP_2$: Vacuum Growth and Electrical Properties," *Mater. Lett.* **8**, 464 (1989).

[64] S. Francoeur, G.A. Seryogin, S.A. Nikishin, H. Temkin, "X-Ray Diffraction Study of Chalcopyrite Ordering in Epitaxial $ZnSnP_2$ Grown on GaAs," *Appl. Phys. Lett.* **74**, 3678 (1999).

[65] G.A. Seryogin, S.A. Nikishin, H. Temkin, A.M. Mintairov, J.L. Merz, M. Holtz, "Order–Disorder Transition in Epitaxial $ZnSnP_2$," *Appl. Phys. Lett.* **74**, 2128 (1999).

[66] S. Francoeur, G.A. Seryogin, S.A. Nikishin, H. Temkin, "Quantitative Determination of the Order Parameter in Epitaxial Layers of $ZnSnP_2$," *Appl. Phys. Lett.* **76**, 2017 (2000).

[67] P. St-Jean, G.A. Seryogin, S. Francoeur, "Band Gap of Sphalerite and Chalcopyrite Phases of Epitaxial $ZnSnP_2$," *Appl. Phys. Lett.* **96**, 231913 (2010).

[68] S. Mukherjee, T. Maitra, A. Nayak, S. Mukherjee, A. Pradhan, M. K. Mukhopadhyay, B. Satpati, S. Bhunia, "Microstructural and Light Emission Properties of $ZnSnP_2$ Thin Film Absorber: Study of Native Defects," *Mater. Chem. Phys.* **204**, 147 (2018).

[69] S. Mukherjee, T. Maitra, A. Pradhan, S. Mukherjee, G. Manna, S. Bhunia, A. Nayak, "Rapid Responsive Mg/$ZnSnP_2$/Sn Photodetector for Visible to near-Infrared Application," *Sol. Energy Mater. Sol. Cells* **189**, 181 (2019).

[70] S. Mukherjee, T. Maitra, A. Pradhan, S. Mukherjee, S. Bhunia, A. Nayak, "Probing Bias and

Power Dependency of High-Performance Broadband Mg/ZnSnP_2/Sn Back-to-Back Schottky Junction Photodetectors," *Sol. Energy Mater. Sol. Cells* **208**, 110386 (2020).

[71] S. Nakatsuka, Y. Nose, T. Uda, "Fabrication of ZnSnP_2 Thin Films by Phosphidation," *Thin Solid Films* **589**, 66 (2015).

[72] S. Akari, J. Chantana, S. Nakatsuka, Y. Nose, T. Minemoto, "ZnSnP_2 Solar Cell with (Cd,Zn)S Buffer Layer: Analysis of Recombination Rates," *Sol. Energy Mater. and Sol. Cells* **174**, 412 (2018).

[73] S. Nakatsuka, S. Akari, J. Chantana, T. Minemoto, Y. Nose, "Impact of Heterointerfaces in Solar Cells Using ZnSnP_2 Bulk Crystals," *ACS Appl. Mater. Interfaces* **9**, 33827 (2017).

[74] N. Yuzawa, J. Chantana, S. Nakatsuka, Y. Nose, T. Minemoto, "ZnSnP_2 Thin-Film Solar Cell Prepared by Phosphidation Method under Optimized Zn/Sn Atomic Ratio of Its Absorbing Layer," *Curr. Appl. Phys.* **17**, 557 (2017).

[75] Y. Hinuma, F. Oba, Y. Nose, I. Tanaka, "First-Principles Study of Valence Band Offsets at ZnSnP_2/CdS, ZnSnP_2/ZnS, and Related Chalcopyrite/Zincblende Heterointerfaces," *J. Appl. Phys.* **114**, 043718 (2013).

[76] S. Nakatsuka, K. Kazumi, Y. Nose, "A pn-Junction between Chalcopyrite Phosphide Semiconductors for Photovoltaic Application," *Jpn. J. Appl. Phys.* **58**, 075508 (2019).

[77] H.B. Michaelson, "The Work Function of the Elements and Its Periodicity," *J. Appl. Phys.* **48**, 4729 (1977).

2. Cu_3P back buffer layer for $ZnSnP_2$ solar cells

2.1. Introduction

Solar cells based on compound semiconductors such as chalcogenides and pnictides are one of the promising alternatives to silicon solar cells. Among various compounds, GaAs, CdTe and $Cu(In,Ga)Se_2$ (CIGS) have been well investigated and the conversion efficiencies of these compounds-based solar cells are over 20% [1–3]. On the other hand, the use of minor or toxic elements such as Ga, As, In, Cd, Te, and Se may disturb the further spread of solar cells. The alternative materials have been thus investigated intensely such as $Cu_2ZnSnS_{4-x}Se_x$ (CZTSSe) [4], Se [5], Cu_2SnS_3 [6], $CuSbSe_2$ [7], Cu_2O [8], SnS [9], FeS_2 [10], Sb_2Se_3 [11], Zn_3P_2 [12], and $ZnSnN_2$ [13]. As summarized in Table 2-1, however, the conversion efficiencies are still below 10 % except for CZTSSe.

Table 2-1. Efficiency and parameters for various solar cells are summarized based on the paper by Wong et al. [1], except for SnS [2] and Zn_3P_2 [3].

Absorber	Efficiency / %	V_{OC} / V	J_{SC} / mA cm^{-2}	FF / %	Year
Se	6.5	0.969	10.6	63.4	2017
Sb_2Se_3	9.2	0.400	32.6	70.3	2018
Cu_2O	8.1	1.10	11.5	60	2016
SnS [2]	4.8	0.33	24.7	58.5	2019
Cu_2SnS_3	4.3	0.258	35.6	46.7	2019
$CuSbSe_2$	4.7	0.336	26.3	53.0	2017
$Cu_2ZnSn(S,Se)_4$	12.6	0.513	35.2	69.8	2013
Zn_3P_2 [3]	4.5	0.41	21.4	51	2010
$ZnSnN_2$	1.5	0.360	7.5	57	2018
$ZnSnP_2$	3.87	0.535	12.1	59.8	2019

$ZnSnP_2$ (ZTP) has recently attracted much attention because of the earth-abundant constituents, the high absorption coefficient close to those of CdTe and GaAs in the visible region [15], and the bandgap controllable in 1.3–1.7 eV [16, 17]. The chalcogenide compounds are the mainstream in studies on compound solar cells, while pnictides including ZTP, Zn_3P_2, and $ZnSnN_2$ belong to a novel absorber family. Our group reported the preparation of ZTP thin films by phosphidation of Zn-Sn precursors; however, it was difficult to apply to devices due to the surface roughness [18]. Therefore, bulk crystals of ZTP obtained by a conventional solution growth using Sn flux were used for solar cells [19, 20]. The grain size is about 1 mm and the smooth surface can be prepared by mechanical polishing and chemical etching. In the last few years, solar cells using ZTP bulk crystals have been developed in our group and the highest conversion efficiency is 3.44 % for the cell structure with Al/Al:ZnO/ZnO/(Cd,Zn)S/ZTP/Cu [21]. Nakatsuka et al. applied Cu to back electrodes of ZTP solar cells for the first time and suggested that it is one of the key factors for the reduction of series resistance [22]. However, the way to optimize and the mechanism is still unclear.

In this work, we thus investigated the relationship between the structure and carrier transport properties at the Cu/ZTP interface and applied the knowledge to ZTP solar cells. In particular, we focused on the reactive diffusion and the formation of intermediate compounds, Cu3P, at the Cu/ZTP interface through heat treatment under various conditions. We already reported the preliminary results on Cu electrode characteristics and reactive diffusion [23]. In this paper, the detailed structure around the interface, the mechanism of resistance reduction and the device demonstration are discussed.

2.2. Investigation on Cu/$ZnSnP_2$ interface

2.2.1. Experimental procedures

ZTP bulk crystals were prepared according to our previous report [19]. Starting materials, zinc shots (99.9999 %, Kojundo Chemical Laboratory), tin shots (99.99 %, Kojundo Chemical Laboratory), and red phosphorus flakes (99.9999 %, Kojundo Chemical Laboratory) were sealed in evacuated quartz ampules with an inner diameter of 11 mm under a pressure of 10^{-2} Pa. The overall weight of the materials was about 60 g, and the nominal molar composition was 92 mol%Sn, 2.7 mol%Zn, and 5.3 mol%P. The ampules were then heated up to 700 °C and kept for 12 hours for homogenization. After homogenization, the ampules were unidirectionally cooled from the bottom with a rate of 12 °C day^{-1}. The obtained ingots were cut into wafers with a thickness of about 1 mm using a diamond wheel saw.

Cu electrodes were deposited on the etched surface of ZTP wafers by DC sputtering using Cu target (Furuuchi Chemical). Before the deposition, the surface of the wafers was polished with a series of emery papers and finally with 1 μm diamond slurry on a buff sheet, and then etched in 1/2 diluted aqua regia for 5 min to remove a damaged layer by mechanical polishing. Subsequently, the wafers were ultrasonic-cleaned by sequential 1/4 diluted hydrochloric acid and ultrapure water. Shadow masks with two circle windows were used for the deposition of two electrodes on the surface. The diameter of the windows and their distance were both 1.5 mm. The power density, the working pressure of Ar gas, and the duration during sputtering were 4 W cm^{-2}, 0.8 Pa, and 120 min, respectively, so that the thickness of electrodes was about 500 nm. For Cu/Cu_3P/ZTP specimens, Cu_3P was deposited on ZTP wafers by DC sputtering through the shadow mask prior to Cu deposition. A sputtering target of Cu_3P with a diameter of 1 inch was prepared by cutting out from a Cu-P ingot (15 wt%P, Osaka Alloy Works Co. Ltd.). During sputtering, the power density, the working pressure, and the duration were set at 6 W cm^{-2}, 3.0 Pa, and 5 min, respectively, to control the thickness of Cu_3P to 20 nm. The deposition of Cu on Cu_3P was also carried out by the same conditions as described above. Some of Cu/ZTP and Cu/Cu_3P/ZTP specimens were annealed at 400 ºC for 5−60 min in evacuated quartz ampules under a pressure of 10^{-2} Pa. The ampules were quenched into water after annealing.

The current-voltage (*I-V*) characteristics of Cu/ZTP and Cu/Cu_3P/ZTP specimens before and after annealing were evaluated by a source meter (2400, Keithley). The cross-sectional microstructure of Cu/ZTP and Cu/Cu_3P/ZTP interfaces were investigated by scanning transmission electron microscopy (STEM, JEM-2100F, JEOL) equipped with energy-dispersive X-ray spectroscopy (EDS, JED2300T, JEOL). Selected area electron diffraction (SAED) patterns were also obtained by the same equipment. Specimens for STEM observations were prepared by focused ion beam (FIB, JFIB2300, JEOL) with Ga^+ ion beam accelerated at 5.5 keV. The surface morphology of specimens was observed by scanning electron microscopy (SEM, JCM-6000Plus, JEOL), and the corresponding elemental distribution was analyzed by EDS (JED-2300 Series, JEOL). The work function and the ionization potential were evaluated by a photoelectron yield spectroscopy system (PYS, BIP-KV201, Bunkoukeiki). The performance of ZTP solar cells was evaluated under air-mass 1.5 global (AM 1.5G) illumination with 100 mW cm^{-2} using a system with a solar simulator (OTENTO-SUN II, Bunkoukeiki) together with the dark condition. The external quantum efficiency (EQE) spectra were obtained by a measurement system (SM-250, Bunkoukeiki). The relationship between capacitance and a bias voltage of the cells was examined in the dark conditions at room temperature by Probe Station (PS-100, Lake Shore Cryotronics) and LCR meter (E4980A, Agilent). The repetition rate and amplitude were 10 kHz and 10 mV, respectively.

2.2.2. Microstructure around interface and carrier transport behavior

Figure 2-1 shows the cross-sectional STEM-dark field (DF) images and the corresponding EDS mappings of Cu, Zn, Sn, and P for Cu/ZTP specimens before and after annealing at 400 °C. The white region shows Cu film in the DF image of Fig. 2-1(a), while ZTP is at the bottom side. The dark area was observed between Cu and ZTP, which might be sputtered during the FIB process for the preparation of specimens. In the case before annealing, it is speculated that chemical bonding at the interface was not strong, and then some atoms were sputtered during the FIB process. Hence, we considered that no interdiffusion occurred before the FIB process. As shown in Figs. 2-1(b) and (c), structural changes are recognized around the interface after annealing, where diffusion of Zn and Sn from ZTP to Cu side is observed. The formation of an intermetallic compound, Cu_3Sn, was suggested by EDS composition analyses in the area such as white particles and top layer in Fig. 2-1(c), where Sn and Cu were both detected. On the other hand, both Cu and P were detected in the white-grey regions in the DF images after annealing. The composition analysis and SAED patterns indicated the formation of Cu_3P as described below. Figures 2-2(a) and (b) show SAED patterns obtained from the white-grey and ZTP regions. The former pattern is well assigned to [1100] zone axis of Cu_3P [24], which coincides with the results of the composition analysis. In our previous paper [22], such reaction products were not observed, and the interdiffusion of Cu, Sn, and P might be at an early stage of the formation of Cu_3P and Cu_3Sn.

The discussion on the structure around Cu_3P/ZTP interface can also be derived from SAED patterns. The SAED pattern taken on the ZTP region shown in Fig. 2-2(b) is well-indexed to the [110] zone axis of ZTP. Arrays of the diffraction spots highlighted by orange boxes in Figs. 2-2(a) and (b) are systematic reflections of 000l for Cu_3P and 112 for ZTP, respectively, and they are parallel to each other. This means that (0001) plane of Cu_3P is parallel to (112) plane of ZTP, and hence there is an epitaxial relationship of Cu_3P [1100](0001) // ZTP [110](112) because these patterns were obtained with the incident electron beam with the same direction. In fact, the area of Cu_3P shown by white-grey in the STEM-DF images is certainly beside ZTP regions. We further discuss the orientation relationship between Cu_3P and ZTP from the viewpoint of lattice matching. Figures 2-2(c) and (d) show atomic arrangements of Cu_3P (0001) and ZTP (112) planes, respectively. Although Cu, Zn, and Sn atoms are on slightly-displaced planes from the phosphorus sublattice plane, they are displayed in the figures for easy understanding. The arrangements of phosphorus atoms in both planes are almost the same, and the distances between the first nearest neighbor phosphorus atoms are 4.02 Å for Cu_3P

[24] and 4.00 Å for ZTP [25], calculated from lattice constants. The lattice mismatch calculated from phosphorus sublattice is thus less than 0.5%, and a lattice-matched epitaxial interface between Cu_3P and ZTP can be understood.

Figures 2-3(a) and (b) show *I*-*V* characteristics of Cu/ZTP specimens before and after annealing at 400 ºC. Each curve is labeled from A to D corresponding to the specimens with each annealing period: 5, 15, 30, and 60 min, respectively. It is noticed that *I*-*V* curves before annealing seem slightly different, although they should be originally consistent with each other because of the same preparation procedure. There are some variations among specimens; however, it is not a matter since the effects of annealing on *I*-*V* curves are discussed in this study. The nonlinear relationship is confirmed in *I*-*V* curves before annealing shown in Fig. 2-3(a), and an effect of a potential barrier is considered at the Cu/ZTP interface. It is understood that the annealing enhanced the current by one order in every specimen paying attention to the vertical axes in Fig. 2-3(b), and the linearity of the *I*-*V* characteristics is enhanced, which suggests that the carrier transport behavior changes from Schottky to Ohmic resulting in reducing resistance. In the specimens with annealing for 15 and 30 min, labeled B and C, the formation of Cu_3P was confirmed in the cross-sectional STEM observation as described above and it affects the change of *I*-*V* characteristics. The resistances evaluated by linear regression to the *I*-*V* curves in the range from −0.5 to 0.5 V are shown in Fig. 2-3(c). The average value before annealing is shown by a blue dashed line. The annealing clearly makes the reduction of resistance and the lowest was obtained when annealing for 30 min. On the other hand, the resistance in the case of annealing for 60 min is higher than that for 30 min. One of the important factors is the microstructure at the surface. As shown in Fig. 2-4, the formation of Cu_3P is considered even in the specimen with annealing for 60 min since the white-grey regions are confirmed in the DF image, while areas consisting of metals at the surface are inhomogeneous. Such microstructure is also observed for the specimen with annealing for 30 min, which showed the lowest resistance. The surface morphology of each specimen was observed as shown in Fig. 2-5 and the areas without detecting metals such as Cu and Sn are outstanding with increasing annealing period. The decrease of such areas leads to the reduction of electrode areas, resulting in higher resistance. The inhomogeneity of metal areas might come from the aggregation of Cu; however, it is surprising that the surface diffusion of Cu occurs at 400 ºC, a much lower temperature than the melting point, 1085 ºC. The impact of Sn with the lower melting point, which diffused from ZTP, is speculated and further investigation is necessary.

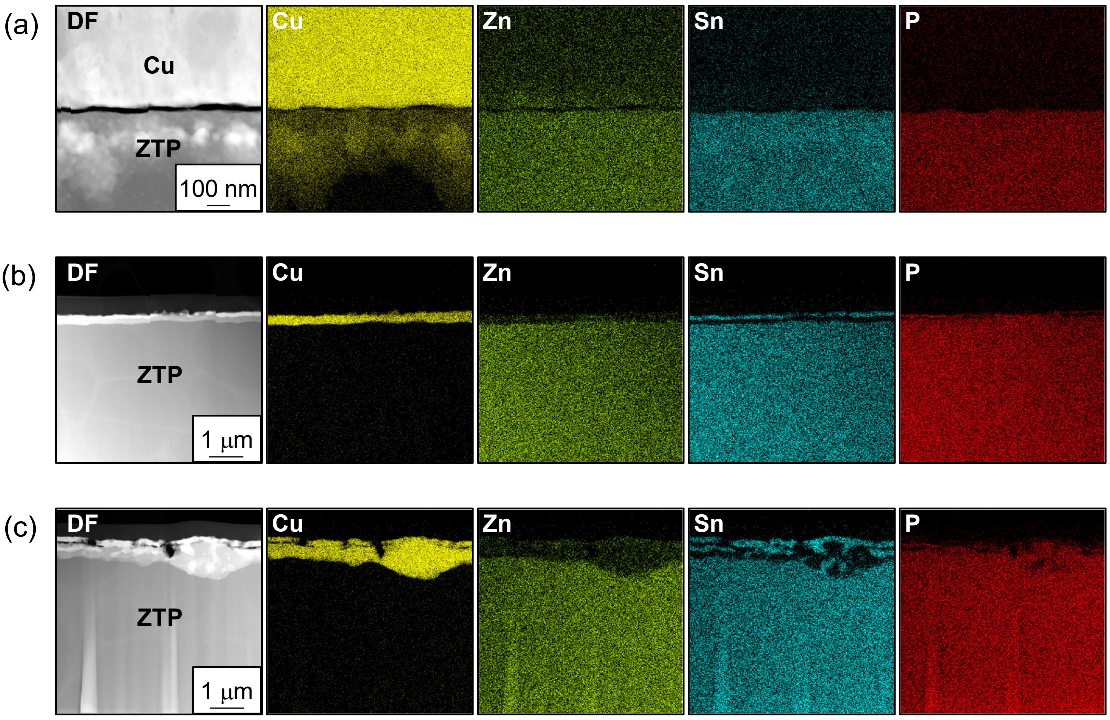

Figure 2-1. Cross-sectional STEM-DF images and corresponding EDS mappings of Cu, Zn, Sn, and P for Cu/ZTP specimens (a) before and after annealing at 400 ºC for (b) 15 and (c) 30 min.

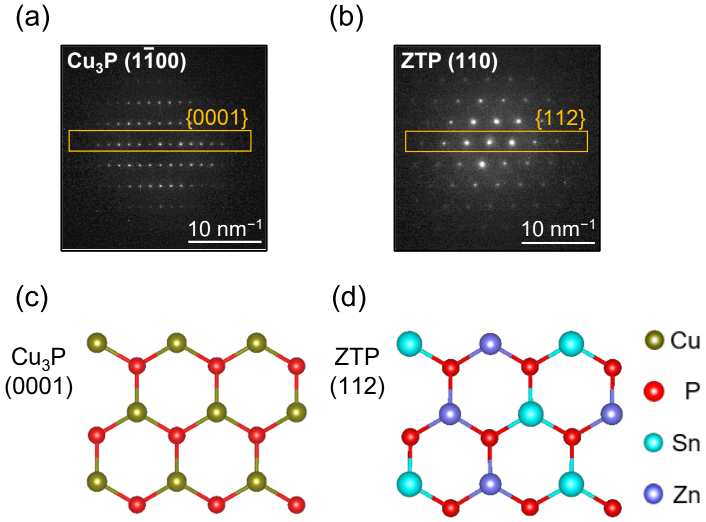

Figure 2-2. SAED patterns taken from (a) Cu_3P and (b) ZTP regions at the interface in Cu/ZTP specimen annealed at 400 ºC for 15 min. Atom configurations of (c) Cu_3P (0001) and (d) ZTP (112) planes.

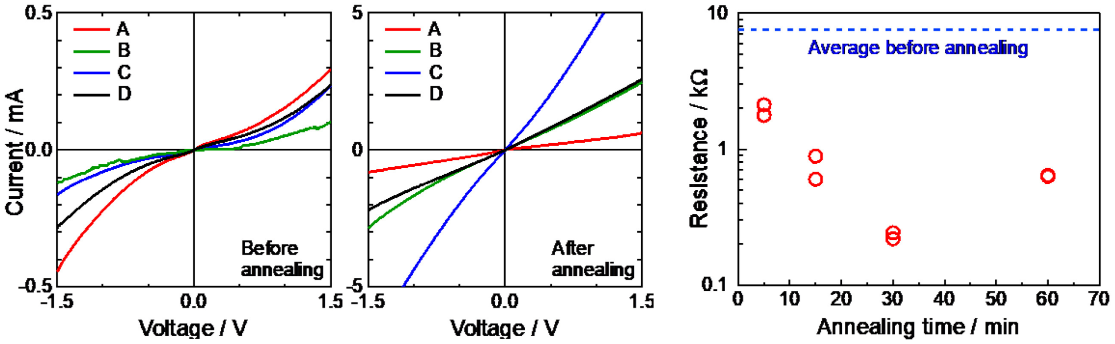

Figure 2-3. *I-V* characteristics of Cu/ZTP specimens (a) before and (b) after annealing at 400 ºC. Each curve is labeled from A to D corresponding to the annealing period, 5, 15, 30, and 60 min, respectively. (c) Resistance evaluated from *I-V* curves.

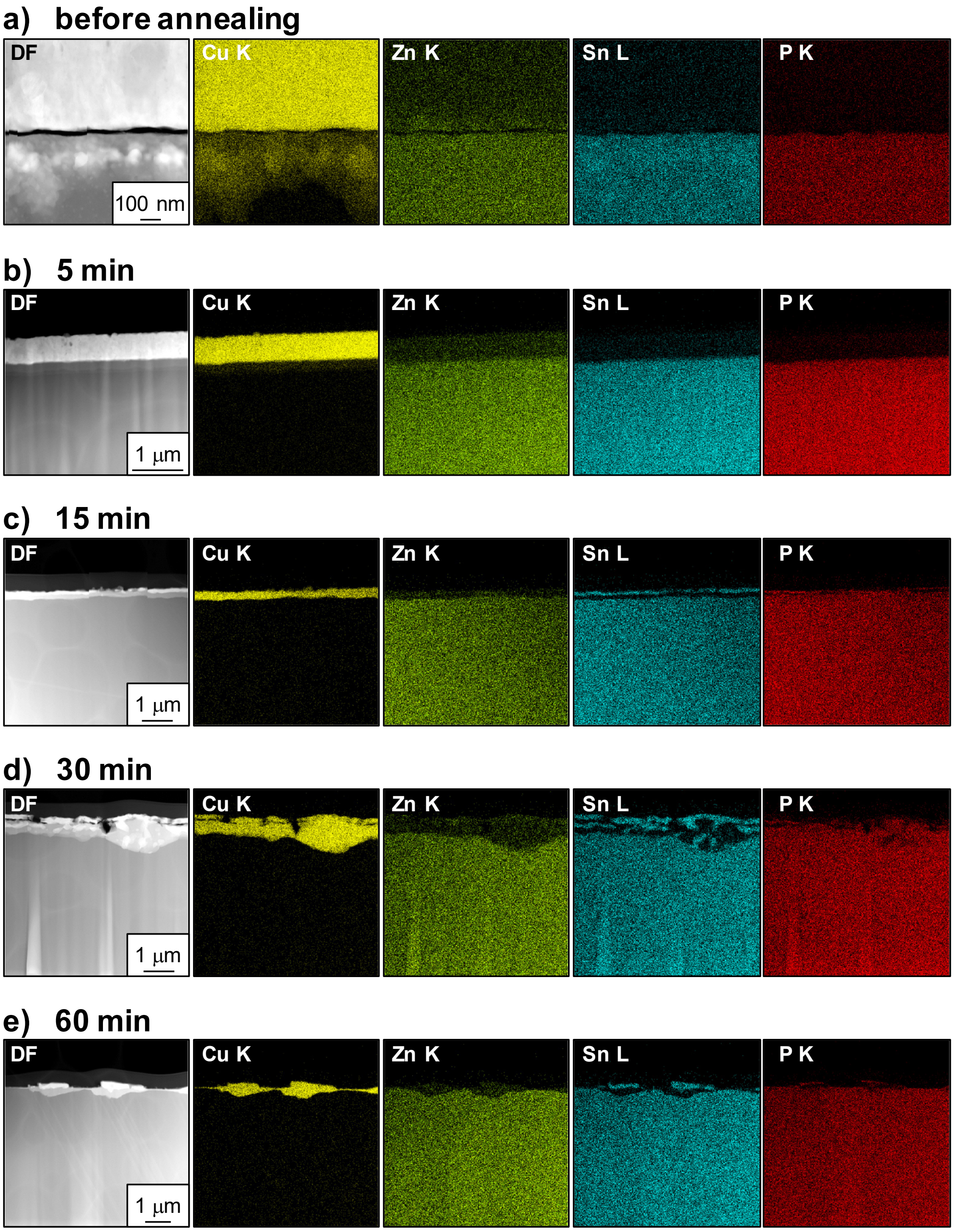

Figure 2-4. Cross-sectional STEM-DF images and corresponding EDS mappings of Cu, Zn, Sn, and P for Cu/ZTP specimens (a) before and after annealing at 400 °C for (b) 5, (c) 15, (d) 30, and (e) 60 min.

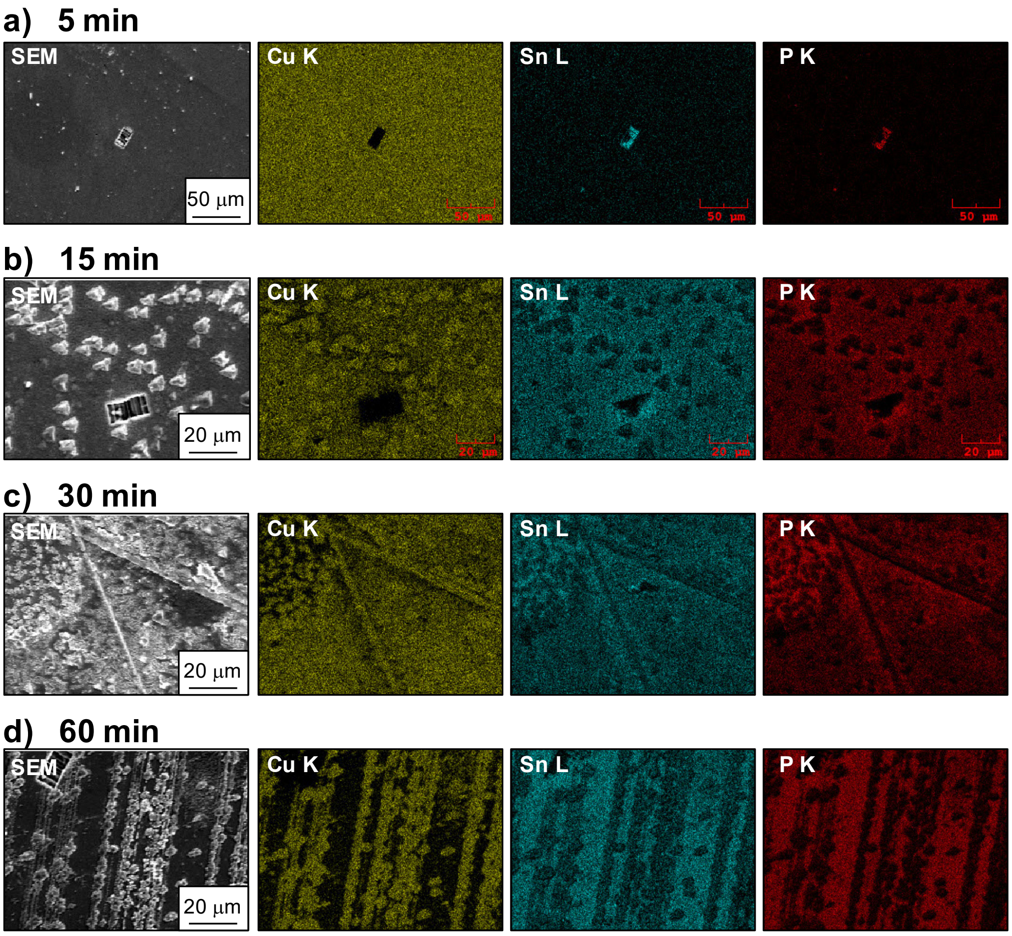

Figure 2-5. SEM images and corresponding EDS mappings of Cu, Sn, and P on the surfaces of Cu/ZTP specimens after annealing at 400 °C for (a) 5, (b) 15, (c) 30, and (d) 60 min.

2.2.3. Band alignment of Cu_3P and $ZnSnP_2$

Concerning carrier transport at the interface, not only structural features but also electrical aspects of Cu_3P should be discussed. The electrical properties of Cu_3P films on glass substrates such as resistivity, carrier concentration, and mobility were evaluated to be 8.12×10^{-4} Ω cm, 1.43×10^{23} cm^{-3} and 0.205 cm^{2} V^{-1} s^{-1}, respectively, through Hall effect measurements. For the measurements, Cu_3P films were prepared on glass substrates by RF-sputtering. The type of majority carrier was difficult to be determined and a quite high carrier concentration suggests that the Cu_3P film has metallic or a degenerated semiconducting behavior at around room temperature. In the previous works, Robertson et al. described a single crystal of Cu_3P was metallic with a resistivity of 5×10^{-5} Ω cm [26], and Wolff et al. concluded that sintered Cu_3P showed a p-type conductivity with the carrier concentration of 3×10^{21} cm^{-3} [27]. Figure 2-6(a) shows the results of photoelectron yield spectroscopy (PYS) measurements for ZTP and Cu_3P powders. We here considered Cu_3P to be metallic and evaluated the work function to be 5.2 eV, which is consistent with the report by Manna et al. [28]. They recognized Cu_3P as a semiconductor and investigated that the bandgap and ionization potential of Cu_3P were 1.4 eV and 5.2 eV, respectively, through scanning tunneling microscope (STM)-based *I-V* measurements. On the other hand, the ionization potential for ZTP was 5.25 eV. Consequently, the band positions for both compounds are expressed as shown in Fig. 6(b), and the ionization potential of ZTP and the work function of Cu_3P are comparable. In other words, the level of valence band maximum (VBM) of ZTP and the Fermi level of Cu_3P are similar, expecting the small potential barrier against hole transport at Cu_3P/ZTP interface because the Fermi level of ZTP is located near VBM as shown in Fig 2-6(c). In our previous work, the potential barrier (band offset) between ZTP and CdS was evaluated to be 2.0 eV by XPS analysis [29], while it was also reported that the offset between Cu_3P and CdS was 1.9 eV by Manna et al. The band diagram shown in Fig. 2-6(b) can also be understood from these results based on CdS.

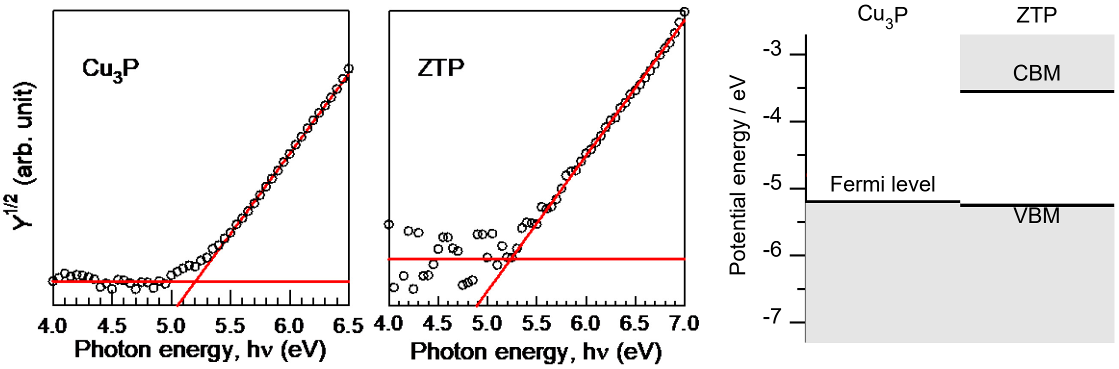

Figure 2-6. (a) PYS spectra and (b) band positions of ZTP and Cu_3P. Bandgap of ZTP is referred to the previous photoluminescence study by Nakatsuka et al. [20].

2.3. Fabrication of $ZnSnP_2$ solar cells with Cu_3P inserted

2.3.1. Experimental procedures

The cell structure was referred to our previous reports [21, 22]. The back electrode of Cu with and without Cu_3P was prepared on the polished and etched surface of ZTP wafers by the same procedure described in the previous section, where the annealing conditions were 400 °C for 5 min in evacuated quartz ampules. After that, each wafer was attached to a glass substrate to easily handle in the later procedure. The electrode side was in contact with the glass substrate with a pinhole with a diameter of 1 mm for a pathway to the back electrode. The opposite surface of the ZTP wafer was mechanically polished until the wafer thickness of 200–300 μm. The polished surface was etched by 1/2 diluted aqua regia for 15 min and then ultrasonic-cleaned by ultrapure water. An *n*-type buffer material, CdS was deposited by the chemical bath deposition (CBD) method. The solution was prepared using 11 mmol L^{-1} $CdSO_4$, 2.3 mol L^{-1} ammonia, and 56 mmol L^{-1} thiourea. The temperature for the deposition was 80 °C so that the typical thickness of CdS was 50 nm. The window layer ITO was deposited on CdS by RF sputtering using an ITO target prepared by sintering the mixture of In_2O_3 (99.99%, Kojundo Chemical Laboratory) and SnO_2 powders (99.99%, Kojundo Chemical Laboratory). The power density, the working pressure, and the duration were 2 W cm^{-2}, 0.55 Pa, and 120 min, respectively. The thickness and the typical resistivity of ITO film were 250 nm and 10^{-3} Ωcm. Finally, Al grid electrodes were prepared by thermal evaporation of Al wire (99.999%, The Nilaco Corporation) under the pressure of 10^{-3} Pa.

2.3.2. Effect of inserting Cu_3P

As discussed in the previous section, the formation of Cu_3P at the interface is an advantage for carrier transport from the viewpoints of lattice and band alignments. On the other hand, the annealing to obtain low resistance led to Cu agglomeration and inhomogeneity of the electrode. It seems originally difficult to prepare a uniform Cu_3P layer with reactive diffusion between Cn and ZTP. We thus considered making Cu/Cu_3P/ZTP structure by intentional deposition of Cu_3P. Figure 2-7 shows *I-V* characteristics for Cu/Cu_3P/ZTP specimens, in which Cu_3P film was prepared on ZTP wafer by DC sputtering before Cu deposition. The *I-V* characteristics for both Cu/ZTP and Cu/Cu_3P/ZTP specimens before annealing are similar, although the current in specimens with Cu_3P is slightly higher. In the case of Cu/ZTP specimens discussed above, the annealing for 30 min was necessary to obtain the lowest resistance, and no significant improvement was observed by annealing only for 5 min. On the other hand, it was confirmed that the current and the linearity were expressly enhanced even after annealing for 5 min in Cu/Cu_3P/ZTP specimens, and the resistances after annealing for 5 and 30 min are the same in level. The annealing for reactive diffusion might not be needed for a long period by inserting Cu_3P in advance, resulting in keeping a homogeneous Cu electrode. Consequently, we investigated the cross-sectional structures around the Cu/Cu_3P/ZTP interface before and after annealing for 5 min as shown in Figure 2-8. Figure 2-9 also shows the SEM images of the surface for Cu/Cu_3P/ZTP specimens after annealing. A part of the impact of inserting Cu_3P on Cu aggregation was already reported by our group [30]. The thickness of the Cu_3P layer and Cu electrode before annealing was about 25 nm and 500 nm, respectively, while the reacted region extended to 400–500 nm of thickness by annealing only for 5 min. The top layer with 30–40 nm consisting of metals such as Cu, Zn, and Sn was uniformly formed. The faceting was confirmed at the interface between reacted region and ZTP. The facet plane of ZTP is in contact with the Cu_3P region, which is understandable considering the epitaxial relationship between them as discussed above. In the middle region, the distribution of two types of metallic phases such as Cu-Zn-Sn and Cu-Sn regions was observed in the Cu_3P matrix; metallic phases and Cu_3P are recognized as white and light grey regions, respectively, also in the DF image. Here, it is surprising that the complicated microstructure formed by a short annealing period, 5 min. In the case of Cu/ZTP specimens, annealing for more than 15 min was necessary to obtain reacted region with the thickness of a few hundred micrometers. It is thus concluded that Cu_3P works as rather a diffusion promotor, although it was considered to suppress the reactive diffusion. In particular, the region of Cu_3P extended compared to the case before annealing, and it is speculated that ZTP reacted with Cu to form metallic phases and Cu_3P.

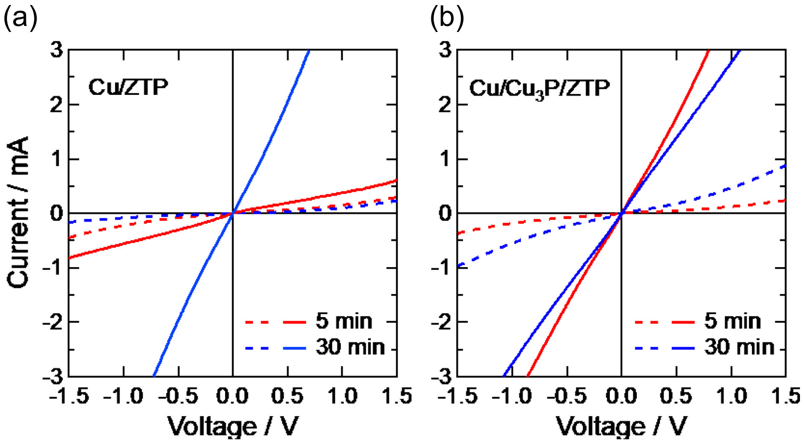

Figure 2-7. ***I-V*** **curves of (a) Cu/ZTP and (b) $Cu/Cu_3P/ZTP$ specimens before and after annealing at 400 °C for 5 and 30 min. Solid and dashed lines represent before and after annealing, respectively. Results before annealing are shown by dotted curves.**

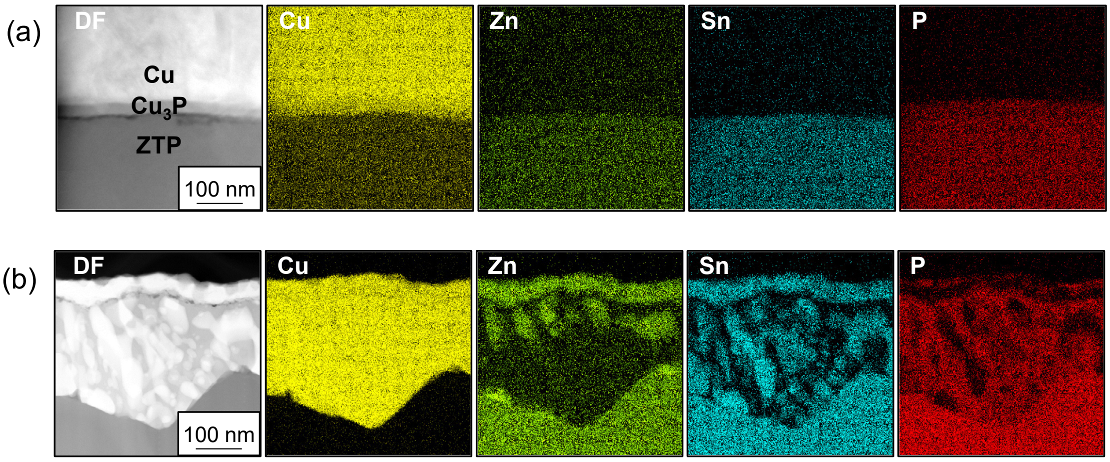

Figure 2-8. Cross-sectional STEM-DF images and corresponding EDS mappings of Cu, Zn, Sn, and P for $Cu/Cu_3P/ZTP$ specimens (a) as prepared and (b) after annealing at 400 °C for 5 min.

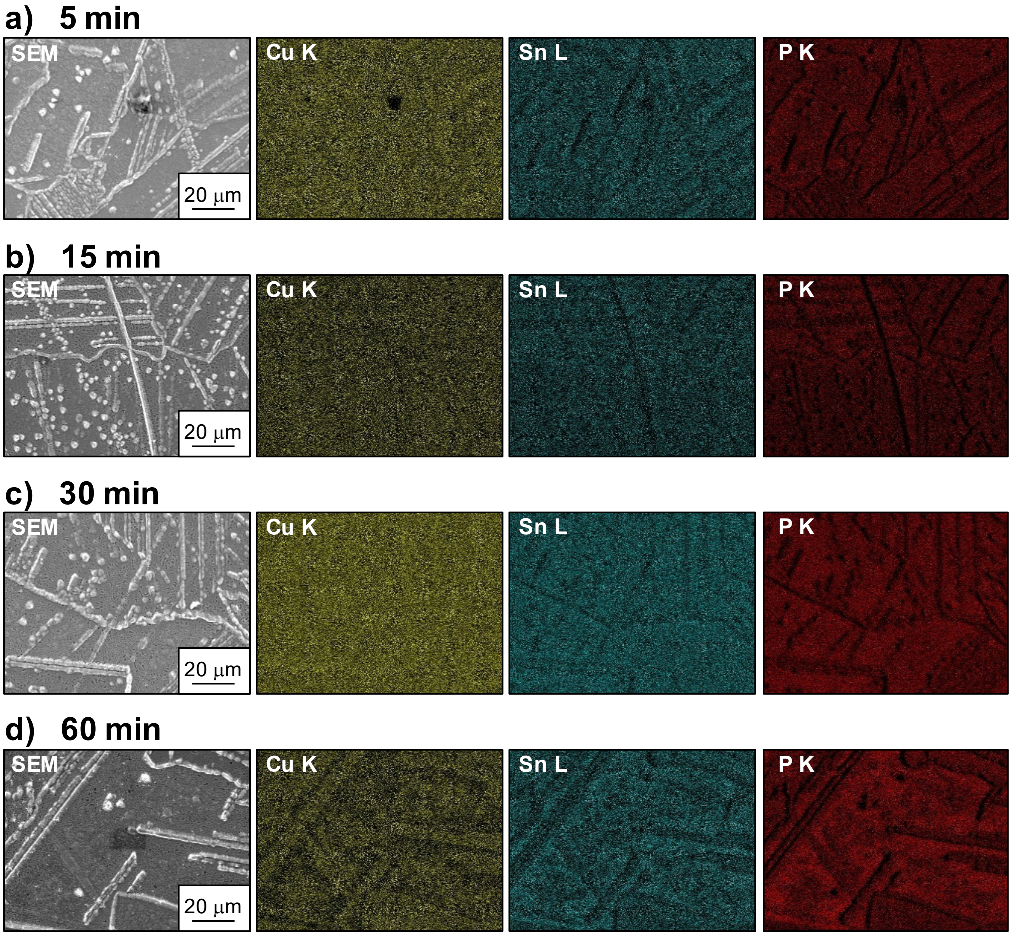

Figure 2-9. SEM images and corresponding EDS mappings of Cu, Sn, and P on the surfaces of Cu/Cu_3P/ZTP specimens after annealing at 400 ºC for (a) 5, (b) 15, (c) 30, and (d) 60 min.

2.3.3. Demonstration on devices

Furthermore, the benefit of inserting Cu_3P is applied to solar cell devices. We demonstrated solar cells with the structure of Al/ITO/CdS/ZTP/Cu_3P/Cu. The annealing condition for back electrodes was 400 °C for 5 min. CdS was selected as a partner material because n-type materials with suitable conductivity other than CdS could not be prepared in this study. Although our previous work indicated that the offset of conduction band minimum (CBM) between ZTP and CdS is as large as about 1.2 eV [29], the aim of this work is the investigation of the interface between ZTP and back electrode. Figure 2-10 shows dark and illuminated *J*-*V* characteristics of solar cells with and without

Cu_3P intentionally inserted between Cu and ZTP. The active area of the cell with Cu_3P insertion was evaluated to be 12.53 mm^2 from the photo by image analysis and measurement software. In the case without inserting Cu_3P, the *J-V* curve under illuminated shows roll-over in forward bias, resulting in that a cross-over behavior with the curve under dark condition was observed, as confirmed in our previous cells [21, 22]. Such behavior was also confirmed in CdTe/Au back contact in CdTe solar cells [31]. On the other hand, the *J-V* characteristics in the cells with Cu_3P by sputtering are closer to an ideal diode curve, and the current density was enhanced. This is also understood from EQE spectra discussed later, where it is recognized that the carrier collection is remarkably enhanced in the whole wavelength range. This improvement comes from the reduction of a Schottky barrier at the back electrode side, and the series resistance was actually reduced to 1.5 Ω cm^2. The short-circuit current density, the open-circuit voltage, and the fill factor are 12.1 mA cm^{-2}, 0.535 V, and 0.598, respectively, and every cell parameter was improved compared to cells without Cu_3P inserting. Consequently, the best conversion efficiency of 3.87 % has been achieved. The impact of inserting Cu_3P also leads to good reproductivity shown in Figure 2-11, where the efficiency of every cell with the same structure was around 3%. As observed in CdTe solar cells, a back contact should be controlled to be Ohmic with low resistance for higher efficiency. Wu et al. investigated the effects of Cu_xTe back contact on device performance and demonstrated that the control of Cu_xTe phases is critical for *J-V* curves [32]. In CIGS solar cells, it was suggested that the formation of $MoSe_x$ was self-organizing with lattice-matched to CIGS during the deposition of CIGS on Mo [33], which must be a key to achieve an Ohmic contact between CIGS and Mo back electrode. In the practical devices as seen above, suitable materials contribute to back contacts, which is also considered as a *back buffer* because they play as a *connector* in between absorber and back electrode. In ZTP solar cells, Cu_3P is really a *back buffer* material for the Cu back electrode.

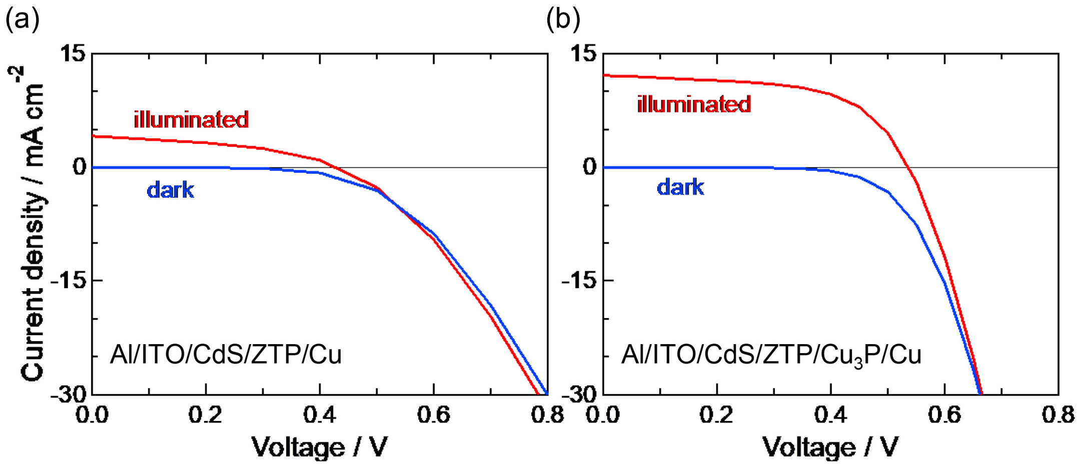

Fig. 2-10. ***J-V*** **characteristics of solar cells (a) without and (b) with inserting Cu_3P.**

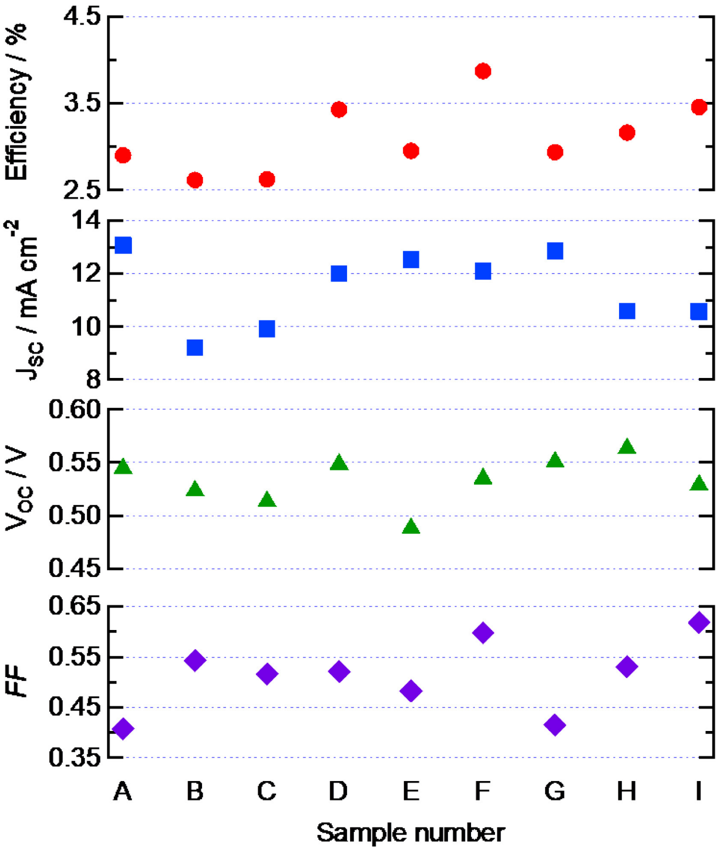

Figure 2-11. Efficiencies, short circuit current densities (J_{SC}), open-circuit voltages (V_{OC}), and fill factor (*FF*) of ZTP solar cells with the structure of Al/ITO/CdS/ZTP/Cu_3P/Cu fabricated in this study.

EQE spectra under various biases are also shown in Figure 2-12, where Cu_3P/Cu and Al/ITO respectively correspond to positive and negative electrodes as schematically shown in Figure 2-13. The bias-dependence of EQE indicates that the carrier collection, particularly in the range of longer wavelength, is needed to be further improved in ZTP solar cells even with Cu_3P inserted. Figure 2-14 shows the Mott-Schottky plot of the ZTP solar cell with the highest conversion efficiency. The built-in potential and the depletion width were evaluated by the Mott-Schottky analysis using the following equation for heterojunction [34].

$$\frac{A^2}{C^2} = \frac{2(\varepsilon_{\mathrm{ZTP}} N_a + \varepsilon_{\mathrm{CdS}} N_d)}{q \varepsilon_0 \varepsilon_{\mathrm{ZTP}} \varepsilon_{\mathrm{CdS}} N_a N_d} (\phi_{bi} - V), \tag{2-1}$$

where C is measured capacitance, A is the area of *pn*- junction corresponding to an active area of the cell in this work, ϕ_{bi} is the built-in potential, and V is bias voltage. The built-in potential was 1.16 V obtained from the intercept of the bias voltage axis, and it is larger compared to the cell showing the efficiency of 3.44 % reported in the previous paper: 0.75 V [21]. This indicates that the potential around *pn*-junction was not adequately evaluated in the previous paper due to the Schottky-like behavior at the interface between ZTP and Cu back electrode, while the built-in potential in the present cell is nearly ideal considering the bandgap of ZTP. Here, the slope of the regression line in the Mott-Schottky plot is expressed by b, and then we can obtain the following expression of the net concentration of ionized acceptor defects in p-region N_a,

$$N_a = \frac{2\varepsilon_{\mathrm{CdS}} N_d}{(bq\varepsilon_0 \varepsilon_{\mathrm{CdS}} N_{\mathrm{d}} - 2)\varepsilon_{\mathrm{ZTP}}}, \tag{2-2}$$

where q is the elementary charge and ε_0 is the vacuum permittivity. The relative dielectric constant of CdS $\varepsilon_{\mathrm{CdS}}$ is 5.4 [34,35], and that of ZTP $\varepsilon_{\mathrm{CdS}}$ was obtained to be 9.52 from the results calculated by Kumagai et al. [36]. They evaluated the dielectric tensor by first-principles calculation using HSE06. Assuming that the net concentration of ionized donor defects in n-region N_d is 1 ×10^{18} cm^{-3}, N_a is calculated to be 3.9 ×10^{17} cm^{-3}, which is reasonable considering the hole concentration of ZTP bulk crystals of 10^{16}–10^{17} cm^{-3} [19]. Furthermore, the depletion widths of p- and n-regions, W_p and W_n, around heterojunction are expressed by the following equations [34],

$$W_p = \sqrt{\frac{2N_d \varepsilon_0 \varepsilon_{\mathrm{ZTP}} \varepsilon_{\mathrm{CdS}} \phi_{bi}}{qN_a(\varepsilon_{\mathrm{ZTP}} N_a + \varepsilon_{\mathrm{CdS}} N_d)}}, \tag{2-3}$$

$$W_n = \sqrt{\frac{2N_a \varepsilon_0 \varepsilon_{\mathrm{ZTP}} \varepsilon_{\mathrm{CdS}} \phi_{bi}}{qN_d(\varepsilon_{\mathrm{ZTP}} N_a + \varepsilon_{\mathrm{CdS}} N_d)}}. \tag{2-4}$$

The depletion widths of *p*- and *n*-regions were calculated to be 43 and 17 nm, respectively, using the above built-in potential and defect concentrations. This is comparable to other solar cell devices with inorganic compound absorbers.

In this work, the issue on the interface between ZTP and Cu back electrode has been solved by inserting Cu_3P, and the impact of *pn*-junction with CdS on lower cell performance might not be high. Therefore, for the further improvement of cell performance, detailed re-investigation on bulk properties such as minority carrier lifetime in addition to interfaces is necessary.

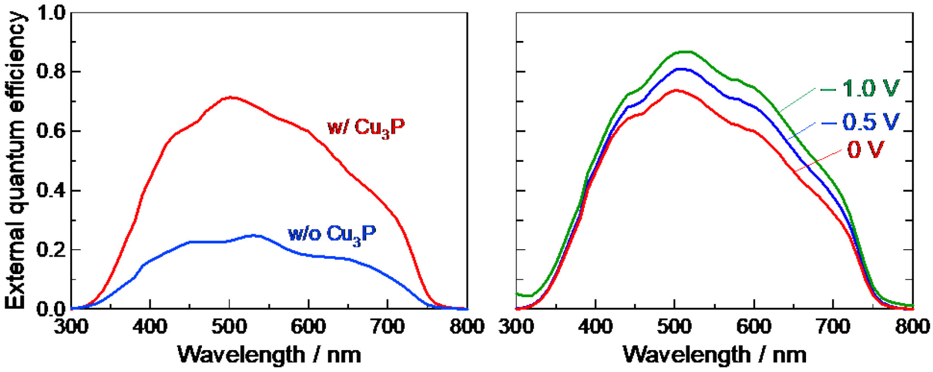

Figure 2-12. (a) EQE spectra of ZTP solar cells with and without inserting Cu_3P. (b) EQE spectra of the soalr cell with Cu_3P insertion under various biases.

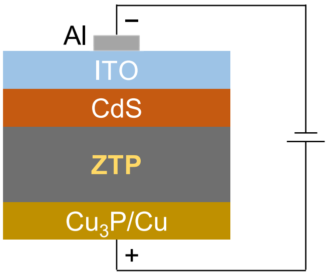

Figure 2-13. Schematic illustration of the direction of the bias applied on the ZTP-based solar cell in the EQE measurement.

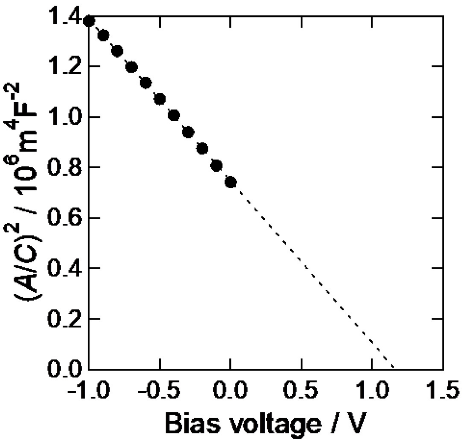

Figure 2-14. Mott-Schottky plot of solar cell with Cu3P insertion. The dotted line represents linear regression to measured values.

2.4. Summary of this chapter

We investigated the reactive diffusion at the interface between the Cu back electrode and ZTP absorber and found that the epitaxial formation of Cu_3P on ZTP through annealing at 400 °C. The electron diffraction analyses revealed the relationship of Cu_3P [1100](0001) // ZTP [110](112) and the lattice-mismatch was calculated less than 0.5 % from the phosphorus sublattice in both compounds. On the other hand, the work function of Cu_3P, which showed metallic conductivity, was close to the ionization potential of ZTP, which indicates the potential barrier against hole transport is small enough at the Cu_3P/ZTP interface. The resistance was really reduced by the formation of Cu_3P, while longer annealing made the resistance increase. This might be the reduction of electrode area due to Cu aggregation through interdiffusion. However, by intentionally preparing the Cu_3P layer between Cu and ZTP, the lowest resistance could be obtained even by short annealing for 5 min. The thickness of the reacted region was larger compared to 15 min-annealed specimens without Cu_3P insertion. This indicates that Cu_3P rather worked as a diffusion promoter, which was unexpected. Consequently, the knowledge obtained in the reactive diffusion experiments was applied to solar cell devices, and *J-V* characteristics of solar cells with intentional insertion of Cu_3P were close to desirable diode curves without cross-over. Such improvement of back contact led to good reproducibility, and the best efficiency of 3.87 % has been achieved. This work demonstrated that the insertion of a *back buffer* layer like Cu_3P, which was well-matched with absorber in the viewpoints of atom configuration and band alignment, is effective to realize Ohmic back contact with low resistance, leading to enhance the cell performance.

References to Chapter 2

[1] Alta Devices, “Alta Devices sets 29.1% solar efficiency record; NASA selects Alta Devices for International Space Station Test,” https://www.businesswire.com/news/home/20181212005060/en/Alta-Devices-Sets-29.1-Solar-Efficiency-Record 2018 (access; 24 December 2021).

[2] First Solar, “First Solar Hits Record 22.1% Conversion Efficiency for CdTe Solar Cell,” https://www.greentechmedia.com/articles/read/First-Solar-Hits-Record-22.1-Conversion-Efficiency-For-CdTe-Solar-Cell, 2016 (accessed 24 December 2021).

[3] Solar Frontier, Solar Frontier Achieves World Record Thin-Film Solar Cell Efficiency of 23.35%, http://www.solar-frontier.com/eng/news/2019/0117_press.html, 2019 (accessed 24 December 2021).

[4] W. Wang, M. T. Winkler, O. Gunawan, T. Gokmen, T. K. Todorov, Y. Zhu, D. B. Mitzi, “Device Characteristics of CZTSSe Thin-Film Solar Cells with 12.6% Efficiency,” *Adv. Energy Mater.* **4**, 1301465 (2014).

[5] T.K. Todorov, S. Singh, D.M. Bishop, O. Gunawan, Y.S. Lee, T.S. Gershon, K.W. Brew, P.D. Antunez, R. Haight, “Ultrathin high band gap solar cells with improved efficiencies from the world’s oldest photovoltaic material,” *Nat. Commun.* **8**, 682 (2017).

[6] A. Kanai, K. Toyonaga, K. Chino, H. Katagiri, H. Akari, “Fabrication of Cu_2SnS_3 thin-film solar cells with power conversion efficiency of over 4%,” *Jpn. J. Appl. Phys.* **54**, 08KC06 (2015).

[7] A.W. Welch, L.L. Baranowski, H. Peng, H. Hempel, R. Eichberger, T. Unold, S. Lany, C. Wolden, A. Zakutayev, “Trade-Offs in Thin Film Solar Cells with Layered Chalcostibite Photovoltaic Absorbers,” *Adv. Energy Mater.* **7**, 1601935 (2017).

[8] T. Minami, Y. Nishi, T. Miyata, “Efficiency enhancement using a $Zn_{1-x}Ge_x$-O thin film as an n-type window layer in Cu_2O-based heterojunction solar cells,” *Appl. Phys. Express* **9**, 052301 (2016).

[9] H-S. Yun, B-W. Park, Y.C. Choi, J. Im, T.J. Shin, S.I. Seok, “Efficient Nanostructured TiO_2/SnS

Heterojunction Solar Cells," *Adv. Energy Mater.* **9**, 1901343 (2019).

[10] A. Ennaoui, S. Fiechter, Ch. Pettenkofer, N. Alonso-Vante, K. Büker, M. Bronold, Ch. Höpfner, H. Tributsch, "Iron disulfide for solar energy conversion," *Sol. Energy Mater. Sol. Cells* **29**, 289–370 (1993).

[11] Z. Li, X. Liang, G. Li, H. Liu, H. Zhang, J. Guo, J. Chen, K. Shen, X. San, W. Yu, R.E.I. Schropp, Y. Mai, "9.2%-efficient core-shell structured antimony selenide nanorod array solar cells," *Nat. Commun.* **10**, 125 (2019).

[12] G.M. Kimball, N.S. Lewis, H.A. Atwater, "Mg doping and alloying in Zn_3P_2 heterojunction solar cells," *in 35th IEEE Photovoltaic Specialists Conference (PVSC-35)*, 1039–1043 (2010).

[13] K. Javaid, W. Wu, J. Wang, J. Fang, H. Zhang, J. Gao, F. Zhuge, L. Liang, H. Cao, "Band Offset Engineering in $ZnSnN_2$-Based Heterojunction for Low-Cost Solar Cells," *ACS Photonics* **5**, 2094–2099 (2018).

[14] L.H. Wong, A. Zakutayev, J.D. Major, X. Hao, A. Walsh, T.K. Todorov, E. Saucedo, "Emerging inorganic solar cell efficiency tables (Version 1)," *J. Phys.: Energy* **1**, 032001 (2019).

[15] T. Yokoyama, F. Oba, A. Seko, H. Hayashi, Y. Nose, I. Tanaka, "Theoretical Photovoltaic Conversion Efficiencies of $ZnSnP_2$, $CdSnP_2$, and $Zn_{1-x}Cd_xSnP_2$ Alloys," *Appl. Phys. Express* **6**, 061201 (2013).

[16] D.O. Scanlon, A. Walsh, "Bandgap engineering of $ZnSnP_2$ for high-efficiency solar cells," *Appl. Phys. Lett.* **100**, 251911 (2012).

[17] S. Nakatsuka, Y. Nose, "Order–Disorder Phenomena and Their Effects on Bandgap in $ZnSnP_2$," *J. Phys. Chem. C* **121**, 1040–1046 (2017).

[18] S. Nakatsuka, Y. Nose, T. Uda, "Fabrication of $ZnSnP_2$ thin films by phosphidation," *Thin Solid Films* **589**, 66–71 (2015).

[19] S. Nakatsuka, H. Nakamoto, Y. Nose, T. Uda, Y. Shirai, "Bulk crystal growth and

characterization of $ZnSnP_2$ compound semiconductor by flux method," *Phys. Status Solidi C* **12**, 520–523 (2015).

[20] S. Nakatsuka, N. Yuzawa, J. Chantana, T. Minemoto, Y. Nose, "Solar cells using bulk crystals of rare metal-free compound semiconductor $ZnSnP_2$," *Phys. Status Solidi A* **214**, 1600650 (2017).

[21] S. Akari, J. Ctantana, S. Nakatsuka, Y. Nose, T. Minemoto, "$ZnSnP_2$ solar cell with (Cd,Zn)S buffer layer: Analysis of recombination rates," *Sol. Energy Mater. Sol. Cells* **174**, 412–417 (2018).

[22] S. Nakatsuka, S. Akari, J. Chantana, T. Minemoto, Y. Nose, "Impact of Heterointerfaces in Solar Cells Using $ZnSnP_2$ Bulk Crystals," *ACS Appl. Mater. Interfaces* **9**, 33827–33832 (2017).

[23] T. Kuwano, S. Nakatsuka, Y. Nose, "Impact of structure on carrier transport behavior at the interface between electrode and $ZnSnP_2$ absorber," *IEEE 7th World Conference on Photovoltaic Energy Conversion (WCPEC-7)*, 2998–2999 (2018).

[24] O. Olofsson, "The Crystal Structure of Cu_3P," *Acta Chem. Scand.* **26**, 2777–2787 (1972).

[25] M. Rubenstein, R.W. Ure Jr., "Preparation and Characteristics of $ZnSnP_2$," *J. Phys. Chem. Solids* **29**, 551–555 (1968).

[26] D.S. Robertson, G. Snowball, H. Webber, "The preparation and properties of single crystal copper phosphide," *J. Mater. Sci.* **15**, 256–258 (1980).

[27] A. Wolff, T. Doert, J. Hunger, M. Kaiser, J. Pallmann, R. Reinhold, S. Yogendra, L. Giebeler, J. Sichelschemidt, W. Schnelle, R. Whiteside, H.Q.N. Gunaratne, P. Nockemann, J. Weigand, E. Brunner, M. Ruck, "Low-Temperature Tailoring of Copper-Deficient $Cu_{3-x}P$—Electric Properties, Phase Transitions, and Performance in Lithium-Ion Batteries," *Chem. Mater.* **30**, 7111–7123 (2018).

[28] G. Manna, R. Bose, N. Pradhan, "Semiconducting and Plasmonic Copper Phosphide Platelets," *Angew. Chem.* **125**, 6894–6898 (2013).

[29] S. Nakatsuka, Y. Nose, Y. Shirai, "Band offset at the heterojunction interfaces of $CdS/ZnSnP_2$, $ZnS/ZnSnP_2$, and $In_2S_3/ZnSnP_2$," *J. Appl. Phys.* **119**, 193107 (2016).

[30] T. Kuwano, R. Katsube, Y. Nose, "Improvement of Ohmic Behavior of Back Contact in $ZnSnP_2$ Solar Cells by Inserting Cu_3P," *IEEE 46th Photovoltaic Scientists Conference (PVSC-46)*, 3007-3009 (2019).

[31] A. Niemegeers, M. Burgelman, "Effects of the Au/CdTe back contact on IV and CV characteristics of Au/CdTe/CdS/TCO solar cells," *J. Appl. Phys.* **81**, 2881–2886 (1997).

[32] X. Wu, J. Zhou, A. Duda, Y. Yan, G. Teeter, S. Asher, W.K. Metzger, S. Demtsu, S.-H. Wei, R. Noufi, "Phase control of Cu_xTe film and its effects on CdS/CdTe solar cell," *Thin Solid Films* **515**, 5798–5803 (2007).

[33] S. Nishiwaki, N. Kohara, T. Negami, T. Wada, "$MoSe_2$ layer formation at $Cu(In,Ga)Se_2$/Mo Interfaces in High Efficiency $Cu(In_{1-x}Ga_x)Se_2$ Solar Cells," *Jpn. J. Appl. Phys.* **37**, L71–L73 (1998).

[34] S.M. Sze, K.K. Ng, "Physics of Semiconductor Devices (3rd ed.)," Wiley-Interscience, Chapter2 (2007).

[35] P.A. Fernandes, P.M.P. Salomé, A.F. Sartori, J. Malaquias, A.F. da Cunha, B.-A. Schubert, J.C. González, G.M. Ribeiro, "Effects of sulphurization time on Cu_2ZnSnS_4 absorbers and thin films solar cells obtained from metallic precursors," *Sol. Energy Mater. Sol. Cells* **115**, 157-165 (2013).

[36] Y. Kumagai, M. Choi, Y. Nose, F. Oba, "First-principles study of point defects in chalcopyrite $ZnSnP_2$," *Phys. Rev. B* **90**, 125202 (2014).

3. DLTS and PL analyses on $ZnSnP_2$ bulk crystals

3.1. Introduction

$ZnSnP_2$ (ZTP) has recently attracted much attention as a photo-absorber of thin-film solar cells because of the non-toxic constituents, the suitable bandgap (1.67 eV), and the high absorption coefficient of about 10^5 cm^{-1} in the visible light region [1,2]. Nakatsuka et al. first demonstrated solar cells using ZTP bulk crystals with the device structure of Al-doped ZnO/CdS/ZTP/Mo, referring to the typical structure of $CuInSe_2$-based solar cells, and reported the conversion efficiency of 0.087% [3]. They also discussed the high series resistance of 100 Ω cm^2 in the above device and proposed the usage of Cu as a back electrode in order to reduce the resistance in the subsequent work [4]. Based on their results, we recently revealed the formation of intermediate compound Cu_3P, which is well-matched to ZTP in the viewpoints of band and lattice structures, between ZTP and Cu electrode by heat treatment. Moreover, we have achieved 1.5 Ω cm^2, comparable to the resistance of the absorber ZTP, through the electrode structure with Cu_3P sputtered in advance, and consequently demonstrated the efficiency of 3.87% in ZTP solar cells [5,6]. On the other hand, there is still room for an efficiency improvement much, in particular, a short lifetime of minority carriers in ZTP bulk crystals reported by Nakatsuka et al. [3]. The short circuit current density (J_{SC}) and open-circuit voltage (V_{OC}) in the device with the best efficiency are 12.1 mA cm^{-2} and 0.535 V, respectively, and such low performance may come from poor carrier lifetime. The external quantum efficiency (EQE) spectra in ZTP also showed a strong bias dependence in the longer wavelength region, and which indicated an insufficient carrier collection through light absorption in this wavelength region, in other words, a short diffusion length of minority carriers.

In this study, ZTP bulk crystals were characterized by deep level transient spectroscopy (DLTS) and photoluminescence (PL) for discussion on intrinsic defects to improve carrier lifetime. DLTS is well known to be a technique to detect trap levels in semiconductors and has also been applied to devices recently. Das et al. demonstrated the existence of deep acceptor levels detected by DLTS in $Cu_2ZnSn(S_xSe_{1-x})_4$ (CZTSSe) solar cells directly affects the performance of solar cells [7]. A further discussion including first-principles calculation on intrinsic point defects such as formation energies and energy levels is fruitful for conventional materials of thin-film solar cells [8] and even for emerging absorber materials such as SnS [9], Cu_3N [10], FeS_2 [11], and Cu_2SnS_3 [12]. Particularly, a combination of experiments and theory based on defect physics is developing [13], and actually, it was clearly shown that emission observed in a PL spectrum consisted of some recombination processes related to shallow and deep levels in an absorber material $CuSbS_2$ [14]. The aim of this study is thus to reveal the recombination behavior of minority carriers based on energy levels due to intrinsic defects in ZTP through electric and optical evaluations and theoretical calculation. Note that Kumagai et al. reported first-principles calculation for intrinsic point defects in ZTP and evaluated formation energy and energy level of each defect [15]. In this study, we discuss experimental results by DLTS, PL, and our previous results on time-resolved PL (TRPL) based on their calculation.

3.2. Experimental procedures

ZTP bulk crystals were grown by a solution method using Sn flux as reported by Nakatsuka et al. [16]. The obtained bulk crystals were cut into wafers with a thickness of ~0.8 mm, and both surfaces of each wafer were mechanically polished and chemically treated using 1/2-diluted aqua regia, 1/4-diluted hydrochloric acid, and ultrapure water in this order. For DLTS measurements, we prepared specimens with the structure of Ag/ZTP/Cu_3P/Cu, where Ag and Cu were adopted as a Schottky and ohmic contact, respectively [4,5]. Cu_3P thin layer with 25 nm in thickness was prepared on a treated surface by DC sputtering, and then Cu film was also deposited by DC sputtering in the same chamber. After deposition of Cu_3P and Cu, the specimens were annealed at 673 K for 5 min in an evacuated quartz ampule to reduce the resistance. Subsequently, an Ag electrode was prepared on the opposite surface of the wafer by conventional thermal evaporation. According to a typical DLTS procedure proposed by Lang [16], the transient capacitances between a certain time, t_1 and t_2, with various rate windows, expressed by ΔC, were evaluated as a function of temperature for Ag/ZTP/Cu_3P/Cu diodes. The reverse and pulse biases were set at −1.3 and 1.3 V for condition 1, and −1.7 and 1.7 V for condition 2, respectively. The pulse width was 1 ms for both conditions. The temperature was swept from 300 to 80 K. PL measurements were performed at room temperature using a He-Cd laser with the wavelength of 442 nm and the power of 10 mW.

3.3. Results and discussion

Figure 3-1 shows DLTS signals for the Ag/ZTP/Cu_3P/Cu specimen measured under the conditions 1 and 2. A series of negative signals were observed in condition 1, as seen Fig. 3-1(a), while each spectrum in Fig. 3-1(b) for condition 2 includes negative and positive signals. Since ZTP exhibits a *p*-type conductivity [17], Fig. 3-1 indicates two acceptor-like (hole) traps, A1 and A2, and one donor-like (electron) trap, D1, in ZTP bulk crystal. According to conventional analysis for DLTS [16,18], the activation energy of trap i, E_i, is estimated using the following relation,

$$\tau T^2 \propto \exp\left(E_i / kT\right), \qquad (3\text{-}1)$$

where T is the absolute temperature at which ΔC takes a maximal or minimal value, k is the Boltzmann constant, and τ is the time constant defined as

$$\tau = \frac{t_2 - t_1}{\ln(t_2 / t_1)}. \qquad (3\text{-}2)$$

In this study, the ratio, t_2/t_1, was fixed at 11.5, hence τ equals to $4.3t_1$. Fig. 3-2 shows an Arrhenius plot derived from DLTS. The activation energies for traps A1, A2, and D1 were estimated to be 0.12±0.01, 0.65±0.13, and 0.21±0.02 eV, respectively. The estimated energies for donor- and acceptor-like traps correspond to gaps with the conduction band minimum (CBM) edge, E_c, or the valence band maximum (VBM) edge, E_v. A Diagram of relative energy levels for E_c, E_v, and traps is thus shown in Fig. 3-3. We first discuss the carrier recombination including shallow levels based on the diagram. Figure 4 shows the PL spectrum of a ZTP wafer measured at room temperature. In Fig. 3-4, a sharp emission coming from band-to-band transition is observed around 1.69 eV, of which the peak position is comparable to that reported on a ZTP bulk crystal by Nakatsuka et al. [3], while emission with the small and broad signal is confirmed in the lower energy range. Considering the diagram shown in Fig. 3-3, there are three transition processes in addition to band-to-band recombination in the energy range of PL measurements. We thus analyzed the PL spectrum using Voigt function assuming four transitions: D1 to A1 (DAP), D1 to VBM, CBM to A1, and band-to-band. The results are also shown as blue-dashed and green-solid lines in Fig. 3-4. Peak positions derived from four Voigt functions were 1.29, 1.41, 1.59, and 1.69 eV. The energies for four possible recombination processes in the diagram shown in Fig. 3-3 are 1.36 (E_{D1}–E_{A1}), 1.48 (E_{D1}–E_{V}), 1.57 (E_{C}–E_{A1}), and 1.69 eV (E_{C}–E_{V}), which correspond to the energies for respective transitions observed in PL spectrum. Therefore, the results of PL and DLTS coincide with each other. According to the calculation by Kumagai et al. [15], formation energies are significantly low for antisites of Zn on Sn site ($\mathrm{Zn_{Sn}}$) and Sn on Zn site ($\mathrm{Sn_{Zn}}$), suggesting that they are dominant defects in ZTP. Thermodynamic transition level, TTL, of $\mathrm{Sn_{Zn}}$ (+2/0) is 0.2 eV below CBM edge, which means antisite of Sn can act as a donor-like defect. On the other hand, antisite of Zn might act as acceptor and lead to *p*-type conductivity of ZTP, although TTL of $\mathrm{Zn_{Sn}}$ (0/−2) was not clearly confirmed between CBM and VBM in the calculation. It is stated that the formation energy of $\mathrm{Zn_{Sn}}^0$ was overestimated in their calculation resulting in lower TTL of $\mathrm{Zn_{Sn}}$. The temperature dependence of hole concentration in ZTP is shown in Figure 3-5, and the activation energy in *p*-type ZTP is evaluated to be 0.105 eV, which is supported the formation of $\mathrm{Zn_{Sn}}$ as an acceptor defect.

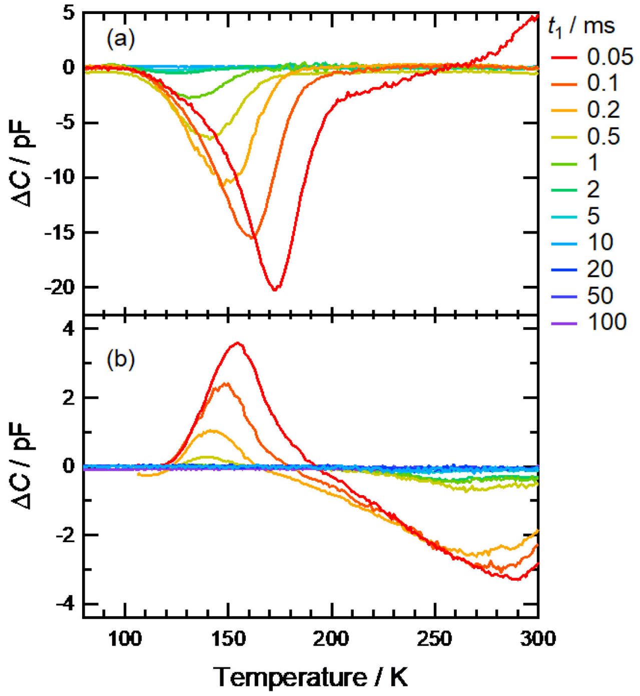

Figure 3-1. DLTS spectra of Ag/ZTP/Cu$_3$P/Cu specimen with various t_1. Reverse bias and pulse bias are (a) −1.3 and 1.3 V and (b) −1.7 and 1.7 V, respectively.

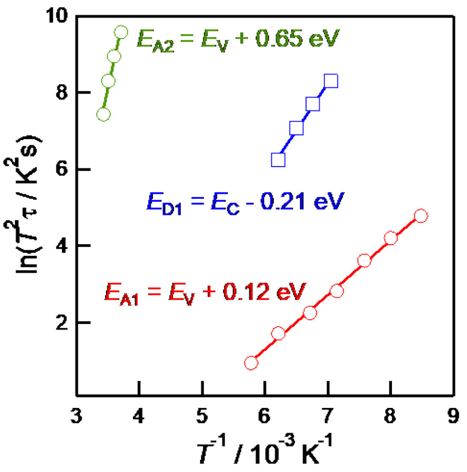

Figure 3-2. Arrhenius plots from DLTS spectra of Ag/ZTP/Cu$_3$P/Cu specimen shown in Fig. 3-1.

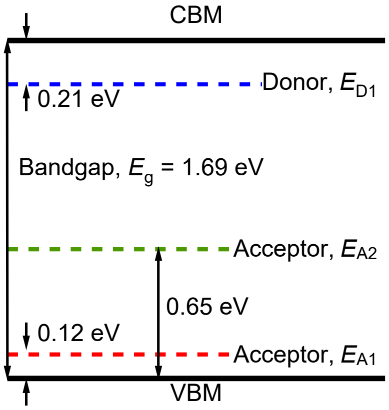

Figure 3-3. Relatively shallow trap levels detected by DLTS shown with respect to CBM and VBM. The bandgap is determined by PL analysis.

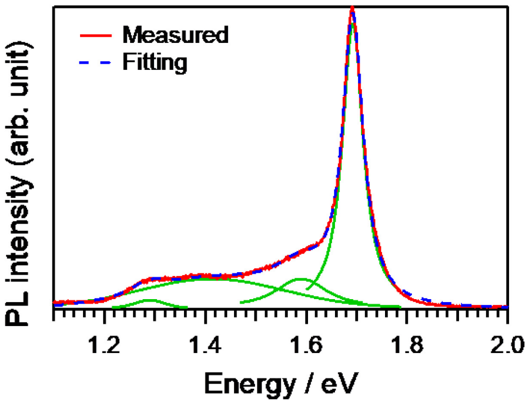

Figure 3-4. Room-temperature PL spectrum of a ZTP bulk crystal.

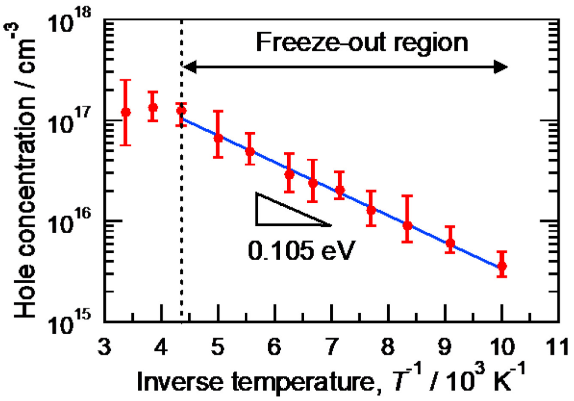

Figure 3-5. Temperature dependence of hole concentration in $ZnSnP_2$ crystal. The activation energy is approximately 0.105 eV.

TTLs can be experimentally obtained from DLTS or temperature-dependent Hall effect measurements [19]. In DLTS, TTLs are evaluated from activation energies since it corresponds to thermal ionization energies [20]. Consequently, shallow traps of D1 and A1 come from antisite defects of $\mathrm{Sn_{Zn}}$ and $\mathrm{Zn_{Sn}}$, respectively. We also discuss A2, the trap with a deep level in the diagram shown in Fig. 3. In the viewpoint of TTL, similarly to the discussion for traps D1 and A1, vacancies of phosphorus and tin, and interstitial defects of zinc and phosphorus should be considered for A2. Among them, the vacancy of phosphorus ($\mathrm{V_P}$) and interstitial zinc (Zn_i) are rather favorable from their formation energies. First-principles calculation actually suggested that they might show acceptor-like behavior.

Here, we re-discuss a decay curve of TRPL in ZTP bulk crystal reported in our previous work [3]. They analyzed the curve using two components and evaluated minority carrier lifetime to be 0.442 and 37.8 ns. On the other hand, the ratio of the pre-exponential factors of the fast component to slow one was about 10^2, which implies that almost all minority carriers with light-excited vanished due to fast recombination other than band-to-band. This experimental fact is consistent with the present results showing the presence of A2, the trap with deep energy level, based on the Shockley-Read-Hall theory [21,22].

3.4. Summary of this chapter

In summary, we investigated hole and electron traps in ZTP bulk crystals by DLTS and PL. DLTS analysis revealed three types of traps in ZTP bulk crystal: two with shallow energy levels and the other with a deep level. Hole and electron traps with shallow levels are related to carrier concentration at room temperature, corresponding to so-called donor and acceptor defects, respectively. The previous study based on ab-initio calculation also suggested antisite Sn and Zn might correspond to such defects, respectively, which are favorable in the viewpoint of the formation energy. In the PL spectrum, the sub-gap luminescence in a broad energy range was observed, and it was understood the spectrum contained four recombinations related to CBM, VBM, and the above acceptor and donor levels. On the other hand, the trap with a deep energy level might come from phosphorus vacancy or Zn interstitials, and the presence of such a trap is also suggested in the TRPL decay of our previous work. The formation energy of such defects by calculation is relatively high in ZTP, and it is an advantage as an absorber in solar cells. However, the discussion on DLTS is slightly inconsistent with theoretical studies. This might be from the chemical environment, in other words, chemical potentials of constituent elements, in preparation of bulk crystals, which should be considered and investigated in future works.

References to Chapter 3

[1] J. L. Shay, J.H. Wernick, "Ternary chalcopyrite semiconductors, growth, electronic properties, and applications," Pergamon Press, Oxford, (1975).

[2] T. Yokoyama, F. Oba, A. Seko, H. Hayashi, Y. Nose, I. Tanaka, "Theoretical Photovoltaic Conversion Efficiencies of $ZnSnP_2$, $CdSnP_2$, and $Zn_{1-x}Cd_xSnP_2$ Alloys," *Appl. Phys. Express* **6**, 061201 (2013).

[3] S. Nakatsuka, N. Yuzawa, J. Chantana, T. Minemoto, Y. Nose, "Solar cells using bulk crystals of rare metal-free compound semiconductor $ZnSnP_2$," *Phys. Status Solidi A* **214**, 1600650 (2017).

[4] S. Nakatsuka, S. Akari, J. Chantana, T. Minemoto, Y. Nose, "Impact of Heterointerfaces in Solar Cells Using $ZnSnP_2$ Bulk Crystals," *ACS Appl. Mater. Interfaces* **9**, 33827 (2017).

[5] T. Kuwano, R. Katsube, Y. Nose, "Improvement of Ohmic Behavior of Back Contact in $ZnSnP_2$ Solar Cells by Inserting Cu_3P,"in *IEEE 46th Photovoltaic Specialists Conference (PVSC)*, 3007 (2019).

[6] T. Kuwano, R. Katsube, K. Kazumi, Y. Nose, "Performance enhancement of $ZnSnP_2$ solar cells by a Cu_3P back buffer layer," *Sol. Energy Mater. Sol. Cells* **221**, 110891 (2021).

[7] S.Das, S.K.Chaudhuri, R.N. Bhattacharya, K.C. Mandal, "Defect levels in $Cu_2ZnSn(S_xSe_{1-x})_4$ solar cells probed by current-mode deep level transient spectroscopy," *Appl. Phys. Lett.* **104**, 192106 (2014).

[8] J.S. Park, S. Kim, Z. Xie, A. Walsh, "Point defect engineering in thin-film solar cells," *Nat. Rev. Mater.* **3**, 194 (2018).

[9] J. Vidal, S. Lany, M. d'Avezac, A. Zunger, A. Zakutayev, J. Francis, J. Tate, "Band-structure, optical properties, and defect physics of the photovoltaic semiconductor SnS," *Appl. Phys. Lett.* **100**, 032104 (2012).

[10] A. Zakutayev, C.M. Caskey, A.N. Fioretti, D.S. Ginley, J. Vidal, V. Stevanovic, E. Tea, S. Lany, "Defect Tolerant Semiconductors for Solar Energy Conversion," *J. Phys. Chem. Lett.* **5**, 1117 (2014).

[11] L. Yu, S. Lany, R. Kykyneshi, V. Jieratum, R. Ravichandran, B. Pelatt, E. Altschul, H.A.S. Platt,

J.F. Wager, D.A. Keszler, A. Zunger, “Iron Chalcogenide Photovoltaic Absorbers,” *Adv. Energy Mater.* **1**, 748 (2011).

[12] P.W. Guan Z.K. Liu, “A hybrid functional study of native point defects in Cu_2SnS_3: implications for reducing carrier recombination,” *Phys. Chem. Chem. Phys.* **20**, 256 (2018).

[13] A. Alkauskas. M.D. McCluskey, C.G. Van de Walle, “Tutorial: Defects in semiconductors—Combining experiment and theory,” *J. Appl. Phys.* **119**, 181101 (2016).

[14] F.W. de Souza Lucas, H. Peng, S. Johnston, P.C. Dippo, S. Lany, L.H. Mascaro, A. Zakutayev, “Characterization of defects in copper antimony disulfide,” *J. Mater. Chem.* A **5**, 21986 (2017).

[15] Y. Kumagai, M. Choi, Y. Nose, F. Oba, “First-principles study of point defects in chalcopyrite $ZnSnP_2$,” *Phys. Rev. B* **90**, 125202 (2014).

[16] D. V. Lang, “Deep-level transient spectroscopy: A new method to characterize traps in semiconductors,” *J. Appl. Phys.* **45**, 3023 (1974).

[17] S. Nakatsuka, H. Nakamoto, Y. Nose, T. Uda, Y. Shirai, “Bulk crystal growth and characterization of $ZnSnP_2$ compound semiconductor by flux method,” *Phys. Status Solidi C* **12**, 520 (2015).

[18] D.K. Schroder, “Semiconductor Material and Device Characterization,” 3rd ed. (John Wiley & Sons, Inc., New Jersey, 2015), pp. 270–274.

[19] C. Freysoldt, B. Grabowski, T. Hickel, J. Neugebauer, G. Kresse, A. Janotti, C.G. Van de Walle, “First-principles calculations for point defects in solids,” *Rev. Mod. Phys.* **86**, 253 (2014).

[20] D. Wickramarantne, C.E. Dreyer, B. Monserrat, J.X. Shen, J.L. Lyons, A. Alkauskas, C.G. Van de Walle, “Defect identification based on first-principles calculations for deep level transient spectroscopy,” *Appl. Phys. Lett.* **113**, 192106 (2018).

[21] W. Shockley, W.T. Read, “Statistics of the Recombinations of Holes and Electrons,” *Phys. Rev.* **87**, 835 (1952).

[22] R.N. Hall, “Electron-Hole Recombination in Germanium,” *Phys. Rev.* **87**, 387 (1952).

4. Raman spectroscopy on $ZnSnP_2$ with various degrees of order

4.1. Experimental procedures

4.1.1. Bulk crystal growth

$ZnSnP_2$ bulk crystals with various degrees of order were prepared according to our previous report [1]. Starting materials, zinc shots (99.9999% purity, Kojundo Chemical Laboratory), tin shots (99.99% purity, Kojundo Chemical Laboratory), and red phosphorus flakes (99.9999% purity, Kojundo Chemical Laboratory), were sealed in evacuated quartz ampules with inner diameters of 11 mm under a pressure of 10^{-2} Pa. The overall weight of the materials was about 60 g, and the nominal molar composition was 92 mol%Sn, 2.7 mol%Zn and 5.3 mol%P. The ampules were then heated up to 700 °C and kept for 12 hours for homogenization. After homogenization, the ampules were unidirectionally cooled from the bottom at different rates of 0.7−640 °C h^{-1} to obtain specimens with various degrees of order in the cation sub-lattice. For a specimen with a cooling rate of 0.7 °C h^{-1}, bulk crystals precipitating at the bottom of the ingot were then cut into wafers with a thickness of about 1 mm using a diamond wheel saw. Some wafers were then mechanically polished with emery papers and a buff-sheet, and the others were ground into powder with an agate mortar and a pestle for following characterizations. For the specimens with other cooling rates in which small $ZnSnP_2$ dispersed around in ingots, Sn flux was dissolved by NaCl-added nitric acid. NaCl was added as a supplier of chlorine ions for the formation of tin chloride complex. After completely dissolving Sn flux, the solvent was filtered and $ZnSnP_2$ flakes were collected. Those flakes were ground into powder as done for wafers, with remaining some of them as collected for following measurements.

4.1.2. Characterizations

X-ray diffraction (XRD) were measured for all types of samples, such as wafer, flake, and powder, by the equipment (X'Pert Pro Alpha-1, PANalytical) and conditions; using CuKα_1 ($\lambda = 1.5406$

Å) with the tube voltage and current of 45 kV and 40 mA, respectively, in the Bragg-Brentano (θ-2θ) configuration. Raman spectra were measured with laser Raman spectrometer (NRS-3100 for powder and NRS-5500 for wafers and flakes, JASCO). The laser diameter of ~1 μm and resolution of ~1 cm^{-1} in wavenumber. The laser wavelength was 532 nm. Compositions of flakes were analyzed by scanning electron microscopy (SEM; JCM-600Plus, JEOL) equipped with energy-dispersive x-ray spectroscopy (EDS; MP-05030EDK, JEOL). In EDS analysis, we used a bulk crystal of $ZnSnP_2$ as a standard, supposing $ZnSnP_2$ is a line compound. Optical properties were analyzed based on transmittance and diffuse reflectance measurements (UV-2600, SHIMADZU) and ellipsometry (UVISEL, HORIBA). Chemical states were analyzed for all types of samples by x-ray photoelectron spectroscopy (XPS; ESCA-3400HSE, SHIMADZU) using Mg Kα with the acceleration voltage of 10 kV and emission current of 20 mA under pressure less than 10^{-6} Pa before and after etching surface. The surface etching was done by Ar gas with the pressure of 4×10^{-3} Pa, the acceleration voltage of 0.5 kV, and the emission current of 20 mA.

4.2. Results and discussion

Figure 4-1 shows XRD profiles of the powder specimens obtained by grinding wafer and flake obtained from ingots grown with the cooling rate of 0.7 and 640 ºC h^{-1}, respectively. The pictures of the wafer and flake are also shown. Both XRD profiles indicate the presence of only $ZnSnP_2$ while the intensity of the superlattice reflection is higher for the lower cooling rate than those for the higher one. A stronger superlattice reflection indicates a higher degree of order [1]. Thus, the degree of order in the wafer is higher than that in the flake. It has also been reported that a high degree of order resulted in a wider bandgap [1]. Figure 4-2 Transmittance spectra and Tauc plots for the wafer and flake $ZnSnP_2$. Tauc plots were calculated, supposing that the absorption edge of $ZnSnP_2$ is associated with a direct-

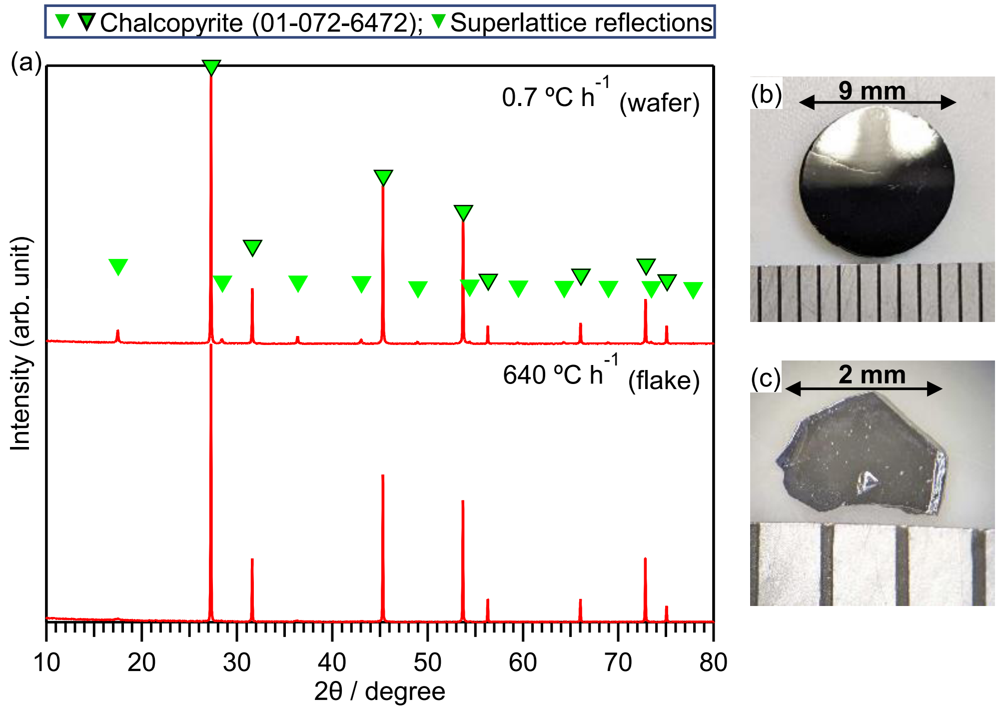

Figure 4-1. (a)XRD profiles of powder specimens with cooling rates of 0.7 and 640 ºC h^{-1}, respectively corresponding to (b) wafer and (c) flake.

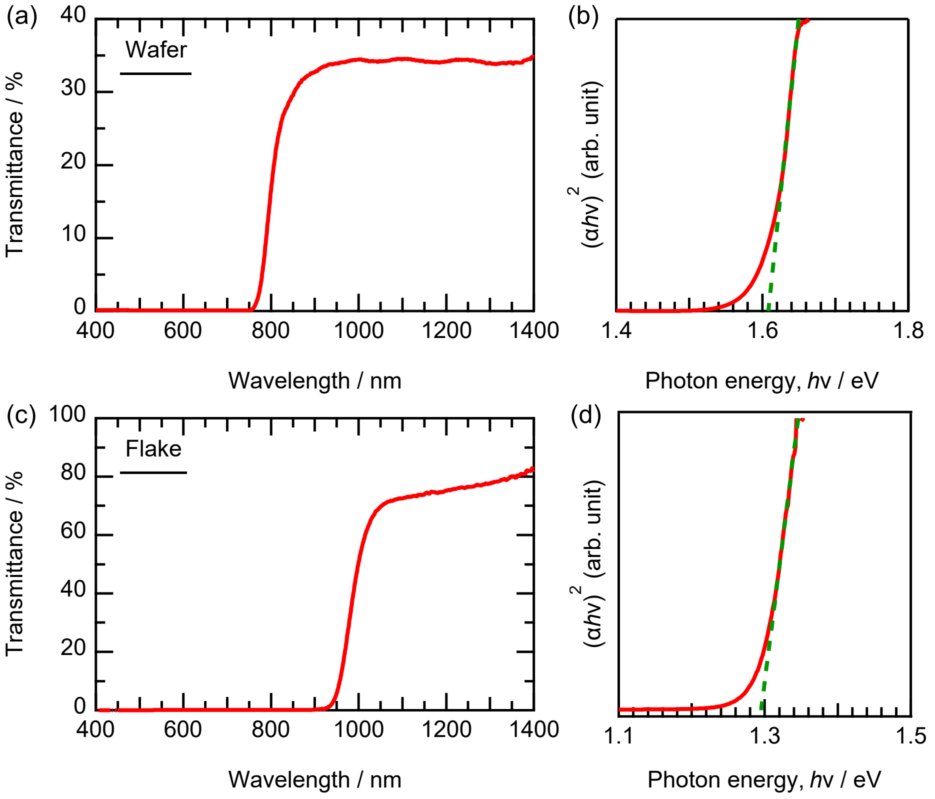

Figure 4-2. Diffuse reflectance and/or transmittance spectra of (a) wafer and (b) flake specimens, and the Tauc plot for (c) wafer and (b) flake specimens.

transition from the valence band maximum (VBM) to the conduction band minimum (CBM) at the Γ-point in **k**-space [2]. The optical bandgap of the wafer specimen is about 1.6 eV, while that of the flake one is about 1.3 eV, which reflects the degree of order.

Figure 4-3 shows Raman spectra and fitting curves for wafer, flake, and powder $ZnSnP_2$ with various cooling rates. As shown in Fig. 4-3 (a), fitting analysis for the wafer resulted in four sharp peaks with Raman shifts of 308.3, 327.9, 342.4, and 365.3 cm^{-1}. In this study, Gaussian seems more favorable for fitting analyses than Lorentzian, maybe due to the broadness of observed peaks. Compared to the values of Raman shifts reported by Mintayrov et al. [3], these peaks can be assigned to the vibration modes of chalcopyrite $ZnSnP_2$, Γ_1, Γ_{5T}, Γ_{5T}, and Γ_{4L}, respectively. The notations of vibration modes are referred to in the report by Mintairov et al. [3] and Kaminow et al. [4]. According to them, the vibration mode of Γ_1 is associated only with the displacement of P atoms, while Γ_{5T} and Γ_{4L} include those of Zn and Sn atoms as well. A study of nuclear magnetic resonance by Ryan et al. indicated that when cation-ordering occurs, the tetrahedral coordination around P-toms deviates from the most stable electrically state of the perfectly-ordered $ZnSnP_2$ [5]. Namely, the combination of the number of the first nearest Zn and Sn atoms around each P atom changed from 2 Zn and 2 Sn, for example, to 1 Zn and 3 Sn or vice versa. On the other hand, the tetrahedral coordination around each cation is invariant under cation-disordering: Zn and Sn atoms are surrounded by 4 P atoms. This implies that vibration modes associated with the displacement of P atoms may change sensitively with cation-disordering. Fig. 4-3(b) shows the Raman spectrum of the flake, for which five peaks are found by fitting analysis. Two peaks at 310.9 and 358.3 cm^{-1} are likely Γ_1 and Γ_{4L} modes, respectively, which are common peaks for the wafer. However, the relative intensity of Γ_1 is much lower for the flake than that of the wafer. As discussed above, Γ_1 is associated only with the displacement of P atoms, but Γ_{4L} includes those of Zn and Sn as well. The weakening of the Γ_1 mode may reflect the decrease of the degree of order. Such behavior of Γ_1 mode was observed in the polarized Raman spectra of thin-film

$ZnSnP_2$ epitaxially grown on GaAs substrate [3]. In contrast to Γ_1, Γ_{4L} seems less sensitive to the difference of the degree of order probably because Γ_{4L} includes the displacement of not only P but also Zn and Sn atoms. Camassel et al. [6] and Artus et al. [7] reported based on group theoretical analyses that Γ_{4L} is a zone-center Raman-active mode for both space groups T_d^2 and D_{2d}^{12}, indicating that Γ_{4L} appears for both perfectly-disordered and -ordered $ZnSnP_2$. On the other hand, two peaks at 295 and 333 cm^{-1} in the Raman spectra of the flake are not observed for the wafer. Considering the low degree of order of the flake, these peaks are rather assigned to Γ_2 mode, which is Raman-inactive in the perfectly-ordered $ZnSnP_2$ but allowed when the cation-disordering is remarkable [3]. The large FWHM for the flake specimen can also be explained by cation-disordering. In $ZnSnP_2$, a decrease in the degree of order directly corresponds to the increase of the concentration of cation antisites such as Zn on Sn site (Zn_{Sn}) and Sn on Zn site (Sn_{Zn}). Generally, an increase in defect concentration leads to

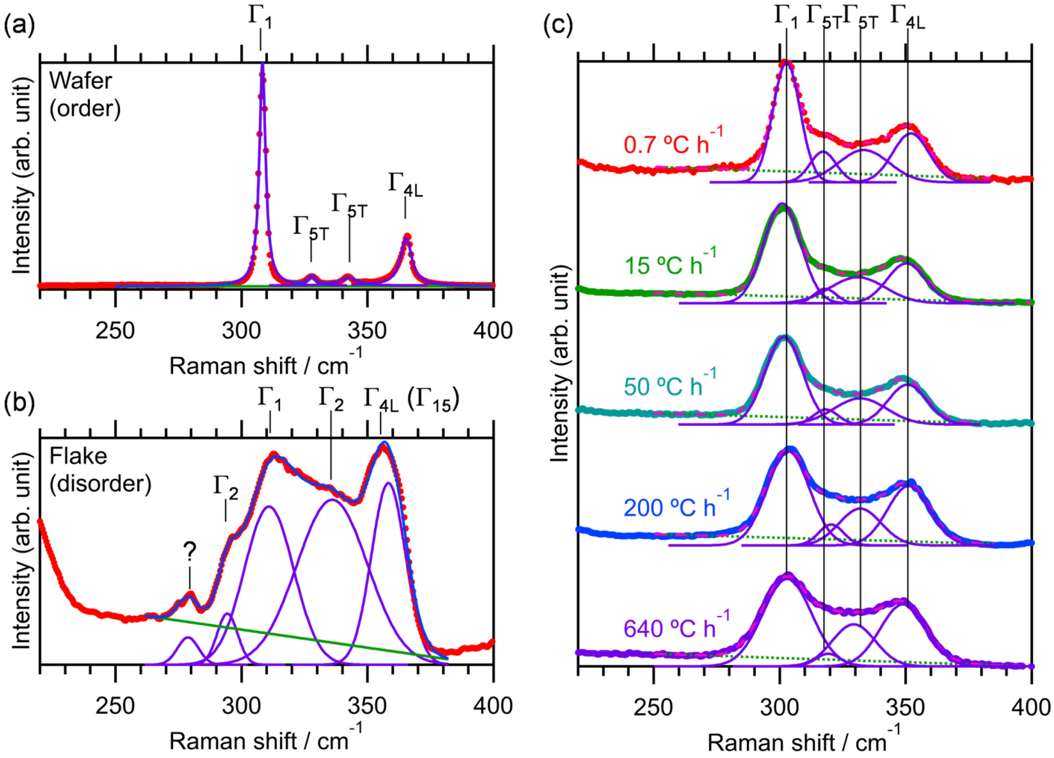

Figure 4-3. Raman spectra of various types of $ZnSnP_2$. (a) Wafer, (b) flake, and (c) powder grown with different cooling rates.

enhancement of damping effects and results in weakening and broadening of Raman peaks. Spatial correlation model by Parayanthal and Pollak also suggests that disorder-induced potential fluctuation leads to broadening of Raman line shape [8]. The small peak at 280 cm^{-1} could not be assigned to the reported vibration mode for $ZnSnP_2$.

Figure 4-3(c) shows Raman spectra of powder $ZnSnP_2$ with various degrees of order confirmed by Nakatsuka and Nose [1]. The peak FWHM is much larger than those of the wafer specimen mainly due to the scattering by much stress and defects induced during grinding. Fitting analyses found four peaks at 302.3±1.8, 318.6±2.2, 331.7±2.7, and 350.6±2.0 cm^{-1}. As is the case for the wafer, they can be assigned to Γ_1, Γ_{5T}, Γ_{5T}, and Γ_{4L} modes, respectively. Γ_1 mode in powder $ZnSnP_2$ exhibits a similar trend to those in wafer and flake: the peak intensity of Γ_1 seems to increase with the decrease in the cooling rate and hence increase in the degree of order.

For more quantitative discussion, the fitting parameters to Raman spectra of all types of specimens are summarized in Figure 4-4: FWHM of Γ_1 and Γ_{4L} (Γ_{15}) peaks and area- and height-ratio of Γ_1 to Γ_{4L} (Γ_{15}). Figure 4-4(a) shows the parameters for the wafer and flake specimens, corresponding

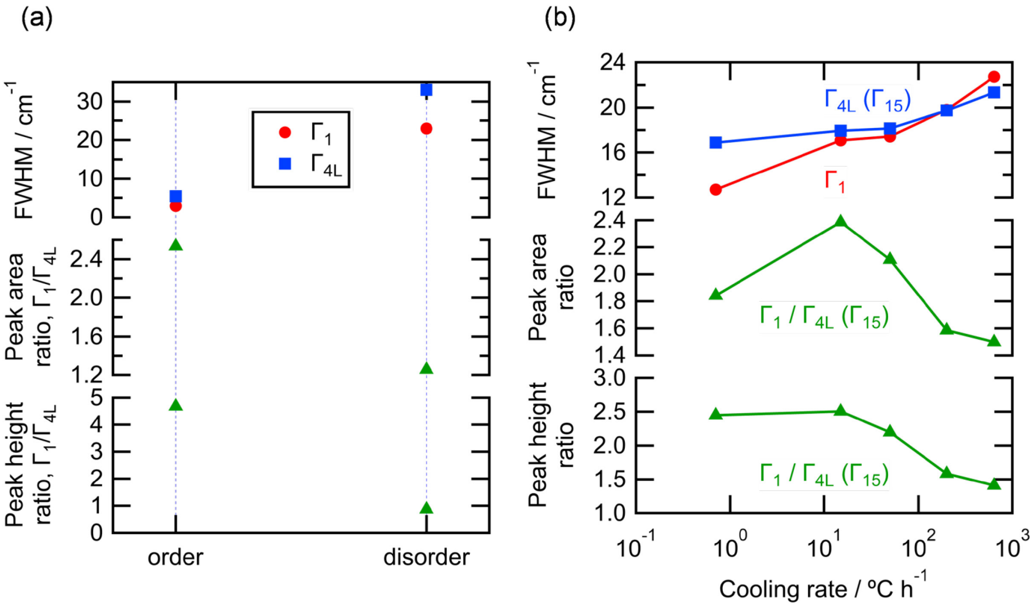

Figure 4-4. FWHM and normalized peak area and intensity evaluated by Gaussian fitting to Raman spectra of (a) bulk and (b) powder $ZnSnP_2$ grown with various cooling rates.

to high and low degrees of order, respectively. FWHM is smaller and area- and height-ratio is higher for the wafer than for the flake. Figure 4-4(b) shows the fitting parameters for powder specimens. As is the case for wafer and flake, FWHM of both Γ_1 and Γ_{4L} decrease with the decrease of cooling rate. The decrease in the FWHM may be explained by the reduction of the damping effect or potential fluctuation due to cation antisites. On the other hand, the peak area ratio does not change monotonically with the degree of order, which takes a maximum at 15 ºC h^{-1}. It can be considered that when the degree of order becomes higher than a certain value, a further reduction of the cation antisites makes the momentum conservation rule of Raman scattering stricter. In this case, phonons with non-zero momentum are not allowed to participate in the first-order Raman scattering process [9], which may cause a decrease in the total number of phonons involved and result in a decrease in the peak area. Generally, the peak area of the Gaussian function is proportional to the product of the FWHM and the peak height. Thus, the small change of the peak height ratio in the range of the cooling rate between 15 and 0.5 ºC h^{-1} results from the balance of the FWHM and the area ratio. These results partly suggest that Raman spectroscopy can be used to evaluate the degree of order of $ZnSnP_2$. However, it is also implied that a more comprehensive and quantitative model should be established, such as taking the grind-induced stress into account.

4.3. Summary of this chapter

In the present study, bulk and powder $ZnSnP_2$ with various degrees of order are characterized by non-polarized Raman spectroscopy. The ordered wafer exhibits a sharp and strong peak of the Γ_1 mode, while the disordered flake exhibits a weak and broad one, which is consistent with the report by Mintairov et al. Systematic changes of the peak intensity, area, and FWHM are also confirmed for the Γ_1 mode in powder samples with different long-range order parameters. These results partly suggest that Raman spectroscopy can be used to evaluate the degree of order of $ZnSnP_2$. However, it is also implied that a more comprehensive and quantitative model should be established, such as taking the grind-induced stress into account.

References to Chapter 4

[1] S. Nakatsuka, Y. Nose, “Order–Disorder Phenomena and Their Effects on Bandgap in $ZnSnP_2$,” *J. Phys. Chem. C* **121**, 1040 (2017).

[2] J. Tauc, “Optical Properties and Electronic Structure of Amorphous Ge and Si,” *Mater. Res. Bull.* **3**, 37 (1968).

[3] A.M. Mintairov, N.A. Sadchikov, T. Sauncy, M. Holtz, G.A. Seryogin, S.A. Nikishin, H. Temkin, “Vibrational Raman and Infrared Studies of Ordering in Epitaxial $ZnSnP_2$,” *Phys. Rev. B* **59**, 15197 (1999).

[4] I.P. Kaminow, E. Buehler, J.H. Wernick, “Vibrational Modes in $ZnSiP_2$,” *Phys. Rev. B* **2**, 960 (1970).

[5] M.A. Ryan, M.W. Peterson, D.L. Williamson, J.S. Frey, G.E. Maciel, B.A. Parkinson, “Metal Site Disorder in Zinc Tin Phosphide,” *J. Mater. Res.* **2**, 528 (1987).

[6] J. Camassel, L. Artus, J. Pascual, “Lattice Dynamics of $AgGaSe_2$. I. Experiment,” *Phys. Rev. B* **41**, 5717 (1990).

[7] L. Artus, J. Pujol, J. Pascual, J. Camassel, “Lattice Dynamics of $AgGaSe_2$. II. Theoretical Aspects,” *Phys. Rev. B* **41**, 5727 (1990).

[8] P. Parayanthal, F.H. Pollak, “Raman Scattering in Alloy Semiconductors: “Spatial Correlation” Model,” *Phys. Rev. Lett.* **52**, 1822 (1984).

[9] T.J. Peshek, T.R. Paudel, K. Kash, W.R.L. Lambrecht, “Vibrational Modes in $ZnGeN_2$: Raman Study and Theory,” *Phys. Rev. B* **77**, 235213 (2008).

5. MBE growth of thin-film $ZnSnP_2$

5.1. Experimental procedures

5.1.1. Thin-film growth

Thin-film $ZnSnP_2$ was grown by MBE using effusion cells. Zn and Sn vapors were supplied from pure metal sources, while P_4 vapor was from Sn_4P_3/Sn composites as reported before [1]. Beam equivalent pressures (BEP) of each vapor were measured by a beam flux monitor with a nude ion gage of an yttria coated iridium filament and a platinum-clad molybdenum wire gird (NIG-2TF 954-7903, Canon Anelva). BEPs of Zn, Sn, and P_4 vapors were set at about 8.5×10^{-6}, 1.5×10^{-5}, and 1.8×10^{-2} Pa, which are modified values from those used in the previous study [2]. All elements were co-supplied for a deposition period of 120 min in all depositions. Soda-lime glass substrates were used and the substrate temperature was measured by a pyrometer (KTL Pro, LEC). The accuracy of the pyrometer was confirmed by the fact that thin-film Sn was melted at the measured temperature of ~230 ºC, near the melting temperature of Sn (232 ºC). Here, the measured temperature by the pyrometer is called growth temperature, T_G. The employed growth temperatures were 200–320 ºC.

5.1.2. Characterizations

Grazing incidence x-ray diffraction (GI-XRD) was measured by standard equipment (Empyrean, Malvern PANalytical) using $CuK\alpha_1$ ($\lambda = 1.5406$ Å) as a source with the tube voltage and current of 45 kV and 40 mA, respectively. The incident angle ω was 0.5º. Raman spectra were measured with a laser Raman spectrometer (NRS-3100, JASCO). Magnification, exposure time, and laser power were the same for all films. The composition of films were analyzed by scanning electron microscopy (SEM; JCM-600Plus, JEOL) equipped with energy-dispersive x-ray spectroscopy (EDS; MP-05030EDK, JEOL). For EDS analysis, the wafer $ZnSnP_2$ was used as a standard with supposing the molar ratio, Zn:Sn:P, is 1:1:2. The thickness of the films was measured by a stylus profiler (Dektak

6M, Veeco). Optical properties were analyzed based on transmittance and diffuse reflectance measurements (UV-2600, SHIMADZU) and ellipsometry (UVISEL, HORIBA). Electrical properties of films were measured by the van der Pauw method with an AC magnetic field of 0.33 T using a resistivity and Hall-effect measurement system (Resitest8300, Toyo Corporation). The microstructure of films was observed by field-emission scanning electron microscopy (FE-SEM; JSM-6500F, JEOL). Chemical states were analyzed by x-ray photoelectron spectroscopy (XPS; ESCA-3400HSE, SHIMADZU) using Mg Kα line with the acceleration voltage of 10 kV and emission current of 20 mA under pressure less than 10^{-6} Pa. The XPS measurements were carried out before and after etching the sample surface by Ar gas with the pressure of 4×10^{-3} Pa, the acceleration voltage of 0.5 kV, and the emission current of 20 mA.

5.2. Results and discussion

5.2.1. Phase identification of thin-films

Figure 5-1 shows XRD profiles of thin films grown by MBE at different temperatures. There is no peak in the profile for 205 ºC, while several peaks are confirmed for above 231 ºC. The intensity and width of the peak at ~27º repectively get higher and smaller with the increase in the growth temperature. This indicates the increase in the crystallinity of films. The Diffraction angles are well matched to those of the reference pattern of chalcopyrite $ZnSnP_2$., although no superlattice reflection could be observed. It seems that the degree of order in the obtained $ZnSnP_2$ is much low. Peaks at other diffraction angles exhibit similar dependence on the growth temperature to the peak at ~27º.

Figure 5-2 shows the EDS compositions of Zn, Sn, and P for the various growth temperatures between 231–317 ºC. P composition is almost constant at 46 mol% in the whole range, while Zn and Sn compositions change between 20–30 mol% depending on the growth temperature. Although these compositions are not totally consistent with that of stoichiometric $ZnSnP_2$, off-stoichiometry of MBE-grown $ZnSnP_2$ was confirmed elsewhere [3,4], maybe due to some kinetic effects. Considering the XRD and EDS results, films above 230 ℃ are likely to be $ZnSnP_2$. Small Zn/Sn ratio at high growth temperature is due to the gap of desorption rates between two cations: the much higher desorption rate and lower nominal deposition rate of Zn than those of Sn. Although the same trend was also expected

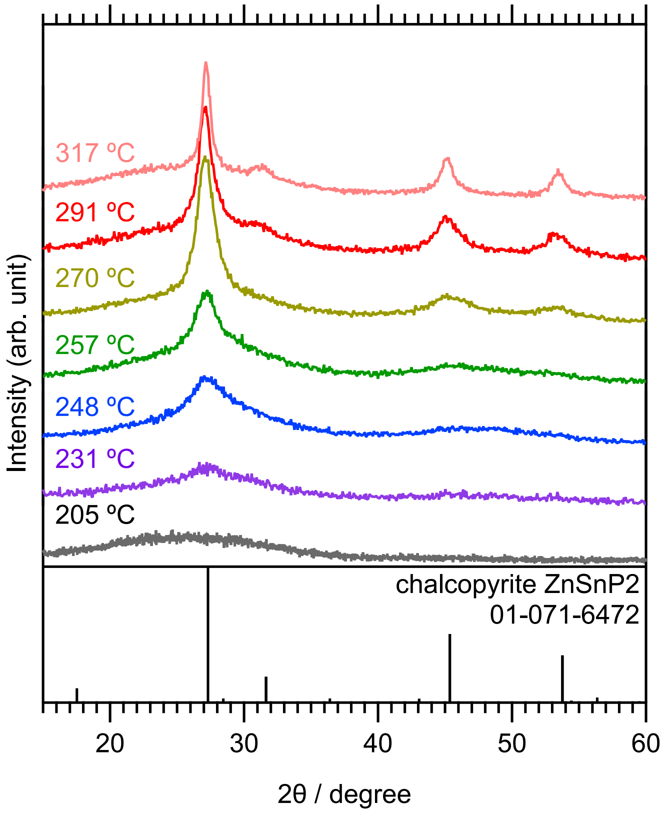

Figure 5-1. XRD profiles of MBE films with different growth temperatures.

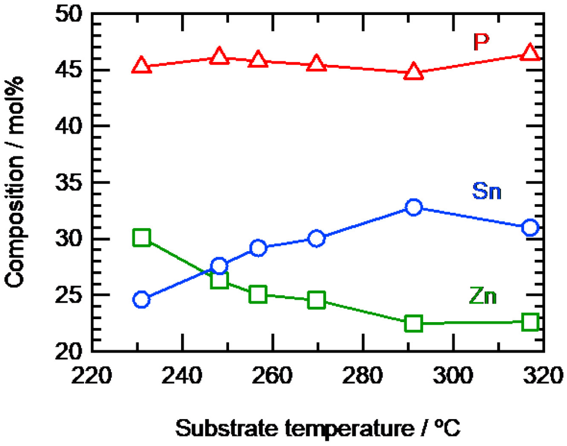

Figure 5-2. EDS compositions of Zn, Sn, and P for thin-films grown by MBE at 231–317 °C.

for P not only for Zn, the large BEP of phosphorus rather dominates the deposition rate than the desorption rate does, resulting in a small dependence of P composition on the growth temperature.

5.2.2. Raman spectra of thin-film $ZnSnP_2$

Figure 5-3 shows Raman spectra of thin-film $ZnSnP_2$. Compared to the spectra of bulk and powder $ZnSnP_2$ discussed in the previous chapter, further broader peaks are observed, of which FWHM is 20–70 cm^{-1}. Similar broad Raman peaks are also reported for nanowire $ZnSnP_2$ [5,6]. As discussed later, FE-SEM observation reveals the grain size of the present films is less than 50 nm. Thus, the broad peaks are the features of small grain size. It was found by fitting analysis that each peak consists of two components over the whole temperature range. Interestingly, peak locations seem changed at a certain growth temperature; two Γ_2 at about 290 and 330 cm^{-1} below 257 ºC while Γ_1 at ~320 cm^{-1} and Γ_{4L} at ~350 cm^{-1} above 270 ºC. Since Γ_2 is a disorder-activated vibration mode as

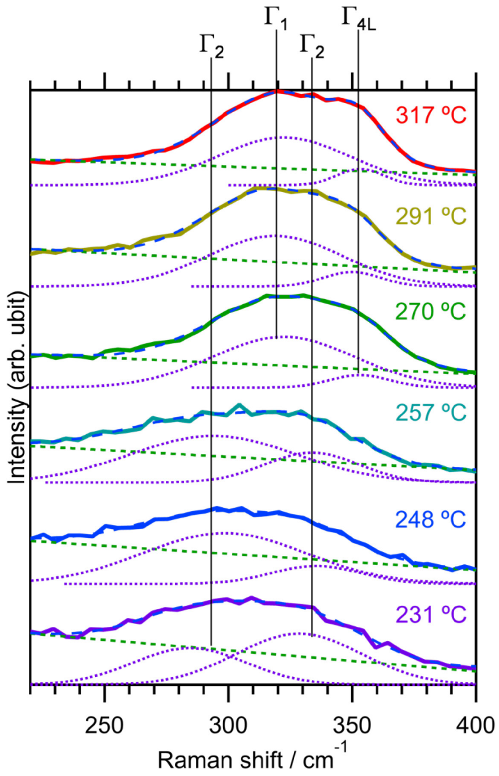

Figure 5-3. Raman spectra of thin-film $ZnSnP_2$ grown by MBE at different temperatures.

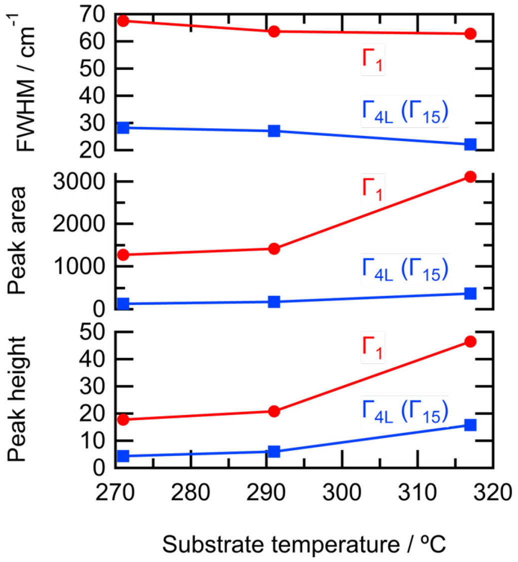

Figure 5-4. Fitting parameters for Raman spectra of thin-film $ZnSnP_2$ grown above 260 ºC.

mentioned above, films grown below 257 ºC are disordered $ZnSnP_2$. Taking account of the much broad peak of GI-XRD, films grown below 257 ºC were rather amorphous. On the other hand, the presence of Γ_1 and Γ_{4L} peaks indicate that films grown above 270 ºC have higher degrees of order. Yet the degree of order is not high enough to evolve superlattice reflection, Raman spectroscopy may detect a slight change even for such a low degree of order. Fig. 5-4 shows the dependence of fitting parameters for thin-film specimens on the growth-temperature above 270 ºC. With the increase in growth temperature, the FWHM decreases while the area and intensities of peaks increases. This may reflect the increase in the crystallinity and, considering the case of the bulk and the powder $ZnSnP_2$ discussed before, partly the increase in the degree of order.

5.2.3. Optical measurements

Figure 5-5 shows transmittance, diffuse reflectance, and absorption coefficients of thin-film grown by MBE. Here, the absorption coefficient α was calculated from the following equation;

$$\alpha = \frac{1}{d}\ln\left[\frac{(1-R)^2}{T}\right], \tag{5-1}$$

where R and T are the measured diffuse reflectance and transmittance divided by 100, respectively. d

is the thickness measured by the stylus, of which the temperature dependence is shown in Figure 5-7. From both transmittance and diffuse reflectance spectra, any obvious absorption edge cannot be confirmed. On the other hand, the absorption coefficients increase abruptly around 0.9–1.2 eV. In addition, the absorption edge seems to shift toward the high-energy side with the increase in the growth temperature. This indicates the increase in the bandgap of the thin-film $ZnSnP_2$ and hence the degree of order. However, it was found that the absorption coefficients take negative values in the low energy region. Because of this, exact absorption edges could not be calculated. Such negative values might be attributed to the inaccuracies in measurement or mismatch of the analysis model. More precise measurements are thus desired for the determination of the absorption edge and hence the bandgap.

Figure 5-6 shows the optical constants evaluated by fitting to the spectra of $\tan\Psi$ and $\cos\Delta$ measured by ellipsometry. Ψ and Δ the azimuth and the phase difference. In the analysis, we assumed that the obtained films consist of stacking of a surface-roughness layer (SRL), $ZnSnP_2$, and soda-lime glass substrate and fitting thicknesses, refractive indices n, and distinction coefficients κ of SRL and

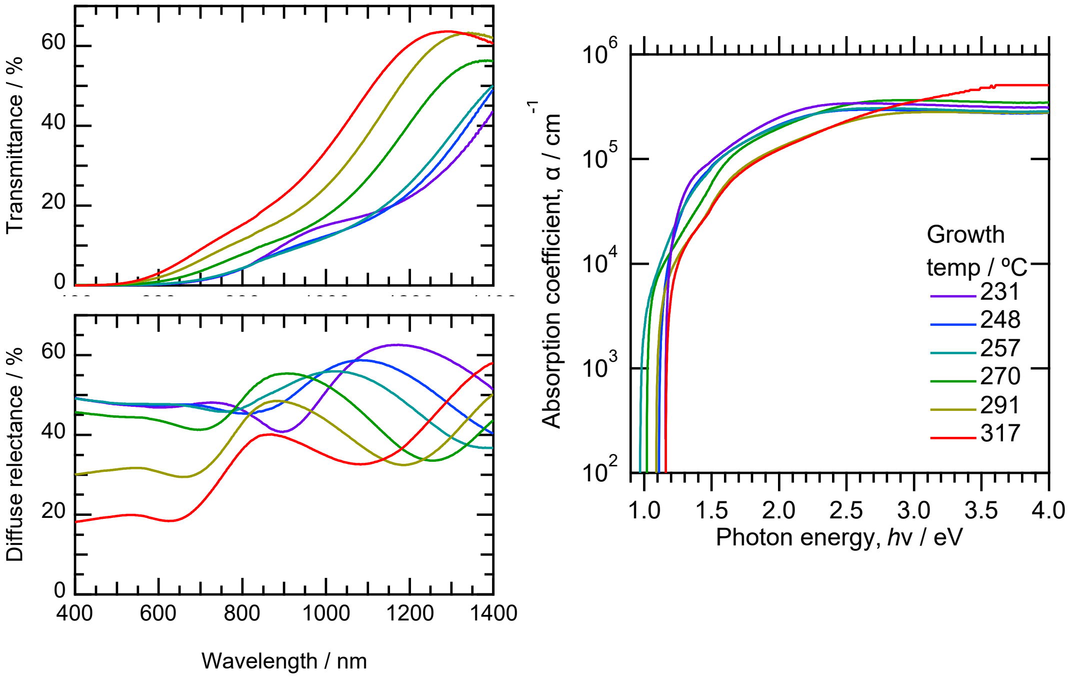

Figure 5-5. (a) Transmittance, (b) diffuse reflectance, and (c) absorption spectra measured on thin-film $ZnSnP_2$ grown by MBE.

$ZnSnP_2$. The thickness of the substrate is fixed at 0.5 mm. As shown in Fig. 5-6(a) and (b), the optical constants n and κ for the growth temperature less than 257 ºC have no distinct peak in the whole energy range, which indicates these films are more amorphous-like. On the other hand, those for above 271 ºC exhibits small peaks in the range of 1–2 eV. These peaks may be associated with absorption, indicating the presence of the band structure in the films. This is consistent with the increase in the crystallinity indicated by both GI-XRD and Raman spectra. In addition, the peak energy slightly increases with the increase in the growth temperature. Similar trend is confirmed in the absorption coefficient as discussed above. The discrepancy between the absorption coefficient evaluated by ellipsometry and that by transmittance and diffuse reflectance may come from the inaccuracies of the measurements or the inherent difficulty in fitting for ellipsometry.

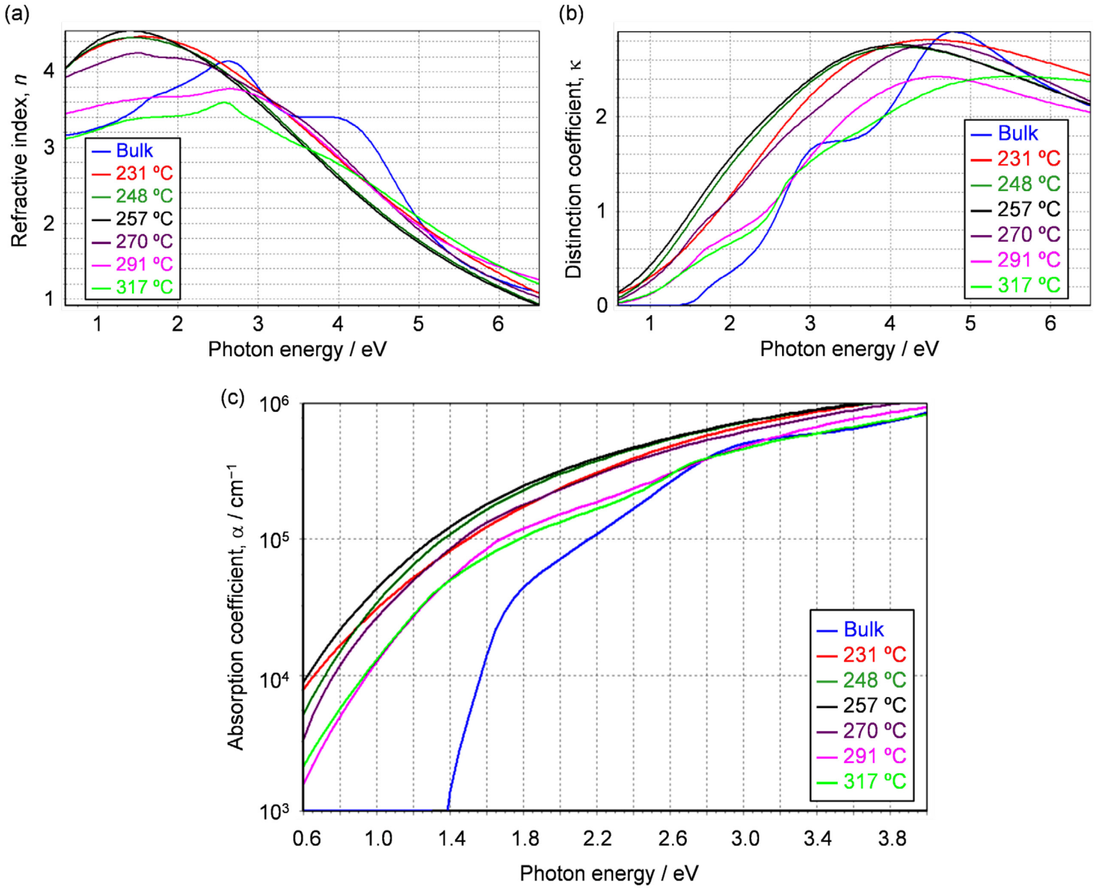

Figure 5-6. (a) Refractive indices, (b) distinction coefficients, and (c) absorption coefficients of thin-film $ZnSnP_2$ with different growth temperatures. Those of bulk $ZnSnP_2$ are also shown for a comparison.

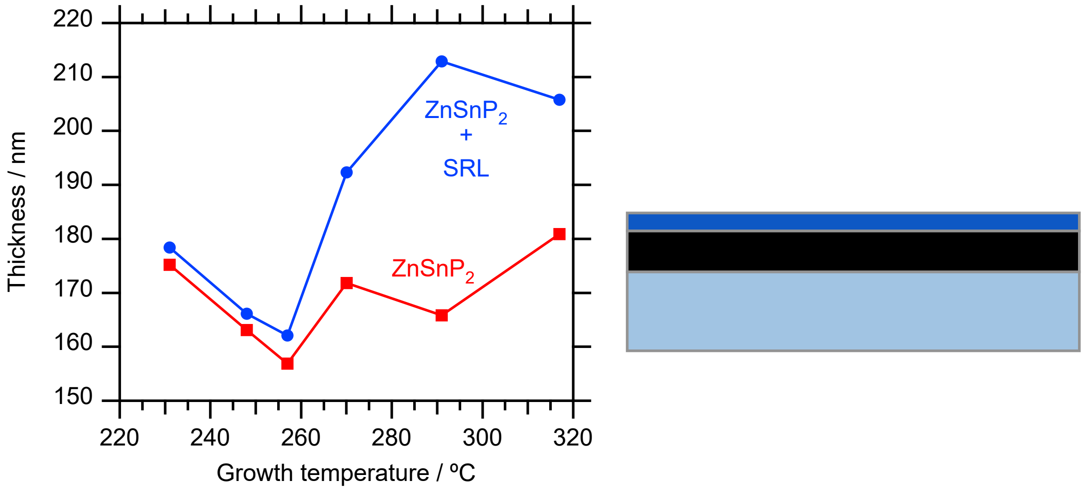

Figure 5-7. (a) The growth temperature dependence of the thickness of surface roughness layer (SRL) and ZnSnP$_2$. (b) The stacking model used in the analysis of ellipsometry.

5.2.4. Ordering in the growth of thin-film ZnSnP$_2$

As pointed out in several studies, the degree of order in ZnSnP$_2$ depends on the growth conditions like cooling rates for bulk crystals [7–9]. The order-disorder transition temperature of ZnSnP$_2$ is assumed to be 993 K or higher [10,11], which is much higher than the growth temperatures for bulk and thin-film ZnSnP$_2$. Thus, nearly perfectly-ordered chalcopyrite ZnSnP$_2$ should be obtained in experiments thermodynamically, and disordered chalcopyrite or sphalerite phases are products of kinetic effects. For bulk crystals grown from the solution of Zn and P in Sn flux, a low degree of order is obtained at a fast cooling-rate, which means an insufficient period for ordering results in an unstable random distribution of Zn and Sn atoms on the cation sub-lattice. For thin-film growth, on the other hand, deposition periods fixed at 120 min and high growth temperature lead to a high degree of order. It is hence considered that sufficient time and temperature are needed for the high degree of order.

In addition to time and temperature, Sn-content may influence cation-ordering in the thin-film growth of ZnSnP$_2$. As discussed in Fig. 5-2, the molar ratio of Sn/Zn varies from 0.82 to 1.46 with the increase in the growth temperature. Seryogin et al. suggested that the increase in BEP ratio of Sn/Zn in MBE leads to the presence of liquid Sn and the change of the growth mode from solid-vapor to solid-liquid-vapor growth [12]. Elyukin and Temkin mentioned, based on a thermodynamical calculation, that the solid-liquid contact reduces the energy barrier to crystallization, resulting in much smaller supercooling, which is a favorable condition for a high degree of order [13]. Liquid Sn can exist in this study, too, since the melting point of Sn (232 ºC) is almost below the subjected growth-temperature range of 231–317 ºC. Therefore, the increase in the degree of order indicated by Raman spectroscopy on thin-film $ZnSnP_2$ may be influenced by the increase of Sn-content and the presence of liquid Sn. Considering the case of the deposition of chalcopyrite $CuInSe_2$ through liquid Cu-Se [14], it may be a common phenomenon that a liquid phase assists cation-ordering during thin-film growth. The influence of Sn-content on the growth mode is indicated by the growth temperature dependence of the thickness of SRL and $ZnSnP_2$ evaluated from ellipsometry. As shown in Figure 5-7, the thickness of the surface roughness layer is much larger for above 260 ºC than that for below 260 ºC, which indicated the surface roughness abruptly changes at that temperature. Such an abrupt change around 260 ºC is also confirmed in Raman spectra in Figure 5-3 and the optical constants in Figure 5-6.

5.2.5. Electrical properties

Figure 5-8 shows resistivity of thin-film $ZnSnP_2$ grown by MBE at different temperatures. The resistivity is higher than 100 Ω cm for all films. Such high resistivity and small thickness (<250 nm) led to high sheet resistance over 10^6 Ω sq., which caused huge noise in Hall effect measurements and hindered the determination of carrier type, concentration, and mobility. As shown in Figure 5-9, it was found by the surface FE-SEM observation that the average grain size of the films is less than 50 nm. Moreover, XPS analysis in the depth direction with Ar etching revealed much content of oxygen in the whole film. Considering both grain boundary and oxygen content can cause carrier-scattering, it is desired to enlarge grain size and remove oxygen in order to reduce the resistivity.

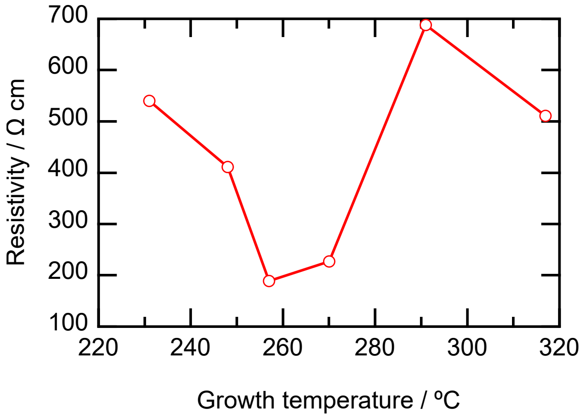

Figure 5-8. Resistivity of thin-film $ZnSnP_2$ grown by MBE at different temperatures.

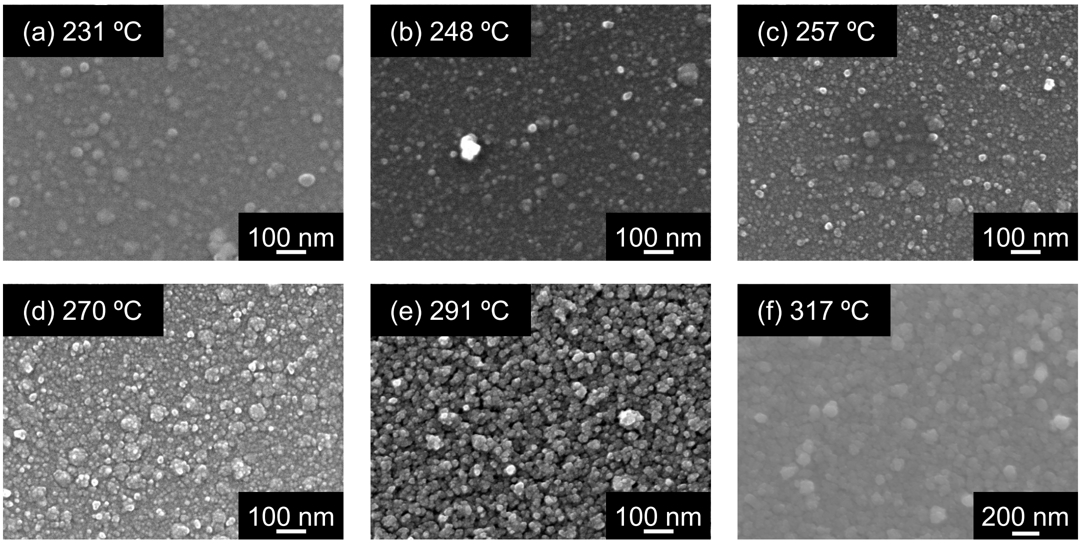

Figure 5-9. Surface FE-SEM images of thin-film $ZnSnP_2$ grown at (a) 231, (b) 248, (c) 257, (d) 270, (e) 291, and (f) 317 °C.

5.3. Summary of this chapter

In the present study, thin-film $ZnSnP_2$ was grown by MBE at different temperatures. GI-XRD indicates crystalline but much disordered $ZnSnP_2$ were obtained above 231 ºC and the crystallinity increases with the increase in the growth temperature. EDS analysis revealed that the composition of the obtained $ZnSnP_2$ is different than the stoichiometry and the cation composition ratio Zn/Sn decreases with the increase in the temperature. Raman spectra of films grown below 257 ºC show two peaks of the Γ_2 mode, a disorder-activated vibration mode, while those for above 270 ºC includes two peaks of Γ_1 and Γ_{4L}. In addition, the peak intensities of both Γ_1 and Γ_{4L} increase with the increase in the growth temperature. These results of Raman spectroscopy indicate the increase in the crystallinity or the degree of order. From optical measurements, the absorption edge seems to shift toward the high-energy side with the increase in the growth temperature. It may reflect the increase in the degree of order. The presence of liquid Sn might be correlated to the ordering in thin-film $ZnSnP_2$. Measurements of carrier type, concentration, and mobility were difficult because of the high resistance probably due to the small grain size and oxygen contents, which must be improved for application.

References to Chapter 5

[1] S. Nakatsuka, Y. Nose, and T. Uda, “Fabrication of $ZnSnP_2$ Thin Films by Phosphidation,” *Thin Solid Films* **589**, 66 (2015).

[2] R. Katsube, K. Terayama, R. Tamura, Y. Nose, “Experimental Establishment of Phase Diagrams Guided by Uncertainty Sampling: An Application to the Deposition of Zn–Sn–P Films by Molecular Beam Epitaxy,” *ACS Mater. Lett.* **2**, 571 (2020).

[3] P.K. Ajmera, H.Y. Shin, and B. Zamanian, “Vacuum Growth of Thin Films of $ZnSnP_2$,” *Solar Cells* **21**, 291 (1987).

[4] H.Y. Shin, P.K. Ajmera, “Characterization of Vacuum Grown Thin Films of $ZnSnP_2$,” *Mater. Lett.* **5**, 211 (1987).

[5] S. Lee, E. Fahrenkrug, S. Maldonado, “Synthesis of Photoactive $ZnSnP_2$ Semiconductor Nanowires,” *J. Mater. Res.* **30**, 2170 (2015).

[6] E.J. Sheets, R.B. Balow, W.C. Yang, E.A. Stach, R. Agrawal, “Solution-Based Synthesis and Purification of Zinc Tin Phosphide Nanowires,” *Nanoscale* **7**, 19317 (2015).

[7] A.A. Vaipolin, N.A. Goryunova, L.I. Kleshchinskii, G.V. Loshakova, E.O. Osmanov, “The Structure and Properties of the Semiconducting Compound $ZnSnP_2$,” *Phys. Status Solidi B* **29**, 435 (1968).

[8] M.A. Ryan, M.W. Peterson, D.L. Williamson, J.S. Frey, G.E. Maciel, B.A. Parkinson, “Metal Site Disorder in Zinc Tin Phosphide,” *J. Mater. Res.* **2**, 528 (1987).

[9] S. Nakatsuka, Y. Nose, “Order–Disorder Phenomena and Their Effects on Bandgap in $ZnSnP_2$,” *J. Phys. Chem. C* **121**, 1040 (2017).

[10] J.L. Shay, J.H. Wernick, “Ternary Chalcopyrite Semiconductors, Growth, Electronic Properties, and Applications” Pergamon Press, Oxford, (1975).

[11] D.O. Scanlon, A. Walsh, “Bandgap Engineering of $ZnSnP_2$ for High-Efficiency Solar Cells,” *Appl.*

Phys. Lett. **100**, 251911 (2012).

[12] G.A. Seryogin, S.A. Nikishin, H. Temkin, A.M. Mintairov, J.L. Merz, M. Holtz, "Order–Disorder Transition in Epitaxial $ZnSnP_2$," *Appl. Phys. Lett.* **74**, 2128 (1999).

[13] V.A. Elyukhin, S.A. Nikishin, H. Temkin, "Energy of Antisite Defects in Chalcopyrites," *Cryst. Growth Des.* **3**, 773 (2003).

[14] T. Wada, "$CuInSe_2$ and Related I–III–VI_2 Chalcopyrite Compounds for Photovoltaic Application," *Jpn. J. Appl. Phys.* **60**, 080101 (2021).

6. General conclusion

Cu_3P back buffer layer for $ZnSnP_2$ solar cells

Re-investigation on the reactive diffusion at the Cu/ZTP interface revealed that the epitaxial formation of Cu_3P beside ZTP through annealing at 400 °C. The electron diffraction analyses revealed the epitaxial relationship of Cu_3P [1100](0001)//ZTP [110](112). In addition, the estimated lattice-mismatch was less than 0.5% on the common triangular arrangements of phosphorus sublattice in both crystal planes. On the other hand, the work function of Cu_3P was close to the ionization potential of ZTP, which indicates the potential barrier against hole transport is small enough at the Cu_3P/ZTP interface. However, the resistance was reduced by the formation of Cu_3P, while longer annealing resulted in an increase in resistance. This might be due to the reduction of electrode area associated with Cu aggregation through interdiffusion. Successfully, by sputtering of Cu_3P on ZTP before the deposition of Cu, we could obtain the lowest resistance by annealing even for 5 min. Interestingly, the thickness of the reacted region was larger than 15 min-annealed specimens without Cu_3P insertion. This indicates that Cu_3P rather worked as a diffusion promoter than a diffusion barrier. Consequently, the *J-V* characteristics of solar cells with intentionally-inserted Cu_3P were close to desirable diode curves; there was no cross-over behavior confirmed in the previous cells. Such improvement of back contact led to good reproducibility and the best efficiency of 3.87 %. This work demonstrated the utility of a "*self-organized back-buffer layer*" like Cu_3P, which is spontaneously formed so as well-matched to absorber in the viewpoints of both atomic configuration and band alignment, for the realization of low resistive ohmic contact.

DLTS and PL analyses on $ZnSnP_2$ bulk crystals

Hole and electron traps in ZTP bulk crystals were investigated by DLTS and PL. DLTS analysis revealed three types of trap in ZTP bulk crystal: two with shallow energy levels and the other with a deep level. Hole and electron traps with shallow levels correspond to so-called donor and acceptor defects, respectively. The previous first-principles study suggested antisite Zn_{Sn} and Sn_{Zn} might be origins of such defects, respectively, in the viewpoint of the formation energy. In the PL spectrum, the sub-gap luminescence in a broad energy range was observed, which could be understood by supposing the spectrum contained four recombinations related to CBM, VBM, and the above acceptor and donor levels. On the other hand, the trap with a deep energy level might come from V_P or Zn_i. The presence of such a deep defect level was implied by the rapid TRPL decay confirmed in our previous work. However, the calculated formation energy of the deep-level defects is not so small, which is slightly inconsistent with the discussion on DLTS. This might be from the discrepancy of the chemical environment, in other words, chemical potentials between the calculation and the actual growth of bulk crystals. It should be investigated in future works.

Raman spectroscopy on $ZnSnP_2$ with various degrees of order

Bulk and powder $ZnSnP_2$ with various degrees of order are characterized by non-polarized Raman spectroscopy. The ordered wafer exhibits a sharp and strong peak of the Γ_1 mode while the disordered flake exhibits a weak and broad one, which is consistent with the report by Mintairov et al. Systematic changes of the peak intensity, area, and FWHM are also confirmed especially for the Γ_1 mode in powder samples with different long-range order parameters. This may suggest that Raman spectroscopy can be used for the evaluation of the degree of order of $ZnSnP_2$, although it is also implied that more quantitative investigation are needed.

MBE growth of thin-film $ZnSnP_2$

Thin-film $ZnSnP_2$ was grown by MBE with different growth temperatures. For the films obtained above 231 ºC, XRD patterns are well assigned to chalcopyrite $ZnSnP_2$, although there is no superlattice reflection. This indicates the obtained thin films are $ZnSnP_2$ with a much low degree of order. The peak width is smaller and the intensity is larger for the higher growth temperature, which indicates the increase in the crystallinity. EDS composition of Zn decreases with the increase in the growth temperature while that of Sn increases probably because of the much higher vapor pressure and desorption rate of Zn than those of Sn. Considering the similar off-stoichiometry repoted in the previous studies of thin-film growth of $ZnSnP_2$, it would be plausible that $ZnSnP_2$ with a off-stoichimetric composition is kinetically obtained. Raman spectra of the films grown below 260 ºC show two peaks of the disorder-activated Γ_2 mode, while those for above 271 ºC show Γ_1 and Γ_{4L}. Such a change of the observed vibration modes may originate from the decrease in defects, i.e., cation-antisites. The increase in the intensity of both modes with the increase in the growth temperature is consistent with the increase in the crystallinity indicated by GI-XRD. The increase in the crystallinity is also indicated by ellipsometry. The absorption edge shifts toward the high-energy side with the increase in the growth temperature, which may be associated with the decrease in the cation antisites. Finally, it is mentioned, as a possible mechanism of thin-fim growth of $ZnSnP_2$, that the presence of liquid Sn indicated by the increase in the Sn/Zn composition ratio also supports the ordering in thin-film $ZnSnP_2$.

Achievements

Journal articles

"Performance enhancement of $ZnSnP_2$ solar cells by a Cu_3P back buffer layer"
Taro Kuwano, Ryoji Katsube, Kenji Kazumi, Yoshitaro Nose
Solar Energy Materials & Solar Cells **221** 110891 (2021).
https://doi.org/10.1016/j.solmat.2020.110891

"Deep level transient spectroscopy and photoluminescence studies of hole and electron traps in $ZnSnP_2$ bulk crystals"
Taro Kuwano, Ryoji Katsube, Steve Johnston, Adele C. Tamboli, Yoshitaro Nose
Japanese Journal of Applied Physics (accepted)
https://doi.org/10.35848/1347-4065/ac468a

Conference proceedings

"Impact of structure on carrier transport behavior at the interface between electrode and $ZnSnP_2$ absorber"
Taro Kuwano, Shigeru Nakatsuka, Yoshitaro Nose
IEEE 7th World Conference on Photovoltaic Conversion, 2998–2999 (2018).
https://doi.org/10.1109/PVSC.2018.8547478

"Improvement of Ohmic Behavior of Back Contact in $ZnSnP_2$ Solar Cells by Inserting Cu_3P"
Taro Kuwano, Ryoji Katsube, Yoshitaro Nose
IEEE 46th Photovoltaic Specialists Conference, 3007–3009 (2019).
https://doi.org/10.1109/PVSC40753.2019.8980788

International conference presentation

"Effect of Interfacial Compounds between Back Electrode and Absorber on Performance of $ZnSnP_2$ Solar Cells"
T. Kuwano, S. Nakatsuka, Y. Nose
27th International Photovoltaic Science and Engineering Conference (PVSEC-27), November 2017

"Impact of structure on carrier transport behavior at the interface between electrode and ZnSnP2 absorber"
T. Kuwano, S. Nakatsuka, Y. Nose
7th World Conference on Photovoltaic Energy Conversion (WCPEC-7), June 2018.

“Interface Structure and Carrier Transport Behavior between Cu Electrode and $ZnSnP_2$ Absorber”
Taro Kuwano, Shigeru Nakatsuka, Yoshitaro Nose
International Symposium on Solar Energy Materials, January 2019.

“Improvement of Ohmic Behavior of Back Contact in $ZnSnP_2$ Solar Cells by Inserting Cu_3P”
T. Kuwano, R. Katsube, Y. Nose
46th IEEE Photovoltaic Specialists Conference (PVSC-46), June 2019.

“Photoluminescence and Deep Transient Spectroscopy for $ZnSnP_2$ Bulk Crystals”
T. Kuwano, R. Katsube, S. Johnston, A. C. Tamboli, Y. Nose
30th International Photovoltaic Science and Engineering Conference (PVSEC-30), November 2020.

“Impact of substrate temperature on bandgap in $ZnSnP_2$ thin films by MBE”
Taro Kuwano, Yoshitaro Nose
31st International Photovoltaic Science and Engineering Conference (PVSEC-31), December 2021.

Domestic conference presentation

“$ZnSnP_2$吸収層とCu裏面電極との接合の界面構造とキャリア輸送”
桑野太郎、勝部涼司、野瀬嘉太郎
第79回応用物理学会秋季学術講演会、2018年9月

“$ZnSnP_2$吸収層/Cu電極界面へのCu_3P層の導入による直列抵抗の低減”
桑野太郎、勝部涼司、野瀬嘉太郎
第66回応用物理学会春季学術講演会、2019年3月

“$ZnSnP_2$太陽電池の裏面電極構造”
桑野太郎、勝部涼司、野瀬嘉太郎
第16回「次世代の太陽光発電システム」シンポジウム、2019年7月

“$ZnSnP_2$吸収層/Cu電極界面へのCu_3Pの挿入による太陽電池の直列抵抗低減と変換効率向上”
桑野太郎、勝部涼司、野瀬嘉太郎
第80回応用物理学会秋季学術講演会、2019年9月

“PLおよびDLTS 測定による$ZnSnP_2$バルク結晶の欠陥評価”
桑野太郎、勝部涼司、Steve Johnston、Adele C. Tamboli、野瀬嘉太郎
第81回応用物理学会秋季学術講演会、2020年9月

“$ZnSnP_2$のＭBE成長における基板温度の影響”
桑野太郎、野瀬嘉太郎
第82回応用物理学会秋季学術講演会、2021年9月

Award and Fellowship

京都大学教育研究振興財団 国際研究集会発表助成 (2019年6月)

京都大学工学研究科馬詰研究奨励賞 (2019年7月)

第46回応用物理学会講演奨励賞 (2019年9月)

日本学術振興会特別研究員 DC2 (2021年4月)

Acknowledgement

First of all, I would like to express my deepest gratitude to my adviser, Associate Prof. Yoshitaro Nose (Kyoto Univ.). Through the six years in Nanostructural Design of Advanced Materials Laboratory, he gave me a principal guide to survive in academic society and taught me what science is and how a scientist should be.

I would also like to thank my thesis committee, Prof. Isao Tanaka (Kyoto Univ.) and Prof. Hiroyuki Sugimura (Kyoto Univ.), for fruitful comments.

I am very thankful to Mr. Kenji Kazumi (Kyoto Univ.), Prof. Takashi Minemoto (Ritsumeikan Univ.), Prof. Shigeru Ikeda (Konan Univ.), Prof. Kenji Yoshino (Miyazaki Univ.), Assistant Prof. Akira Nagaoka (Miyazaki Univ.), Assistant Prof. Hiroyuki Hayashi (Kyoto Univ.), Prof. Fumiyasu Oba (Tokyo Institute of Technology), Associate Prof. Yu Kumagai (Tokyo Institute of Technology), Associate Prof. Hiroki Taniguchi (Nagoya Univ.), Tetsu Ichitsubo (Tohoku Univ.), Assistant Prof. Hongyi Li (Tohoku Univ.), and NREL scientists, Rekha Schnepf, Dr. Andrea Crovetto, Dr. Steve Johnston, Dr. Adele Tamboli, and especially to Dr. Steven Christensen.

I love to give great thanks to all members of this Laboratory, especially to Mayumi Maeda, who always helps me, and Assistant Prof. Ryoji Katsube (Kyoto University) and Dr. Shigeru Nakatsuka (Western Digital), who are the second largest research mentors for me.

Finally, I wish to give my biggest love to my family.

This study was partly supported by Grant-in-Aid for JSPS Research Fellow Number 21J12760.

Taro Kuwano

February 2022